UNIVERSITY OF CALIFORNIA

Santa Barbara

Constraining Hydraulic Properties in Oceanic Crust near the Juan de Fuca Spreading Center

A dissertation submitted in partial satisfaction of the requirements for the degree Doctor of Philosophy in Earth Science

by

Menso Thomas de Jong

Committee in charge:

Professor Jordan Clark, chair

Professor Syee Weldeab

Professor Matt Jackson

Dr. Doug Wilson, Researcher, Earth Science

March 2020

The dissertation of Menso Thomas de Jong is approved.

_____

Doug Wilson

_____

Matthew Jackson

_____

Syee Weldeab

_____

Jordan F Clark, Committee Chair

March 2020

ACKNOWLEDGEMENTS

The work presented in this dissertation would not be possible without the dedicated and capable scientists and crew members of the *R/V Atlantis and R/V Joides Resolution*. Data and guidance from Professor Andrew T. Fisher at the University of California, Santa Cruz and Professor C. Geoffrey Wheat at the Monterey Bay Aquarium Research Institute were also vital to completing this project.

Data presented here builds upon laboratory work completed by Nicole Neira for her 2014 Masters Thesis. Her work and mine were overseen by Professor Jordan F. Clark with patience, understanding, and technical and scientific support.

I would like to dedicate this dissertation to my wife Jaclyn, who has supported me in every life decision throughout my many years of graduate school.

VITA OF MENSO THOMAS DE JONG

March 2020

EDUCATION

Bachelor of Science in Earth Science, California State Polytechnic University, San Luis Obispo, December 2011

Master of Science in Geology, California State University, East Bay, December 2014

Doctor of Philosophy in Earth Science, University of California, Santa Barbara, March 2020

PROFESSIONAL EMPLOYMENT

2010-15: Staff Scientist, Padre Associates, Inc., San Luis Obispo, California

2013-14: Research Intern, Lawrence Livermore National Laboratory, Livermore, California

2015-20: Teaching Assistant/Associate, Department of Earth Science, University of California, Santa Barbara

2018-present: Staff Geologist, Kear Groundwater, Santa Barbara, California

PUBLICATIONS

Analysis of Extrinsic Tracer Data at Seawater Intrusion Barriers in Southern Los Angeles County, Unpublished thesis submitted in partial fulfillment of the requirements for the Master of Science degree in Earth Science, California State University, East Bay 2014. 85 pp.

Identifying paleowater in California drinking water wells, *Quaternary International,* XIV (2018), 56-68.

Tracer Results paper, title TBD, *Journal TBD*, (in prep), 2020.

Evaluating Learning Outcomes in Open-Enrollment STEM General Education University Courses, *Journal TBD*, (in prep), 2020.

FIELDS OF STUDY

Major Field: Hydrogeology

Studies in subseafloor hydrothermal fluid systems with Jordan F. Clark

ABSTRACT

Constraining Hydraulic Properties in Oceanic Crust near the Juan de Fuca Spreading Center

by

Menso Thomas de Jong

Until recently, oceanic crust aquifer properties were estimated from single-borehole experiments and mathematical modeling. This dissertation presents multi-tracer data from a cross-borehole tracer experiment in a hydrothermal system on the eastern flank of the Juan de Fuca Ridge. A rapid tracer breakthrough induced by a ~548 m^3 fluid injection suggests that effective porosity is several orders of magnitude lower than bulk material porosity and ridge-parallel anisotropy may have a large effect on fluid flow in shallow ocean crust. Nine years of data suggest that chaotic local convection does not operate on the 10^2 – 10^3 m scale encompassing this field site. The low effective porosity precludes application of the conventional point-source model for tracer experiments and necessitates the development of a new conceptual model to explain observed tracer breakthroughs and derive aquifer properties. The average linear flow velocity at this site is found to be ~1 m/d. At the 10^2 – 10^3 scale, the representative elemental volume (REV) is constrained for future use in more accurately modeling oceanic crust as a porous medium.

TABLE OF CONTENTS

Chapter 1

Introduction, Setting, Objectives, and Significance

Introduction

On a tectonically active planet, internal heat is redistributed when new crust solidifies from magma and cools near the surface of the planet. On Earth, most of this plate formation occurs beneath the ocean, where new oceanic plates form at spreading centers. Young basalt oceanic basement loses heat conductively, directly to seawater or through overlying sediments, but conductive fluxes do not account for the total heat flux. The remainder is hypothesized to be lost convectively through hydrothermal fluids circulating within fractures and connected pores in the basalt (Lister, 1972). Hydrothermal fluid circulation is driven by convection, where cold dense sea water interacts directly with cooling magma or infiltrates the basalt, is heated, and discharges at a high temperature and lower density. The flux of hydrothermal fluid controls the heat flux, so estimates of fluid fluxes are needed to support the hydrothermal flux hypothesis.

Given known spreading rates and the thermal properties of the basalt, sediments, and ocean water, studies have compared the measured global oceanic lithosphere heat flux with the theoretical conductive solution and concluded that the theoretical total conductive

flux exceeds observed fluxes by 30% (Figure 1.1). It is hypothesized that hydrothermal circulation accounts for the “missing” thirty percent (Pelayo et al., 1994).

Some of the heat flux occurs via “active” hydrothermal circulation, where water that infiltrates young basalt near a ridge interacts directly with magma erupting in sheeted dike complexed (Lister, 1972). Active hydrothermal systems discharge at or near the ridge axis and produce the dramatic “black smokers” with discharge temperatures measured upwards of 400° C (Macdonald et al., 1980). Hydrothermal discharge is also observed on ridge flanks, tens to hundreds of kilometers from ridge axes, but these systems discharge at much lower temperatures, considerably below 100° C (Mottl and Wheat, 1994). In these “passive” hydrothermal systems, water is heated by residual heat instead of direct contact with cooling magma (Lister, 1982). Only approximately 30% of the global hydrothermal heat flux is thought to occur in active hydrothermal systems (Stein, 1994), so the remaining 70% must be accounted for in passive systems.

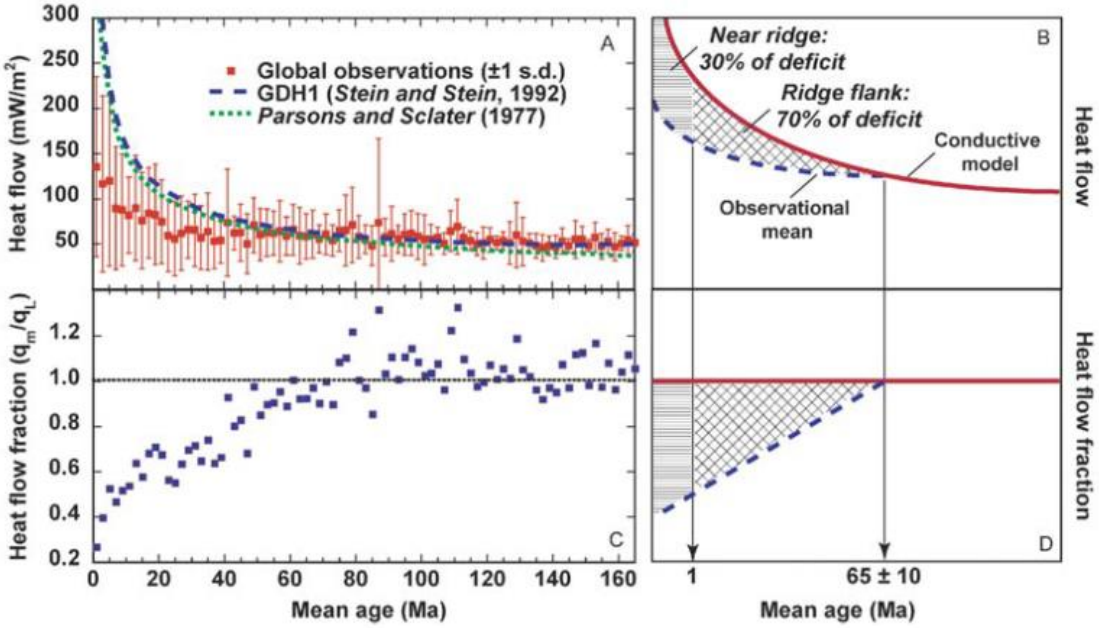

Figure 1.1 – Global conductive heat deficit, depicted as measured heat flux q_m compared to modeled conductive heat flux q_L. 1.1A depicts global heat flux measurements and conductive models. 1.1B presents a simplified graphical presentation of the same data. Figure from Fisher (2005), modified from Stein et al. (1995).

In situ and laboratory petrographic studies of boreholes from globally distributed ridge flank sites suggest that hydrothermal systems operate in the upper several hundred meters of ridge flank lithosphere, with a decrease in activity with depth and age due to overburden compaction and hydrothermal mineral deposition (Bartetzko and Fisher, 2008; Fisher, 2005). These trends are clear but the specific properties are not well defined, so investigating passive ridge flank hydrothermal heat flux is an important area of study with considerable improvements still to be made. In order to do so, we must refine our estimates of ridge flank aquifer properties.

Definitions of Aquifer Properties

In a terrestrial setting, fluid flow through porous media is controlled by Darcy's equation (see equations 1.1a, 1.1b, and 1.1c below), which relates discharge (Q) to several parameters. Head gradient (dh/dl), i.e. elevation difference per length, is the driving force, hydraulic conductivity (K) is a single parameter that controls the ease of water flow through a specific medium, and the cross-sectional area (A) converts flow velocity to volume. Discharge is often reported as flow per unit cross sectional area, known as Darcy Velocity or specific discharge (q). As long as units remain consistent, any units of time and distance are valid. Hydraulic conductivity is difficult to measure, and is dependent on fluid properties and the both the porosity and interconnectivity of the porosity in a medium, permeability, such that it is possible for a highly porous medium (i.e. clay) to have very low hydraulic conductivity if pores are isolated from each other.

$$Q = dh/dl * K * A \quad (1.1a)$$

$$q = Q/A \quad (1.1b)$$

$$q = dh/dl * K \quad (1.1c)$$

In hydrothermal systems, the underlying Darcy equation remains the same, but related terms must be substituted for the conventional terms. Density differences instead of head gradients drive flow, so pressure differences are substituted for differences in head. Hydraulic conductivity (K) is a single term integrating both medium and fluid properties, which are temperature dependent. It is a term only valid for a single fluid at a specified

temperature, since the ease of fluid flow through a porous medium is altered by changes in fluid density (ρ) and dynamic viscosity (μ). These properties differ with fluid composition and temperature, as do hydrothermal fluids in varying systems. Permeability (k) is the component of hydraulic conductivity (K) that is solely reliant on the porous medium properties. For purposes of comparison with other hydrothermal systems, permeability is derived from hydraulic conductivity (Equation 1.2) and reported in place of hydraulic conductivity. Permeability is reported in SI units as square meters (m^2), which is commonly converted Darcys (D) in the petroleum industry.

$$k = K * \mu / (\rho * g) \quad (1.2)$$

When permeability and thus conductivity are defined, the volume of fluid that may be moved through a unit width of an aquifer is known as the transmissivity (T), obtained from the product of conductivity and aquifer thickness (b) (Equation 1.3). The effective aquifer thickness is limited by the extent to which hydraulic conductivity decreases with depth. Therefore, this study seeks to refine estimates of conductivity and the basement aquifer depth profile in order to more accurately define global passive hydrothermal fluxes.

$$T = K * b \quad (1.3)$$

Some physical properties integral to understanding mass and energy flux are not immediately apparent in the Darcy equations. Porosity (n), the unitless percentage of void space in a material, describes the volume of water that can be contained within an aquifer material. But all porosity is not equally impactful on fluid fluxes in an aquifer. Dead end pores, vesicles, and poorly interconnected fractures do not function to transmit water

effectively over significant distances (Figure 1.2). Effective porosity (n_e) describes the percentage of interconnected void space in a material and is more difficult to measure than the bulk material porosity. Furthermore, n_e may be inversely related the distance scale in question, that is to say that much of the porosity in a hypothetical medium might be capable of transmitting fluid on a sub-meter scale but only a small fraction of that porosity might be sufficiently interconnected to transmit fluid for hundreds to thousands of meters.

Darcy flow also only describes aquifer properties in one direction. An aquifer response to head differences results in a fluid flux at a velocity controlled by n_e, but the outcome is not necessarily identical in all directions. In terrestrial alluvial aquifers, vertical (K_z) hydraulic conductivity is commonly assumed to be an order of magnitude less than lateral (K_x and K_y) conductivity, due to horizontally deposited strata and fine-grained laminations. Lateral conductivity is not impacted by such formations, so K_x is assumed to equal K_y and the aquifer is said to be laterally isotropic. As a result, radial coordinates are commonly used in terrestrial settings ($K_x = K_y = K_r$). In fractured volcanic rock aquifers, sedimentary depositional dynamics do not control directionality of properties, complicating assumptions. Fluid may flow in primary porosity between mineral grains, and over larger distances secondary porosity controlled by faulting and fracturing may dominate. The forces causing secondary porosity, namely tectonic stresses, are directional in nature, so lateral conductivity may be highly anisotropic. Fault-guided secondary porosity might channel fluid strongly in the longitudinal direction, while transverse conductivity could be severely limited by lacking connectivity. Lateral anisotropy (A_L) is defined as the ratio of these directional properties (Equation 1.3).

$$A_L = K_x/K_y \quad (1.3)$$

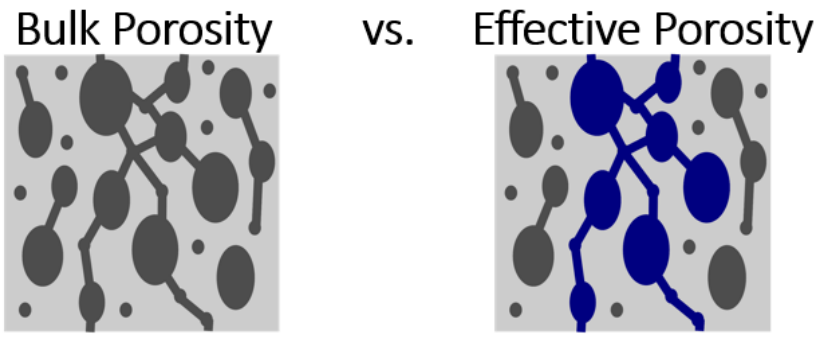

Figure 1.2 – Cartoon comparison of n and n_e.

Motivation – The Representative Elemental Volume

Modeling fractured rock as a porous medium is a question of scale. Fracture systems are inherently heterogeneous, but at progressively larger scales, the distribution of heterogeneity in properties such as porosity, anisotropy, and permeability are sufficiently captured such that the properties of the volume in question represent the homogeneous bulk properties of the material as a whole. This Representative Elemental Volume (REV), as described by Bear (1974), is the fundamental minimum unit volume used to construct three-dimensional finite element and finite difference models of fractured flow systems. Prior crustal-scale computer modeling efforts (e.g. Rosenberg and Spera, 1990; Rosenberg et al., 1993; Winslow et al., 2013; 2016) rely on the REV concept to utilize porous media models for hydrothermal fracture flow systems. A primary goal of this study is to use tracer

results to refine the representative elemental volume scale and properties for modeling ocean crust aquifer systems.

Setting

The setting of this study is on the eastern flank of the Endeavor segment of the Juan de Fuca spreading center, 150 kilometers west of northern Washington State. At this rift zone ridge, new basaltic oceanic crust is continually created, with the eastern half being conveyed eastward to eventually be subducted under the North American plate at the Cascade Subduction Zone, giving rise to the Coast Ranges and volcanic Cascade Mountains in the Pacific Northwest (MacDonald, 2001). The Endeavor rift zone has hosted a series of studies over the past five decades aimed at expanding our knowledge of four primary questions about hydrothermal circulation at seafloor spreading centers: hydrogeological properties, driving forces, fluxes, and sources and sinks of fluids and materials. From 1968 to 1983, the Deep Sea Drilling Program (DSDP) funded ocean drilling expeditions that map the sea floor, collected core samples, and logged wells, leading to the development of the current conceptual model describing crust production rates, sedimentation from continental sources, and regional geochemistry (Fisher 2005). The DSDP has been superseded by several similarly named organizations, and is now known as the International Ocean Discovery Program (IODP).

Drilling expeditions starting in 1997 defined continental sediment accumulation thicknesses and examined heat fluxes on the seafloor east of the Endeavor segment of the

Juan de Fuca rift zone via IODP borehole measurements (Davis et al., 1999) and sediment core observations (Fisher et al., 2003). Unconsolidated continental sediments are exceptionally thick for the age of crust east of this segment due to topographic relief both on and off shore, in addition to the close proximity of the spreading center to the continental margin.

The close proximity to land makes the Juan de Fuca an anomalous ridge flank to study. The North American plate provides a source for neritic sediments, and seafloor bathymetry at the ridge produces a buttress that trapped Miocene to Pleistocene turbidity flows that conveyed sediment from the continental margin (Anderson et al., 1970; Silver, 1972). This thick and impermeable sediment cap over the young basalt crust insulates the basalt from conductive heat loss and produces the strong heat gradients that drive the ridge flank geothermal systems (Fisher et al., 2003). The thick impermeable layer functions as an effective confining layer, simplifying the ridge flank hydrothermal system concept.

This study utilizes four IODP boreholes, 1301A, 1362B, 1301A, and 1026B (Figure 1.3), located between two basalt outcrops, Baby Bare and Mama Bare, which are hypothesized to function as discharge points, facilitating a flow system conducting hydrothermal water in a northeasterly direction away from Grizzly Bare, a hypothesized primary recharge outcrop 52km to the southwest (Hutnak et al., 2006). The tracer study commenced in August 2010 and concluded with the removal of all sampling equipment in June 2019. A known mass of sulfur hexafluoride (SF_6), cesium (Cs), and plastic microbeads were injected into borehole 1362B during IODP Expedition 327 in 2010. Continuous

OsmoSamplers™ (OS) were installed at various locations in the injection borehole (1362B), two downgradient boreholes (1362A and 1026B), and one upgradient borehole (1301A). The distances between these boreholes varied from approximately 221 m to approximately 550 m, with the most extant boreholes separated by approximately 1076 m (Figure 1.3). The fine-grained sediment above the basalt basement is approximately 200 m thick in the study area, and the boreholes extended 50 m to 250 m into the basement aquifer (Figure 1.4).

Large scale regional flow on the Juan de Fuca flank is thought to originate at the spreading center, where cold seawater quenches the lava, forming the fractured basalt basement. As the basalt is translated east towards the subduction zone, the fluid within is confined by the fine-grained sediments originating from the continental margin. Complicating this anomalous situation, north-south trending faults may create anisotropy in the fracture structure, preferentially routing flow parallel to the ridge. Seamounts with topography adequate to avoid burial under sediments appear to act as regional discharge or recharge areas, hypothesized to create density-driven hydrothermal convection cell aquifers (Hutnak et al., 2006). Seafloor heat flux measurements and ROV observations support this hypothesis (Wheat and Mottl, 2000).

In these systems, fluxes are driven by density differences between cold bottom seawater and hydrothermal basement fluid. In outcrops, where effective porosity is adequate to permit connection to the underlying aquifer, cold seawater descends, is heated by residual lithospheric heat, and discharges through other outcrops due to the subsequent

decrease in density and increase in pressure (Winslow et al., 2016). Estimates have been made on the fluxes of fluids through these seamounts (Wheat and Mottl, 2000), but it is yet to be determined if these fluxes are significant in the broader regional flow.

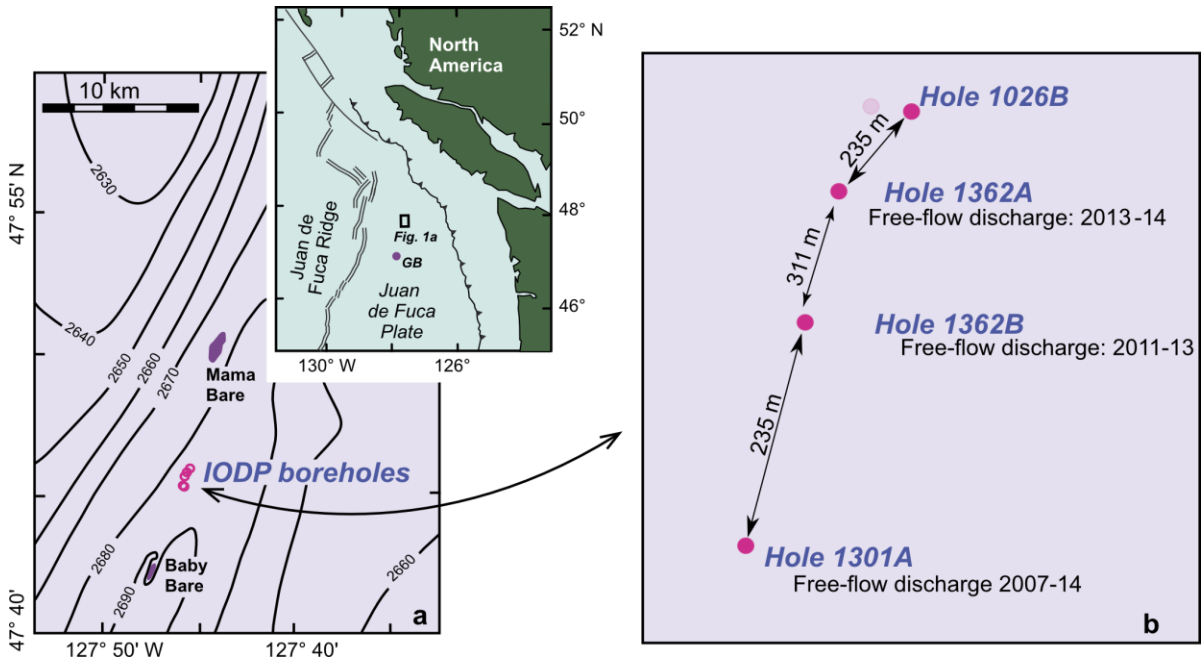

Figure 1.3 – Site maps at various scales. Baby Bare and Mama Bare are known fluid discharge seamounts. GB indicates Grizzly Bare outcrop, the hypothesized recharge location for this system. Hole 1026B location replotted to accurately reflect location. Modified from Neira et al. (2016)**.**

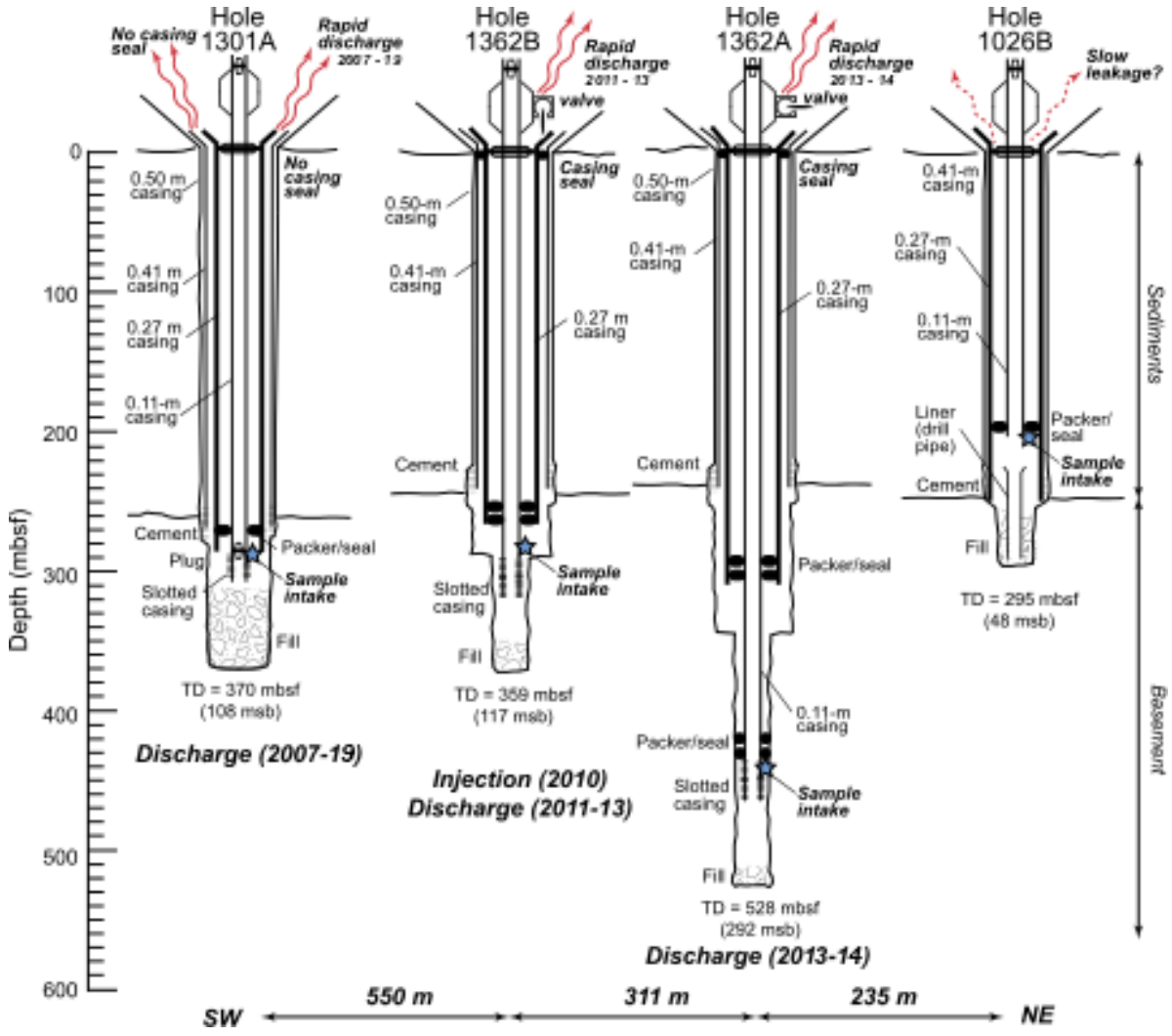

Figure 1.4 – Schematic diagram of CORKS and boreholes, vertically to scale (modified from Neira et al. 2016)**.**

Sediment Accumulation in the Cascadia Basin

The sediment accumulation zone bounded by the North American continental slope to the east and the Juan de Fuca rift zone to the west is known as the Cascadia Basin. Continental sediments are supplied to this Basin via hemipelagic settling and turbidity flows which terminate off the continental slope near the subduction zone. Seven major

submarine canyons have eroded the continental slope, the two largest associated with the two major rivers draining the Pacific Northwest (Silver, 1972). Beyond the continental slope, sediments are deposited in submarine fans in the Cascadia Basin. These undisturbed sediments in the Basin are restricted to Late Miocene age or younger; any sediments older than Late Miocene have either been subducted along with the Juan de Fuca plate or folded and accreted onto the continental slope (Silver, 1972).

In the south, the Astoria Canyon is an extension of the Columbia River, the sediments from which create the Astoria seafloor fan. To the north, the Frazer River empties through the Straits of Juan de Fuca, supplying sediments to cause turbidites which have carved the Juan de Fuca Canyon. The Juan de Fuca Canyon and associated continental slope canyons to the north supply sediment to the Nitinat Fan. The site of this study is in ~3.5 million year old crust in the northern area of the Basin at the toe of the Nitinat Fan, midway between the rift zone and continental slope, approximately 240 km offshore.

Holocene sedimentation rates in the Cascadia Basin are much lower than during the Pleistocene. Modern sedimentations rates of 1-10 mm per 1000 years are observed, compared to rates as high as 170 mm/yr in Pleistocene sediments (Griggs et al., 1969). Sedimentation in the Basin is largely dominated by turbidity flows, though in modern times sedimentation rates are not high enough to sustain frequent turbidites (Anderson et al., 1970; Carson et al., 1986; Knudson and Hendy, 2009). These submarine flows of mass-sorted suspended sediments carve submarine canyon and eventually deposit onto the fans and plains below. Without outside disturbance, turbidity flow frequency is controlled by the

sediment delivery rate. When sediments exceed the maximum angle of repose and become unstable, potentially triggered by earthquakes, large storms, or tsunami, a flow occurs, so high sediment delivery rates decrease the time interval between flows. During glacial maximums, increased erosion due to glacial scouring delivered large volumes of sediments to the Pacific margin. Compounding this increased sediment load, lower sea levels at glacial maximums resulted in river mouths extending onto or near the continental slope, more or less directly depositing sediment into the submarine canyons that feed the basin fans (Knudson and Hendy, 2009). At present, the coast is over 100 km east of the continental slope, so sediments have a considerable distance to settle out before reaching the major canyons. Earthquakes also trigger turbidities flows, the evidence of which can be seen in the tectonically active Cascadia Basin (Gutiérrez-Pastor et al., 2013). The frequency of such events has not changed significantly since the Miocene.

When initially formed at the spreading center, the basalt oceanic crust is free of continental sediment cover. Suspended sediment fallout constitutes the deepest sediments, but as the crust is transported towards the subduction zone, hemipelagic sediments fill in local depressions and overcome ridges, allowing sandy and silty turbidite sequences to dominate crust over approximately 1.5 Ma old (Underwood and Hoke, 2000). Coring in the Cascadia Basin began in the late 1970's and has continued with the various incarnations of the Ocean Drilling Program. Together with seismic surveys, early studies affirmed the then newly-discovered concept of plate tectonics by characterizing basin sediments and examining their deformation in the landward accretionary wedge anticipated to exist in the subduction zone. (Carson et al., 1974). The thickest sediments, at approximately 2.5 km

thick, were found at the base of the continental slope (Carson et al., 1974), as predicted by the tectonic model.

In addition to turbidites of glacial origin, there is strong evidence for rapid sediment accumulation due to glacial lake outburst floods of Glacial Lake Missoula. These floods followed the Columbia River channel and deposited sediments on the Astoria Fan. Extremely thick turbidite beds have been identified, and accumulation rate are calculated to three to five times greater those on the Nitinat Fan during the applicable timeframe. As this project site is on the Nitinat Fan to the north, fed by the Frazer River watershed, impacts from Glacial Lake Missoula floods are limited to fine grained sands and suspended sediments carried by ocean currents in a plume away from the extent of turbidite activity (Knudson and Hendy, 2009).

In the Nitinat Fan, core sediment characterization reveals primarily silty clays with small fractions of sand. Some rafted dropstones have been identified as well. Similar compositions were seen in IODP drill logs for the boreholes utilized by this study (Fisher et al., 2005). These fine-grained sediments form a relatively impermeable layer which insulates the basaltic crust below and confines hydrothermal fluids contained within.

Geochemical Data Revealing Hydrothermal Fluid Fluxes

Submarine hydrothermal systems were hypothesized during the oceanographic advances made following the Second World War. As the body of evidence for seafloor spreading grew, heat flow measurements taken at intervals from ridge axes confirmed what was expected from the theory: maximum heat flux is found near ridges and decreases

symmetrically on flanks (Lister, 1972). Elder (1965) was the first to point out that the same necessary components for terrestrial hydrothermal systems were present in submarine settings and propose that oceanic hydrothermal systems were a possibility. Heat was certainly present, he observed, and a virtually unlimited supply of water available. Rather presciently, Elder also noted that "the major problem is the question of permeability" (Elder, 1965).

Hydrothermal black smokers were discovered by Ballard et. al in 1977, and the Ocean Drilling Program and its descendent programs have investigated hydrothermal systems around the globe since the late seventies. Many studies have since reduced the magnitude of Elder's permeability problem, but fundamental constraints on crustal permeability and hydrothermal fluid residence time remain elusive. Geochemical methods have been the primary tool for determining hydrothermal fluid residence time. Correlating hydrothermal fluid age indicators with other proxies for age, such as distance from the axial ridge, has established that recharge occurs at axes and discharge occurs along the flanks, but linear velocity estimates span three to four orders of magnitude (Elderfield, Wheat, Mottl, Monnin, & Spiro, 1999). Complicating matters, isolated data points contradict trends in porewater geochemistry along rift flank transects, indicating that local recharge zones exist on ridge flanks and conduct hydrothermal flow along ridge-parallel faults (A. Fisher et al., 2003).

This study examines ridge-parallel hydrothermal flow on the eastern flank of the Juan de Fuca ridge, utilizing sulfur hexafluoride (SF_6) as a deliberate (added) tracer in a cross

hole experiment to determine local fluid linear velocity and constrain aquifer properties. The planning, execution, and analyses of results are built upon the prior geochemical studies detailed in this paper.

Composition Chemistry

Bottom water is the essentially limitless source of homogenous recharge water for oceanic hydrothermal systems. Upon recharge into the basalt aquifer, the water is heated by residual geothermal heat to temperatures as high as 400° C, circulated in convection cells of unconstrained size, volume, and flux. Heated water is discharged, either rapidly through black smokers near ridge axes and basalt outcrops on ridge flanks, or slowly by diffusing through the relatively impermeable sediments covering the basalt to depths of up to several hundred meters (Neira et al., 2016). During the process, the geochemical makeup of the hydrothermal fluid evolves. Compounds are exchanged with the basalt, any radioisotopes continue to decay, and the water progresses with age from having an oceanic bottom-water geochemical composition to a unique composition controlled by the media it travels through. The degree of evolution towards this mature hydrothermal composition is a proxy for hydrothermal fluid age.

Dissolve Salts Composition and Exchange

When oceanic bottom water recharges into oceanic sediments and basalt aquifers, it is heated and exchanges salts with the aquifer matrix. Among other salts, magnesium and sulfate are removed over time, and calcium and chloride are leached from the matrix and

dissolved in the fluid (Mottl & Wheat, 1994). Observing these trends in vertical and transect profiles reveals the evolution of porewater after recharge.

Oxygen Isotope Evolution

The chemical exchange of oxygen-containing compounds between the basalt and hydrothermal fluid fractionates oxygen and over time a unique isotopic signature evolves in porewater (Elderfield et al., 1999). At the relatively low temperatures present in ridge flank hydrothermal systems, alteration of basalt leads to $\delta^{18}O$ enrichment in more altered basalt. Since the exchanges occurs between the basalt and porewater, a depleted $\delta^{18}O$ is indicative of longer residence time in the basalt. During higher temperature alteration, the fractionation is opposite, with $\delta^{18}O$ depleting in the basalt and enriching in the porewater.

Radiocarbon Dating

Porewater inherits the ^{14}C of bottom water upon recharge and the atomic clock continues. Bottom water is mixed well enough to maintain a stable radiocarbon composition, but recharge into basalt aquifers isolates the porewater. Since ^{14}C dating is useful to tens of thousands of years, well in excess of the residence time of bottom water even in deep ocean basins of several thousand-meter depth, radiocarbon dating can be used to approximate the age since recharge. Geochemical exchanges and the complex hydrologic properties in fracture flow systems complicate this method, skewing the results towards

older apparent ages (A. T. Fisher, 2004), but it provides a good starting point for investigating porewater age.

Age Proxies for Correlating Geochemical Tracers

In order to evaluate geochemical tracers as indicators of porewater residence time, they must be correlated with established proxies for age. The most obvious of these is simply the distance from the assumed recharge location. In bottom sediments, recharge is extremely slow and vertically oriented, making vertical profiles appropriate. On a larger scale, recharge occurs at the ridge axis and hydrothermal fluid convection occurs perpendicular to the axis. On the ridge flank, where heat flux studies and geochemical analyses (Hutnak et al., 2006) support the hypothesis that local recharge and discharge occurs at basalt outcrops, flow may be more likely to be parallel to the ridge axis approximately aligned with faults that occur at the same orientation relative to the ridge. While this explanation is clear with the current understanding of plate tectonics and ocean spreading, developing that model required a combination of geophysical and geochemical data.

Spreading Rates and Potassium-Argon Dating

Seafloor spreading and, ultimately, plate tectonics gained widespread acceptance after the discovery of symmetrical patterns in seafloor magnetic anomalies about ridge axes worldwide. The symmetry and apparent correlation between reversal observed at multiple spreading centers provided the geophysical basis, and radiometric dating supported the

hypothesis (Pitman, Herron, & Heirtzler, 1968). Potassium-Argon and Argon-Argon dating (Duncan & Hogan, 1994) of young oceanic crust correlates magnetic anomalies with ages worldwide, and allow for precise reconstructions of spreading rates. The K-Ar age of crust at the study site is approximately 3.5 Ma. Obtaining the age of crust is important for hydrogeologic studies, because crust becomes less permeable over time due to compaction and mineral alteration restricting pore size and connectivity (Elder, 1965). Additionally, when modeling geochemical tracer transport through aquifer, one must take into account the alteration timing scheme, since changes in permeability and geochemistry affect correction factors that must be applied to tracer results (Fisher, 2004).

Intrinsic Tracers as Age Indicators

Elderfield et al. (1999) conducted an extensive geochemical transect of the eastern flank of the Juan de Fuca ridge. They produced vertical and longitudinal profiles which revealed expected trends and, just as importantly, identified points in disagreement with understood trends. Those outliers were assumed to be the result of localized convection cells between basalt outcrops, a hypothesis that is tested by this study. These results and discussion are summarized below, along with the implications of this study. Results plotted in Elderfield et al (1999) are shown in Appendix 1.1.

Salts and Oxygen Isotope Depth Profiles

In depth profiles in sediment overlying basalt, the sites assumed to be part of the larger ridge axis convection show expected trends in geochemical evolution. Shallow

porewater in the confining sediment exhibit bottom water composition for dissolved sulfate, chloride, and magnesium and trended toward the evolved composition with depth, indicating a long residence time in the sediment. Within approximately 100m of the interface with the basalt, the geochemical trends in porewater composition reverse, reverting to values nearer the bottom water signature. This indicates that younger, unevolved water is circulating in the relatively more permeable basalt, beneath the stagnant and evolved water confined within the low permeability sediment.

Isotopic date mirrors this finding. Bottom water and evolved hydrothermal fluid have different δ^{18}O signatures, and the same trend as above is observed. Sediment porewater initially exhibits bottom-water qualities, with an alteration at depth to the evolved value, returning to bottom water conditions near the basalt. This is due to fractionating O-isotopes between the fluid and matrix, and results in more positive δ^{18}O with time and depth in sediment. The ratio difference is only approximately 1‰ at its peak, but this peak is well resolved within the profiles.

Salts in Longitudinal Profiles

Eight samples taken at intervals from zero to approximately 100 km east of the ridge axis also indicate the expected evolution over distance and time of large-scale hydrothermal circulation from bottom water composition at the ridge axis to evolved porewater. Coupled with models of aquifer properties and geochemical interactions, these salt data could be used as a proxy for porewater age and linear flow velocity.

Isotopic Data in Longitudinal Profiles

Elderfield et al. (1999) analyzed samples for $\delta^{18}O$, $^{87}Sr/^{86}Sr$, and ^{14}C, and plotted against distance from the ridge axis. The results are summarized below. Figures from Elderfield et al. (1999) are reproduced in Appendix 1.1.

Oxygen Isotope Longitudinal Profile

As expected, porewater near the axis matches the $\delta^{18}O$ of bottom water, and evolves to more depleted values with distance (time). This is due to low temperature exchanges between the fluid and matrix fractionating oxygen, enriching $\delta^{18}O$ in the matrix, resulting in depletion of porewater with time. The observed $\delta^{18}O$ isotopic profile thus supports the large-scale flow direction hypothesis

$^{87}Sr/^{86}Sr$ Longitudinal Profile

During mantle and lithosphere differentiation, rubidium partitions between the mantle and continental crust with the crust having a greater concentration. The ocean, which derives its constituents from continental erosion, thus has higher Rb and its radiogenic daughters than fluids in the mantle. ^{87}Rb decays to ^{87}Sr with $\tau_{½}$ of 4.8 x ^{10} years, and the ocean is relatively well mixed, so ocean water exhibits a stable equilibrium $^{87}Sr/^{86}Sr$ value higher than mantle fluids, which are isolated from the continental radiogenic ^{87}Sr reservoir. Oceanic crust is derived from mantle material depleted in ^{87}Sr, so fluids entrained in basalt are no longer in communication with the continental reservoir, so their $^{87}Sr/^{86}Sr$ ratio is anticipated to decrease with residence time. Longitudinal profiles follow this trend,

with axial porewater $^{87}Sr/^{86}Sr$ reflecting the ocean water standard. Samples obtained farther from the axial recharge zone exhibit decreasing $^{87}Sr/^{86}Sr$, indicating that porewater is no longer receiving radiogenic ^{87}Sr from the equilibrated oceanic reservoir and is evolving with time toward the more depleted basalt value.

Radiocarbon Longitudinal Profile

Of all the tracers mentioned, only ^{14}C has the direct ability to be used as a clock for calculating flow velocities (Elderfield et al., 1999). The expected trend emerged, with young axial porewater and older ^{14}C ages farther from the ridge crest. Ages range from 1000yr to 10,000yr, and produce estimated velocities of 1-3 m/yr. This range is in agreement with estimates obtained from salt, strontium, and oxygen isotopic evolution.

Complications with Radiocarbon Dating of Porewater

Radiocarbon ages must be reported as apparent ages, because inputs of dead carbon (given its $\tau_{1/2}$ of ~ 5700 years; ^{14}C should have decayed away after ~40,000 yr) can have a significant effect on the calculated age. Elderfield et al. (1999) accounted for carbon addition due to organic diagenesis, but did not attempt to quantity other inputs of carbon, such as volcanic inputs. Any dead carbon input will increase the apparent age of porefluid, decreasing the estimated flow velocity calculation made using that value. This added tracer study results imply that such an overestimation of age is occurring, producing inferred velocity results 2-3 orders of magnitude greater, on the scale of meters per day rather than

meters per year. Any additional radiocarbon dating of oceanic porewater should take care to account for all sources of additional carbon.

Study Objectives

This study seeks to determine hydraulic properties of sediment-confined and -insulated fractured basalt hydrothermal systems, and test the underlying hypotheses governing the specific conceptual hydrothermal system on the flank of the Juan de Fuca Ridge. Interpretation of the tracer results in the context of the engineered borehole sampling systems provide a means to determine how deep the fluids are circulating in the basalt, which is currently estimated to be between 100 to 600 meters below the top of the basement based on lithologic log interpretations. Separate from these modeling efforts, documentation of the field and laboratory methods provide insights for future aquifer studies, in both terrestrial and subsea settings.

On the eastern flank of the Juan de Fuca Ridge, geochemical transect studies on the evolution of porewater support a ridge-parallel (north-south) flow hypothesis (Elderfield et al., 1999), as do tracer data from the first two years (Neira et al., 2016) of this nine-year experiment. The dataset is now complete, analyzed in context of the conceptualized hydrothermal system, conceptually modeled in order to test whether the north-south flow hypothesis is supported and if the estimated fluxes from the seamounts account for a significant portion of the aquifer flux. More broadly, the tracer results provide constraints on the porosity, anisotropy, specific discharge, and depth profile of such properties in young

oceanic crustal aquifer systems worldwide, which serve to account for the observed thirty percent excess heat flux hypothesized to be transmitted via hydrothermal conduction and convection.

In summary, interpreting and modeling the tracer results test the following hypotheses:

1. Prior indirect estimations of effective porosity in young oceanic basalt are reasonable and representative of the large-scale hydraulic properties of oceanic crust worldwide.
2. There is a vertical permeability structure in young oceanic basement aquifers confining flow to an upper portion of the basement with a minimum depth of hundreds of meters.
3. Transmissivity in young oceanic basement hydrothermal aquifer systems explains the observed excess heat flux.

On the eastern flank of the Juan de Fuca Ridge, a ridge flank hydrothermal system conducts fluid north-south, parallel to the ridge. This system may be controlled by recharge and discharge via seamounts which account for a significant portion of the system mass balance.

Significance

The empirical data on SF_6 and Cs tracer movement, governed by the flow (i.e., advection, dispersion) and aquifer properties (i.e., depth dependent permeability, transmissivity, etc.), aid in understanding those properties in the seafloor system. In

addition to investigating the properties of seafloor hydrothermal systems, contrasting the values obtained from the tracer data with estimates from other groundwater age methods could further the science of hydrology in general.

In addition to illuminating poorly constrained subseafloor hydrothermal system properties, practical knowledge from this study may have applications in terrestrial fracture flow systems. Fractured rock aquifers are increasingly exploited for potable and irrigation water resources, so understanding aquifer dynamics and contaminant transport in such systems is an emerging area of study. Geothermal power plants also rely on REV modeling of fractured rock hydrothermal systems (e.g., Müller et al., 2010), and some knowledge from this study may be transferrable to that field.

Recent climate engineering studies concerning carbon sequestration have evaluated subseafloor crustal aquifers as a receptor for carbon dioxide (Brewer et al., 2000; Paukert et al., 2012; Slagle and Goldberg, 2011). For the same reasons that made it appealing for this study, namely the impermeable sediment capping young and thus less-altered crust in close proximity to continental anthropogenic carbon sources, the Juan de Fuca plate in particular has been studied (Goldberg et al., 2008). Findings from this study constraining aquifer properties in this region are directly transferrable to such studies. The effective porosity of the aquifer system is directly related to the substrate surface area available to bind injected carbon dioxide, and the estimates found in this study have potentially enormous consequences for the feasibility of such operations.

Central to these applications is the REV concept. The data presented here can be used to define REV scales and parameters for numerical solutions. This study along with Neira et al. (2016) are the first subseafloor cross-borehole tracer experiment, and extends the direct observation of hydrothermal fluid flow from 10^1 meter-scale single borehole packer experiments to over 10^2 meters. Paired with a cross-borehole pressure-response study by a co-chief scientist on this project (Fisher, 2008), permeability, effective porosity, and longitudinal anisotropy can be reasonably constrained at a scale useful for crustal-scale modeling.

Chapter 2

Expedition History

Introduction

A tremendous amount of planning, engineering, and funding made this study possible. IODP, ODP, and DSDP cruises to the Juan de Fuca and other ridge flank environments laid the groundwork upon which this studied was founded. The body of scientific, operational, and engineering knowledge made this cross-hole crustal tracer experiment possible under 2500 meters of ocean water, drilled and sealed through several hundred meters of sediment. Knowledge gained from the drilling of these and other boreholes has enabled both the field experiments and my interpretations of the results.

Except for one sample-retrieval cruise in July 2019, all field activities were completed prior to the laboratory analyses described in this study. This chapter summarizes the various field activities undertaken and described by the scientists and crew of the research vessels *RV Joides Resolution* and *RV Atlantis* in their respective cruise reports. Their work made this study possible.

Foundational Expeditions to the Juan de Fuca and Other Ridge Flanks

Early expeditions to the Juan de Fuca region focused on ridge-normal hydrothermal systems. The foundational expeditions of discovery to mid-ocean ridges in the 1970's and 1980's revealed dramatic high-temperature hydrothermal features producing superheated water, distinct depositional morphology, and supporting unique ecosystems (e.g., Macdonald et al., 1980; Haymond, 1983). Later ODP and IODP expeditions shifted focus from axial hydrothermal systems to sedimentary and geochemical transects from the ridge axis to subduction zones and accretionary prisms. On the Juan de Fuca, the short distance between the oceanic crust production at the ridge and subduction under the North American continental crust produce a unique geomorphic environment ideal for the study of ridge flank processes. Continental sediments rapidly accumulate on young basalt, providing thermal insulation and an effective hydrogeologic confining layer. These phenomena catalyzed a series of expeditions starting in the early 1990's, leading up to the 2010 tracer injection described in this dissertation.

1990 ODP Leg 139

IODP Leg 139 visited the Middle Valley in 1990, and studied the sedimented rift. Hydrothermal features in the rift zone were catalogued and studied, boreholes penetrated up to 175 m into the basalt. The primary motivation for this cruise was the recognition that rapid

confining and insulating sedimentation burying newly formed oceanic crust creates a unique environment for studying subseafloor hydrothermal systems.

2002 IODP 204 Gas Hydrates

In 2002, IODP Leg 204 visited the subduction zone, and conducted sedimentological studies on the thick accumulations of Pleistocene turbidites derived from glacial outwash and Missoula Floods. The study area spanned across the subduction zone and obtained seismic and coring data from accretionary wedge sediments emplaced on the continental rise.

2006 IODP 311

Accretionary wedge transects were completed by the 2006 IODP Leg 311 cruise to study gas hydrates. This cruise did not include ridge flank investigations.

Project Conception and Organization

In the late 1990's, scientists began discussing the possibility of conducting hydrothermal studies on the Juan de Fuca ridge flank (Fisher, A. T., personal communications). The thick sediment cover confining layer was hypothesized to amplify flow in the underlying fractured basalt, convecting remnant heat in a lower temperature hydrothermal system.

Flow in this system was poorly constrained. Subsequent studies revealed the sediment thickness, basement topography, and bulk aquifer properties. Dominant flow direction, linear velocity, and volumetric flux were estimated via coring, sampling, modeling, and seafloor

observations, but a field-scale cross hole experiment would provide direct observations to better study these features.

Basalt Porosity Studies

Aquifer matrix porosity was estimated from cored drilling through continental sediments into the basement. In terrestrial settings, lab table experiments can provide reasonable estimates from hand samples produced from drilling and trenching, but subseafloor investigations are complicated by numerous factors. Core recovery is often pore, leading to biased sampling towards more cohesive formations. Highly fractured zones that may channel the bulk of hydrothermal flow are likely underrepresented in cores. Coring locations themselves are highly heterogeneous, as rift volcanism and tectonics are spatially and temporally variable.

Based on observations of twenty cores, Bartetzko and Fisher (2008) determined that Juan de Fuca basalt core bulk porosity varied from 0.02 to 0.30, and averaged 0.06 ± 0.03. Oceanic crustal heat flux modeling studies have assumed n=0.10 for simplicity (e.g. Winslow et al. 2013, 2016), so core observations appeared to validate the assumed value.

In unconsolidated aquifer matrices, hand sample bulk porosity can reasonably approximate field scale properties, but in fractured rock aquifers, spatial heterogeneity and fracture connectivity greatly affect properties over distance. As such, hand sample-scale properties might be considered a maximum bound on *effective* properties, since permeable fractures may only be connected over a scale of meters or less. Effective porosity at field scales of 10^2 m or greater therefore may be orders of magnitude less than observed bulk porosity.

Borehole Logging and Seismic Velocity Surveys

Within basement basalt, permeability is controlled by fracture density and fracture connectivity. These properties are determined by depositional and post-depositional processes. At the ridge, the uppermost basalt solidified from extrusive volcanism in contact with seawater, forming pillow basalt morphology. Pillow basalts are fractured during quenching and heterogenous in size and shape, resulting in high bulk porosity.

Beneath pillow basalts, shallow intrusive sheeted dikes also contain considerable and varied fracturing. At depths of several hundred meters, massive intrusive gabbros provide few fractures to allow permeability.

Post-deposition, basement basalt experiences seismic events as it translates from the ridge to the subduction zone. Faulting can produce both conduits and barriers to groundwater flow, and may preferentially connect preexisting fractures in a common vector, introducing anisotropy to the system. Over millions of years, seawater and hydrothermal fluid weathers fresh basalt, altering volcanic glass through ion exchange and filling fractures with vein deposits.

All the above processes alter the bulk density and mineral composition, which can be proxies for permeability. *In situ* aquifer properties are difficult to measure (and the goal of this study), but density and mineral composition are more easily assessed.

Electronic resistivity and gamma ray logging after drilling reveals zone of alteration and increased aquifer flux by relying on differing properties of drilling and formation fluid and increased radioactivity in clay minerals relative to unalterd formation. Seismic velocity surveys

measure porosity through the inverse relationship between fracture desnity and seismic velocity. These methods reveal a stratified and heterogeneous system, with permeability limited to approximately 600 m subbasement.

Project Site Expeditions Timeline

Specific to this study, multiple IODP and Atlantis expeditions visited the project site. Two of the four boreholes utilized in this study predated the tracer experiment ideation, though they needed to be adequately sealed to control hydrologic conditions prior to tracer injections. Boreholes 1362A and 1362B were specifically drilled and CORK'd immediately prior to tracer activities in 2010, and a series of expeditions between 2011 and 2019 retrieved and replaced samplers.

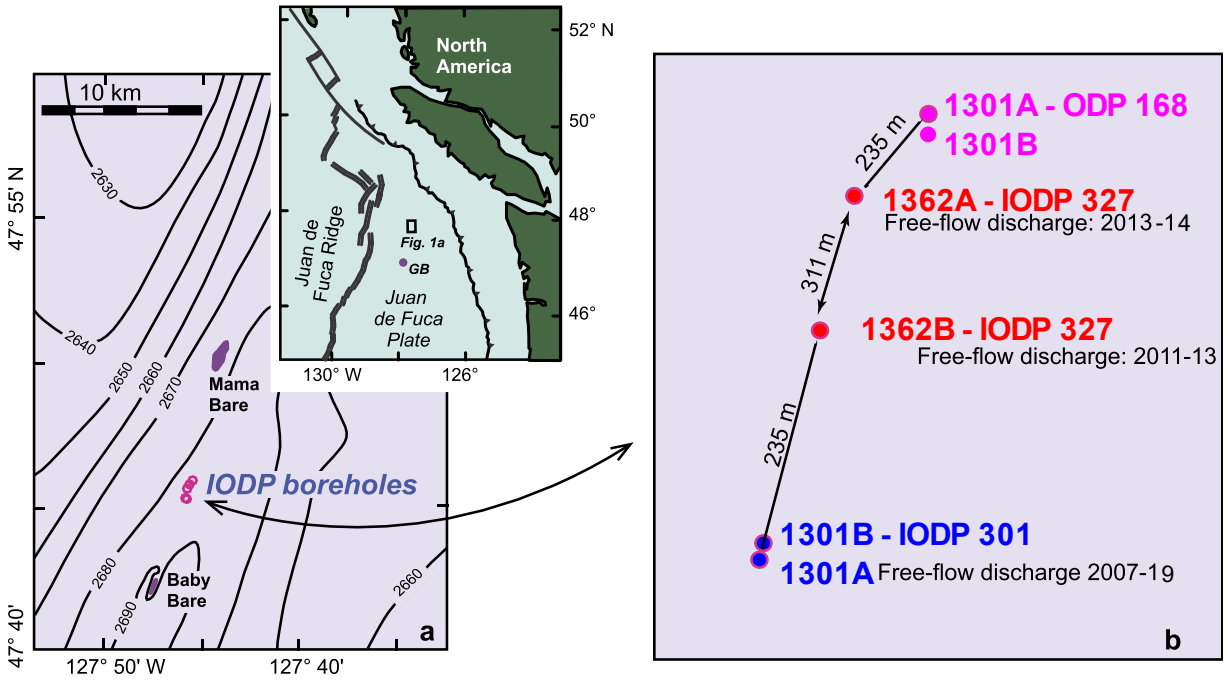

Figure 2.1 – Site maps at various scales showing boreholes relevant to this study indicating the expedition each was first drilled. Modified from Neira et al. (2016)**.**

1996 - ODP Leg 168

In 1996, the project site was undisturbed. Expedition 168 was the first expedition geared towards investigating ridge-flank hydrothermal hydrogeology on the “rough basement” portion of the Juan de Fuca Plate. The expedition consisted of a northwest to southeast transect beginning at the western-most extent of ocean bottom sedimentation.

Drilling and sampling from multiple boreholes provided evidence of homogenized hydrothermal fluid properties. These observations are important in that they provide evidence for circulation vigorous enough to homogenize basement fluid temperatures regardless of sediment cover thickness variations. Combined with pore fluid geochemistry transects, seafloor heat flux measurements, and visual observations of hot spring discharge, these findings supported the seamount hydrothermal syphon theory.

Expedition 196 advanced the first borehole at the “Second Ridge” site that became the location for this tracer study. On July X, 1996, the drillship *RV Joides Resolution* advanced borehole 1026A and 1026B. After the borehole CORK installation, fluid samples were collected from the sediment pore water and basement intervals. Those samples revealed that the basement fluid was more geochemically evolved than the sediment fluid, indicating that the sediment pore fluid is largely derived from bottom water percolating millimeters per year, whereas the basement fluid composition was similar to that of samples obtained from hot springs emanating from nearby basement outcrops.

2005 IODP 301

During the summer 2005 Expedition 301, the JR crew removed the defective CORK from borehole 1026B and replaced it. The new CORK was pressure tested to ensure the seal, which provided an opportunity to observe cross-hole effects. Fisher (2008) analyzed these data to crucially provide aquifer property estimates on a much larger scale than previously available. For the first time, OsmoSamplers were installed to collect representative time-series formation water samples.

Additionally, boreholes 1301A and 1301B were drilled, though full seals were not achieved. Both boreholes leaked extensively from partially-cemented reentry cones.

2009 IODP 321T

IODP Expedition 321T was not a dedicated drilling expedition, but two weeks of the planned transit from Astoria to the Atlantic were dedicated to work on the Juan de Fuca. An attempt was made to cement 1301A and 1301B to prevent further disturbance to the natural formation gradient. Cementing operations at 1301B resulted in a full seal, but 1301A continued to leak, though at a reduced rate.

2010 IODP 327

In September 2010, IODP Expedition 327 sailed. This expedition was dedicated to work at the Second Ridge project site to initiate this tracer study. Boreholes 1301A and 1026B predated this expedition, and were outfitted with wellhead and downhole OsmoSamplers, and new pressure and temperature sensor strings.

Two new borehole observatories were installed for use in this study: 1362A and 1362B. Located between the preexisting borehole, these holes were outfitted with the most up to date CORKs, casings, and sampling systems. 1362B was selected as the tracer injection site, and 1362A was to be the most proximal observation point at 211 meters in the projected downgradient direction. Achieving effective seals was of the utmost importance for multiple reasons. Primarily, the tracer injection experiment was intended to assess hydrologic properties by observing advection and dispersion induced by natural flow conditions. Drilling disturbances (mud injection) and the pressure difference between the warm over-pressured formation water and the cool, dense bottom water cause random spontaneous flow in unsealed boreholes, so sealing was essentially a requirement for the assumptions to be valid. During tracer injection, immense pressure was required to deliver hundreds of cubic meters of injectate into the formation, which the seal needed to withstand. Lastly, ball valves were installed at the new boreholes. These were intended to facilitate induced push pull experiments through controlled overpressure discharge when a valve remained open.

Tracer injection spanned 24 hours, and constituted approximate 548 m^3 fluid injection. SF_6, Cs, plastic microspheres, and other tracers were mixed onboard the ship for injection via the drillship's mud pump. Injectate consisted primarily of surface seawater, with two one-hour periods of freshwater injection from tanks in the ship commencing at hour one and hour twenty. SF_6 injection commence after 20 minutes, and concludes when the two small SF_6 tanks were emptied after approximately 20 hours. Cs salts were mixed and injected in two brief pulses, at approximately 3 and 19 hours into the 24-hour injection.

Sample Retrieval Expedition Summaries

Following the 2010 tracer injection, four annual cruises were planned for sample retrieval and wellhead valve operations (Figure 2.1). The 2011, 2012, and 2014 cruises sailed as planned, but delays lead to the eventual cancelation of the 2013 site visit, resulting in some complications. In June 2019, an additional expedition visited the site and the team was able to secure ship time to retrieve two samplers containing approximately five years of additional data.

2011 - R/V Atlantis Expedition AT18-07

Wellhead samplers were retrieved and replaced with new well head samplers. Furthermore, a ball valve on borehole 1362B was opened to induce pumping conditions.

2012 - RV Thomas G. Thompson (delayed)

Ship delays due to mechanical issues resulted in this planned expedition not reaching the project site. Some wellhead samplers overpumped, resulting in early-time sample loss.

2013 - R/V Atlantis Expedition AT25-04

Wellhead samplers were retrieved and replaced with new well head samplers. The 1362B ball valve was closed and the ball valve on borehole 1362A was opened.

2014 - R/V Atlantis Expedition AT26-18

The 2014 cruise retrieved wellhead samplers from all locations, and withdrew drillstring-mounted downhole samplers from 1362A, 1362B, and 1026B. No new downhole samplers were

installed. Wellhead samplers calibrated for long term operation were left in place at 1362A and 1362B, with all valves closed.

2019 - R/V Atlantis Expedition AT42-11

The last remaining wellhead OsmoSamplers were retrieved from 1362A and 1362B. All valves remained closed, and no samplers were reinstalled. At this time, there are no planned cruises to the project site for the purpose of continuing to monitor the tracer movement.

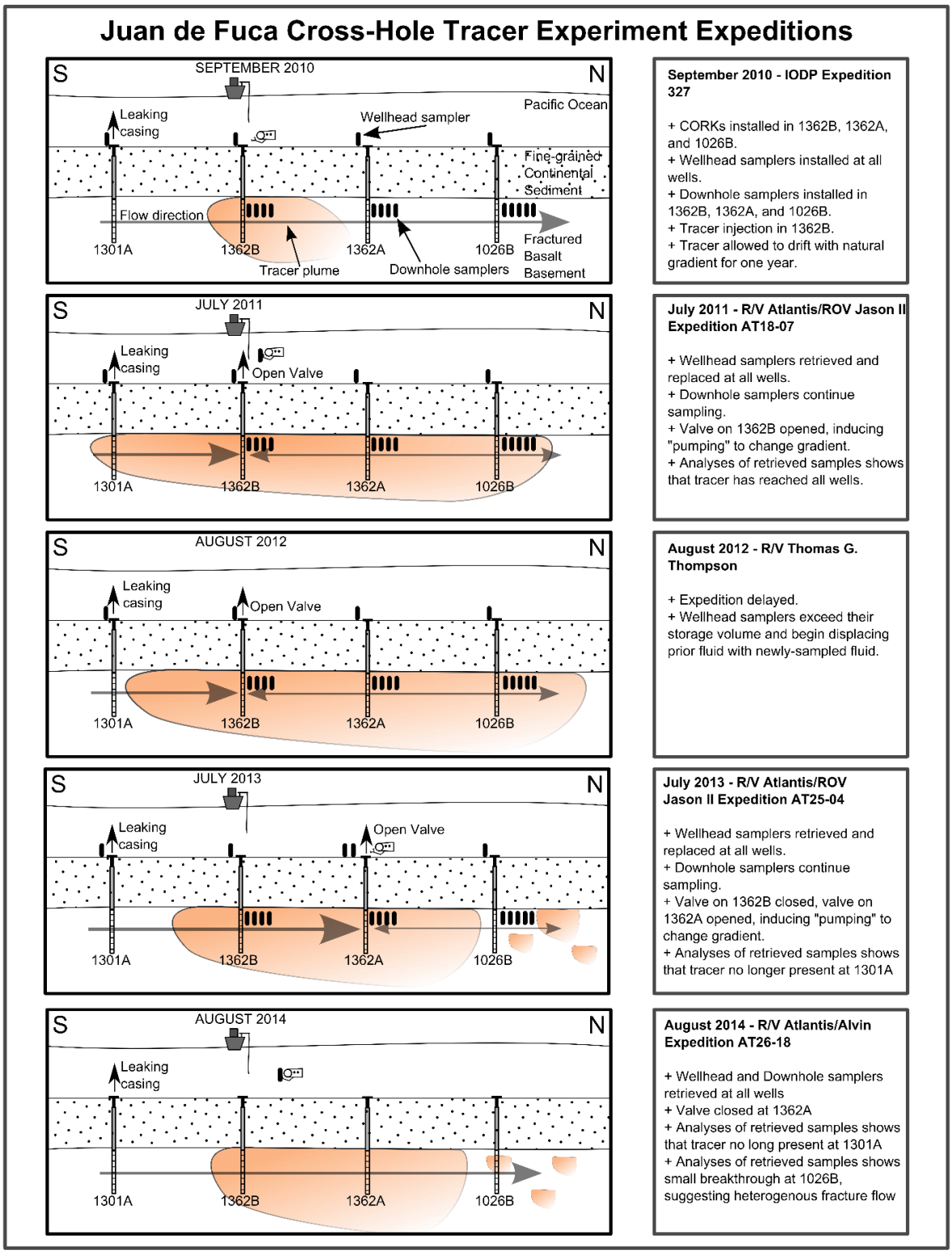

Figure 2.1 – Conceptual timeline of experiment, omitting June 2019 unplanned sample retrieval.

Push Pull Experiment Design

During the four-year duration of the tracer experiment, ball valves on two of the wellhead CORKs (1362A and 1362B) were opened or closed during recovery expeditions to the project site (Figure 2.3). The desired outcome was that the changes in pressure gradient induced by these operations would produce SF_6 breakthrough curves corresponding to each change in conditions. It was hoped that the operations at CORK 1362B, the injection borehole, mimic the classic push-pull methodology used to evaluate contaminant field locations in terrestrial setting (e.g., Leap and Kaplan 1988). This experiment design was a three-phase process of injecting a tracer, allowing it to drift, and then "pumping" the injection location at a known rate, sampling at the injection location during all three phases. The resultant responses in tracer concentration at the injection location were to be used to complete a tracer mass-balance and estimate hydraulic properties at the site (Figure 2.3

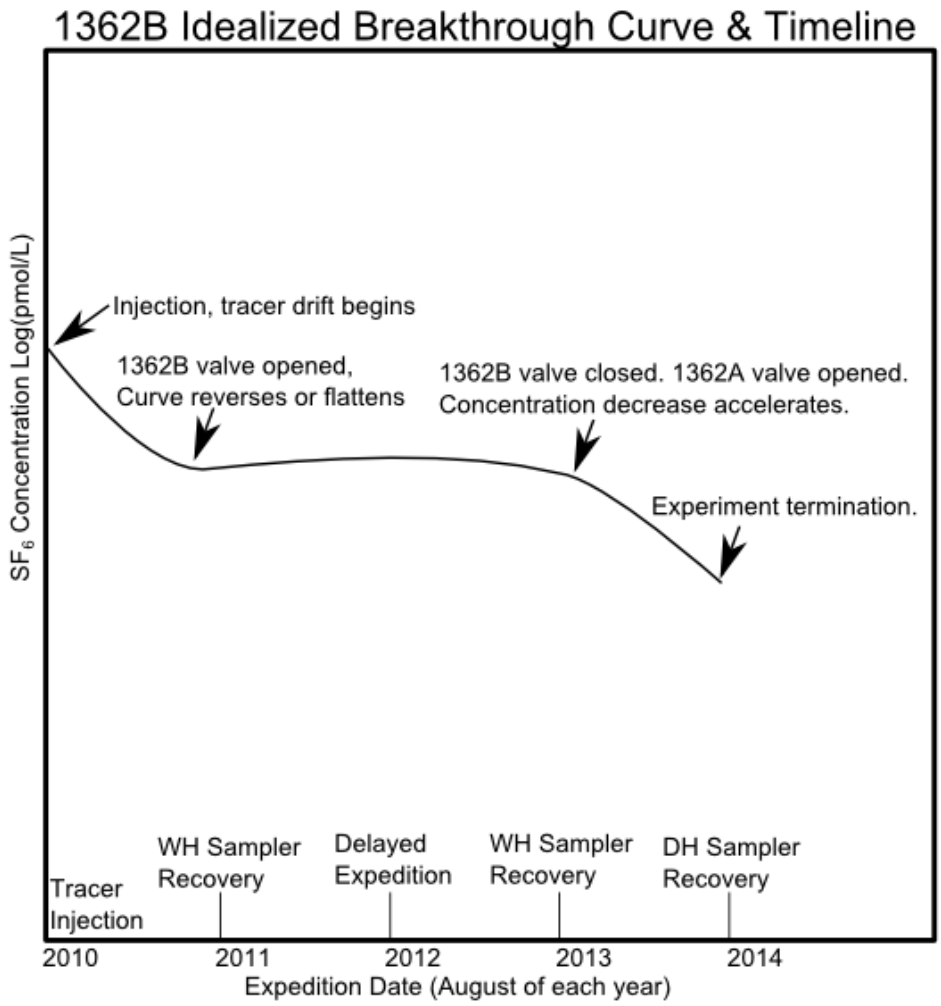

Figure 2.3 – Timeline and idealized expected breakthrough curve for injection hole 1362B.

Summary

Foundational expeditions and cruises prior to work completed in this dissertation enabled the work presented herein. Field work spanning the Juan de Fuca, from the buried ridge to transects across the accretionary prism built the scientific knowledge and engineering abilities that precipitated the genesis and execution of this multi-borehole tracer experiment.

Chapter 3

Continuous Sampling for an Added Sulfur Hexaflouride Gas Tracer Using Osmotically Pumped OsmoSampler Water Sampler

Laboratory Methods and Lessons Learned

Abstract

High temporal resolution sampling is crucial for groundwater tracer and contaminant transport studies. Osmotically-driven Osmosamplers (OS) developed at the Monterey Bay Aquarium Research Institute may be useful in these studies to reduce expenses related to frequent field visits to obtain samples, and to increase temporal frequency for monitoring purposes. Dissolved gases utilized as added and intrinsic tracers may be collected with OS systems plumbed with gas-tight copper sampling tube coils and analyzed on a gas chromatograph or a mass spectrometer. Data from a subseafloor hydrothermal system study and parallel laboratory experiments provide an opportunity to evaluate field planning, analytical procedures, and challenges encountered in utilizing these devices for dissolved gas sampling. *In situ* pressures higher than those in the laboratory present a particular impediment to analysis of samplers deployed at depth, and "smearing" caused by diffusion and dispersion is found to exceed expected theoretical values. Best practices are recommended and theoretical

resolution specifications for a variety of common groundwater tracers and contaminants are presented.

Introduction

OsmoSamplers (OS) are osmotically-driven continuous water sampling devices developed at the Monterey Bay Aquarium Research Institute (MBARI) by Jannasch et al. (1994). By utilizing a hypersaline reservoir separated by membrane(s) from small-diameter sampling tubing pre-filled with deionized water, OS are able to continuously and autonomously sample water for years without requiring electrical or mechanical systems (Fig. 3.1). The water-filled tubing is cut into lengths (typically one meter) representing specific time periods, producing high temporal-resolution geochemical data. Jannasch et al. (2004) correlated pumping rates with fluid temperature and presented laboratory experiment results in support of an analytical solution for diffusion and dispersion of ionic solute gradients. These results are commonly cited in the methods sections of autonomous sampling studies utilizing OS.

Osmosamplers have been successfully deployed primarily in seafloor and oceanic hydrothermal systems (Fisher et al., 2005; Moyer et al., 2000), and also to monitor acid mine drainage (Chapin, 2015), and sample estuaries (Gelesh et al., 2016) and rivers (Gkritzalis-Papadopoulos, 2009). To date, documented OS deployments have sampled for dissolved ions (Jannasch et al., 1994), methane seepage (Lapham et al., 2013), noble gases (Tryon et al., 2012), and biological components (McQuillan and Robidart, 2017). Lacking in the literature is documentation of field and laboratory methods for the utilization of OS in continuous dissolved gas added-tracer studies.

This study utilized twelve OS devices for an added sulfur hexaflouride (SF_6) gas tracer experiment in a subseafloor hydrothermal circulation system on the eastern flank of the Juan de Fuca Ridge. These devices operated for time periods of one to four years. Upon retrieval, samples were analyzed on a gas chromatograph (GC) for SF_6. Approximately 1100 samples were analyzed, largely in sets of three consecutive samples representing two days each, separated by approximately fifteen-day intervals. Parallel field and laboratory studies and observations were conducted to verify the sampling and analytical methods.

Field Activities

Fourteen Osmosamplers were deployed from July 2010 through June 2019, constructed with coiled 300 m length 1.1 mm inner diameter (ID) copper sample tubing for dissolved gas analysis.

Three of the nineteen samplers were installed downhole, with four 300-meter coils of sample tubing attached in series to each sampler. These downhole samplers were calibrated to pump approximately 0.5 mL per day, corresponding with approximately 0.5 m of coil filled per day. They were suspended from the drillstring in each borehole and remained in operation for four years.

Pump rate calibration is vital to OS success. The pumping rate is controlled by both the osmotic membrane type and quantity and the ambient operating temperature, resulting in some uncertainty in the actual pumping rate for a deployment. The most robust method for determining pump rate is to locate the interface between the pre-filled deionized (DI) water and the sample fluid in the sampling coil after retrieval. The deployment and retrieval dates

provide the time of operation, and the interface location determines the length of coil filled, allowing the pump rate to be calculated and the location of any sample along the sampling coil to be transformed from a distance-along-coil to a date and time. Provided that the temperature was constant for the duration, the pumping rate remains unchanged during deployment due to the hypersaline reservoir maintaining saline saturation in the brine fluid.

If the actual pump rate is significantly greater than expected, and no excess coil was installed, the sampling coil may fill prematurely. If over-filled, the OS continues to operate normally, but the DI water is completely ejected, followed by the oldest portion of collected sample fluid. Without the DI – sample interface identifiable in the coil, determining the actual pump rate and thus timing of discrete samples along the coil is more difficult. Chemical analysis of the effluent and peak matching with properly functioning collocated OS systems allows for timing estimates, but uncertainties are greater (Neira et al., 2016). Of the fourteen OS systems deployed at our study site, only seven functioned as intended, allowing ample opportunity to investigate lessons learned.

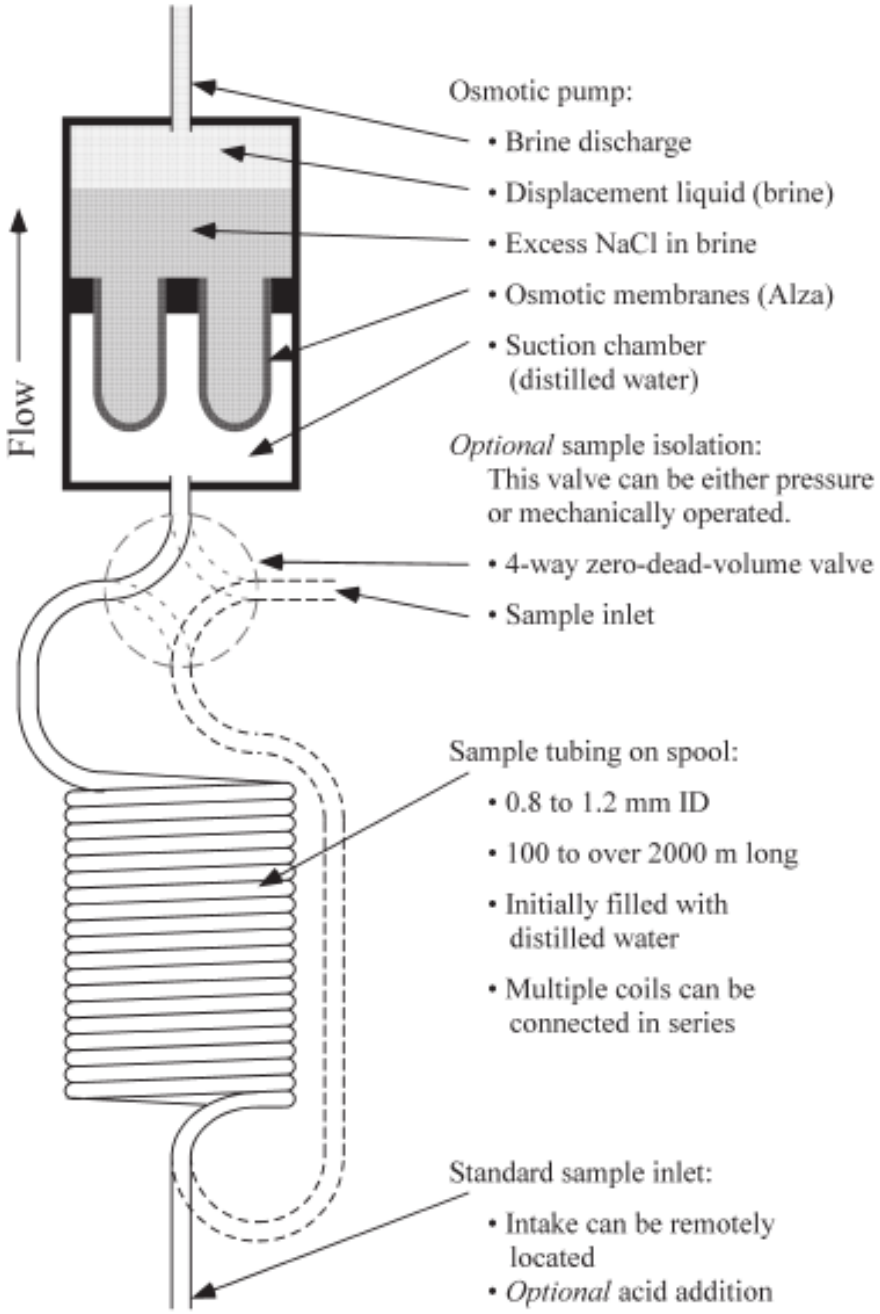

Figure 3.1 – OS schematic, from Jannasch et al. (2004): An osmotic pump consists of a rigid semipermeable membrane separating two chambers containing solutions of differing salinity. Flow rates are kept constant by maintaining freshwater and saturated brine with excess salt on either side of the membrane. OS use an osmotic pump to continuously pull fluid into a long micro-bore sample tube (0.5 to 1.2 mm ID). The pumps are attached either directly to a coil of tubing or through a 4-way sampling valve to prevent degassing during recovery. The tubing is initially filled with distilled water and deployed at any depth at ambient pressure.

Overpumping

Timing via locating the DI – sample interface was achieved on seven of the fourteen OS samplers deployed between 2010 and 2019. These systems pumped 0.35 – 0.70 mL/d, corresponding to 0.34 – 0.68 m of ~1.1 mm ID coil filled per day. Mathematically, an ideal 1.1 mm ID tubing would contain approximately 0.95 mL of fluid per meter of tubing, but an average one-meter sample from our ~1100 samples produced 1.04 mL with a standard deviation of 0.09 mL, indicative of poor manufacturing tolerances. Sampling coils installed with these OS pumps measured approximately 300 m in length per year of intended operation, equating to 624 days of sampling capacity at the ideal 0.5 mL/d pumping rate.

Of the seven OS systems that did not function ideally, one failed structurally at the membrane array. This could have been caused by construction flaws or bacterial colonization and consumption of the acetate membrane. Membrane failure reverses flow in the system as dense hypersaline solution descends and displaces sample fluid. In this case, the sample fluid was not completely displaced at the time of recovery. Sampled fluid was found adjacent to hypersaline fluid in the sampling coil with no DI water interval, indicating that the system had overpumped prior to the membrane failure. The length of coil installed required the OS to pump at least 0.86 mL/d for this to occur.

Three of the fourteem total OS systems functioned as intended but overpumped due to unforeseen circumstances. Systems installed in August 2011 were intended to function for one year but the 2012 *R/V Thompson* cruise was canceled. They were retrieved one year late, in September 2013. Considering the expense of installation and the value of the data, it would

have been prudent to install at least double the anticipated length of sampling tube. Space and other logistical concerns may preclude this, but best practice should be to provide a large buffer of sampling tube.

Four of the fourteen OS systems overpumped due to calibration errors. OS calibration via membrane configuration is well defined by Jannasch et al. (2004), making operating temperature the primary source of error. Average temperatures in these installations may have been as much as 10° C higher than predicted (Fig. 3.2). Such a difference should have been planned for; hydrothermal systems are unpredictable and disturbances such as drilling and opening and closing of borehole seals to install OS devices may have resulted in different conditions compared to static conditions before disturbances. Alternately, micro-scale degradation of the membranes caused by bacterial growth or other factors could have caused actual flowrates to exceed calibrated rates. As with the three OS that overpumped due to the postponed site visit, it would have been prudent to install excess sample tubing for at least a 2x safety factor, if space permitted.

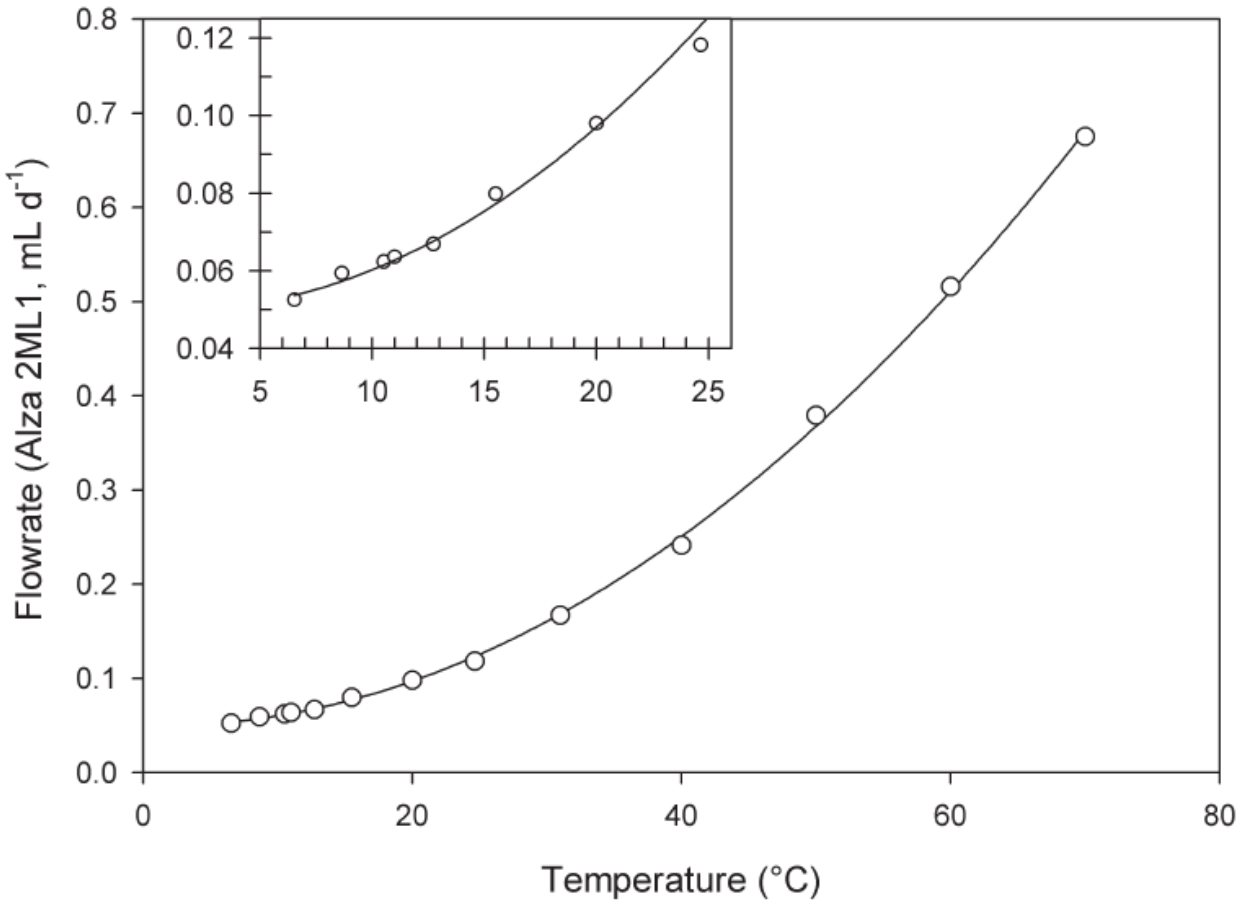

Figure 3.2 – OS Flowrate vs Temperature Calibration from Jannasch et al. (2004). For example, to achieve a flowrate of 0.7 mL/d from a system calibrated to pump 0.5 mL/d at 60° C, the actual operating temperature required is approximately 10° C higher.

Analysis Methods

Analyzing the samples from this nine-year record is a multistep laboratory process. To ensure continuity, procedures remained largely consistent with those developed by Neira (2014) and Neira et al. (2016), as those methods were used to analyze the first two years of this nine-year data series. Deviations from preexisting procedures and possible impacts are discussed in this paper.

The Neira (2014) method for extracting sample water from copper tubing was a three-day process. A coiled 300-meter length of tubing is measured and cut into 1 meter lengths, three lengths for every ten meters of coil, and sealed with steel clamp hardware often utilized to form a cold weld for noble gas intrinsic tracer sampling. On the second day, a small file saw is used to carefully open the sealed ends, with great care taken to ensure that the open ends are near circular. A nitrogen-filled syringe is then attached to the back end of the tube, and a needle affixed on the front. The needle is used to pierce a 10 ml Vacutainer blood serum vial, which draws the water into the vial, with nitrogen filling the excess space. After an overnight wait to allow full degassing of the water sample, the sample is run on the GC.

Here the procedure is truncated the first two days of this process into one, which may reduce the potential for SF_6 loss. As the coil is unrolled, targeted one-meter lengths are cut with perpendicular cutters, crimped open, and immediately extracted into Vacutainers. An audible release of pressure was often heard when a coil section was cut, due to overpressure at depth. By eliminating the additional cutting and overnight storage, gas loss from improper sealing is potentially reduced. Delicate use of plyers to cut and open tubing ends is faster than using a file saw to cut tubing ends, which results in less time with an imperfect seal that could also cause SF_6 loss due to rapid degassing. Once extracted, Neira (2014) methods were followed for overnight equilibration and GC analysis, though same-day analyses of a handful of samples suggests that extracted samples fully degas and equilibrate in as little as 20 minutes.

In all three cases where the Neira (2014) method was superseded by the truncated method, positive offsets in tracer concentration are observed, interrupting otherwise continuous trends (Fig. 3.3). As these three datasets are derived from three different systems,

two installed on the sea floor and one a controlled laboratory experiment, with the only commonality being the change in laboratory method, these results indicate that the new method reduces gas loss during analysis by up to 50%. However, the smoothness of the data suggests that the loss rate is static and predictable for these concentrations, therefor crucially preserving the concentration trends in our data. These results suggest that trend-based interpretations of these data are robust, but mass-based results calculated from data obtained with the prior method in Neira et al. (2016) should be adjusted to account for gas loss.

A sealed OS system was developed to study seafloor methane hydrate emissions (Lapham et al., 2013), designed to maintain *in situ* pressure, keeping methane in solution prior to analysis. A special crimping tool was used, tested to form a seal in copper tubing capable of withstanding up to 13.8 MPa pressure. Aliquots were extracted without manually breaking this seal, instead, samples were injected into vacuum containers via forcing the water with a tube roller until the pressure exceeded the strength of the crimped seal. In our study, low tracer concentrations were expected, so these procedures were not considered. In retrospect, it would have been prudent to take every precaution to avoid tracer gas loss.

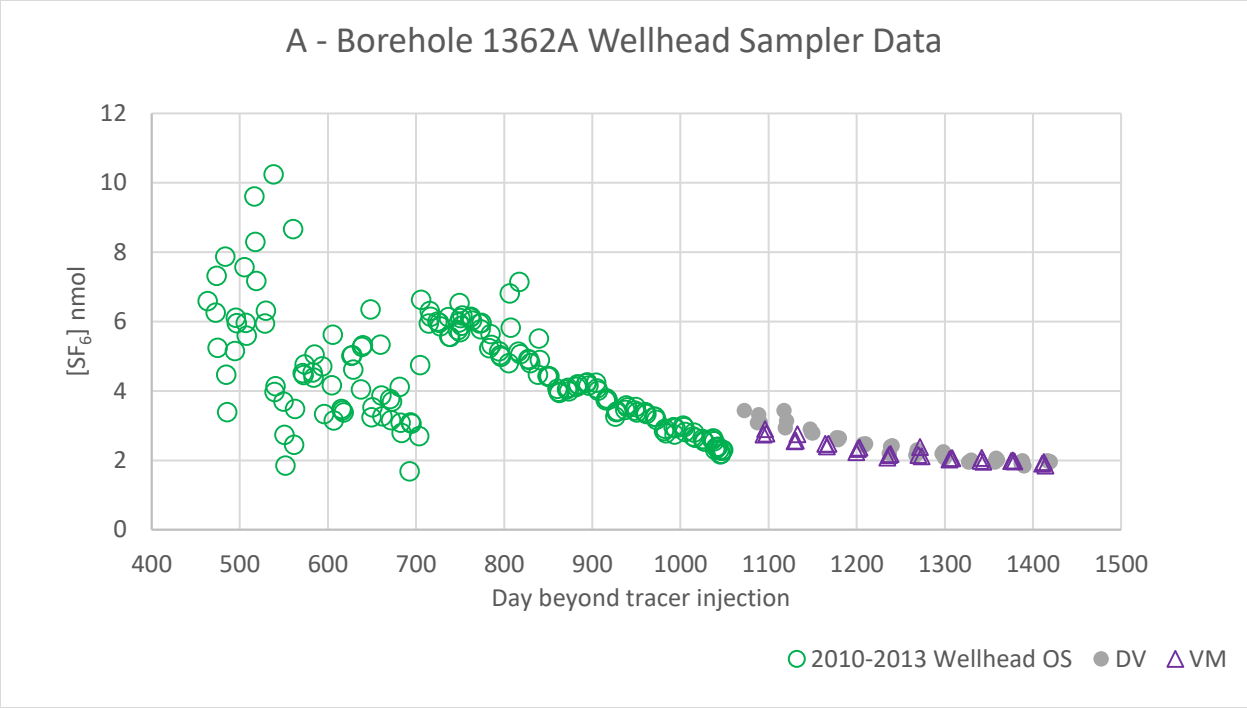
A - Borehole 1362A Wellhead Sampler Data
[SF6] nmol
Day beyond tracer injection
2010-2013 Wellhead OS
DV
VM

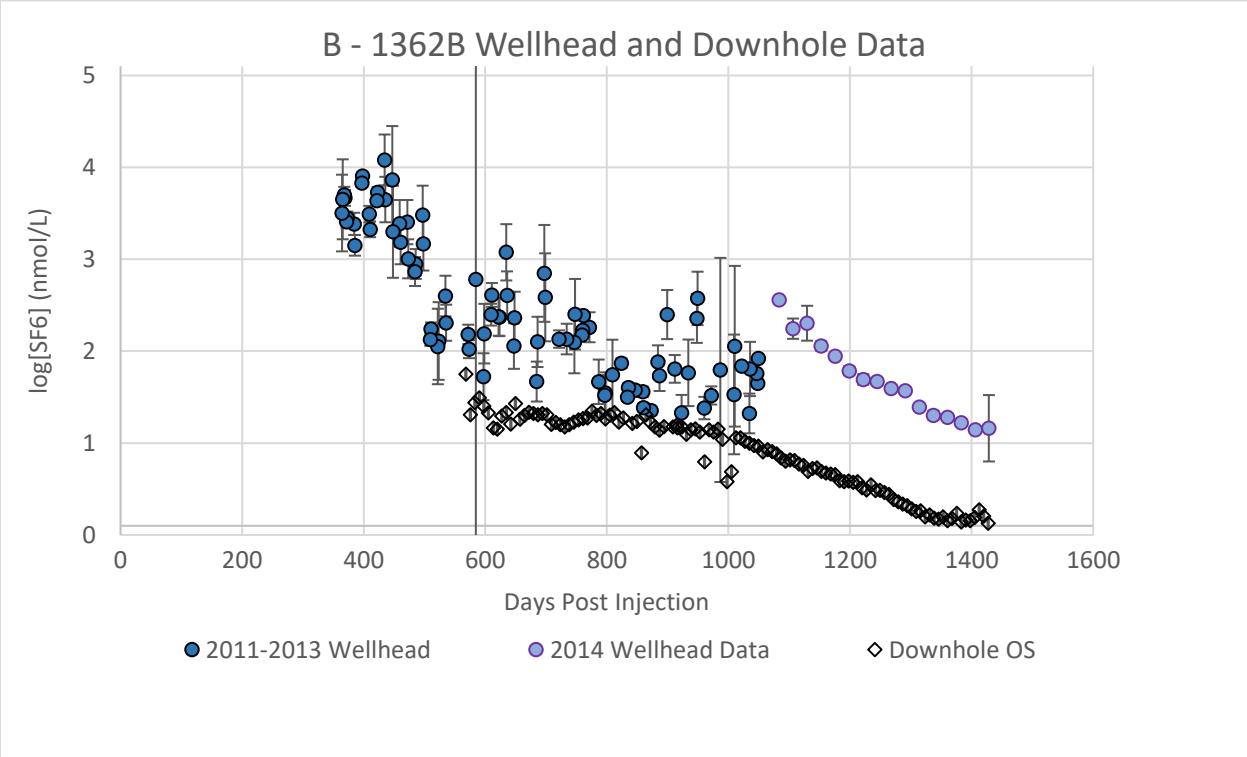
B - 1362B Wellhead and Downhole Data
log[SF6] (nmol/L)
Days Post Injection
2011-2013 Wellhead
2014 Wellhead Data
Downhole OS

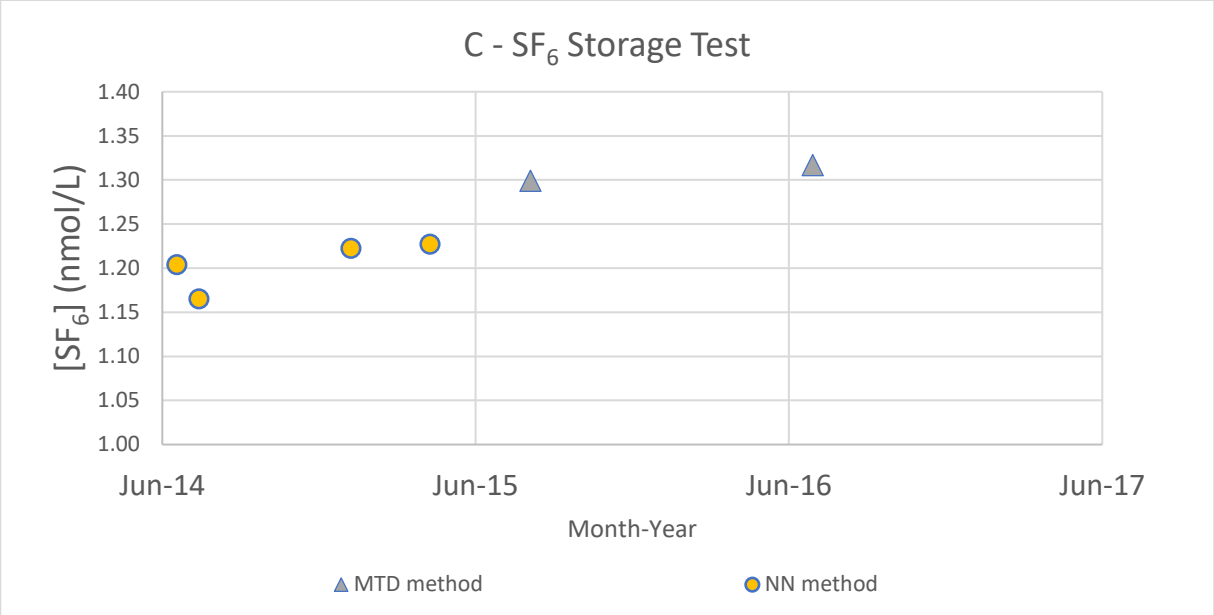

Figure 3.3 - Data discontinuity when sample preparation methods changed. A. Borehole 1362A 2013-2014 Vent Meter (VM) and Deep Vent (VM) data (new methods "MTD") vs 2011-2013 Wellhead Sampler data (old methods "NN"). B. Borehole 1362B 2013-2014 Wellhead data (new method "MTD") vs 2011-2013 Wellhead data (old method "NN"). Note continuity of Downhole Sampler data, which was continuously recorded and prepared with the MTD method. Data are presented as the average of three consecutive 1-m samples, with 1-sigma error bars. Standard error is high in 2011-2013 wellhead data due to leakage in fittings contaminating samples with seawater. Data were corrected via analysis of Mg-Ca ratios in samples compared to known values for formation water and bottom sea water, but this correction introduced additional error to the results. C. Storage Test results, 2014-2016. Plotted results are the average of three consecutive meters analyzed on each respective date. Sample preparation methods changed in September 2015; the 2016 analyses were performed on a different GC than the previous samples.

Gas Chromatograph Optimization

The GC system functions by transporting sample gas through a series of stainless steel loops and valves, through an atomic sieve separation column, and on to the GC itself for detection. A pressurized inert nitrogen environment is used to move a sample through the system, and various needle valves allow for fine-tuning of pressures within the plumping. Adjustments to these pressures and settings of the timing of valve throws via a BASIC timing

program on the Shimadzu Chromatopac PC control unit allow the GC system to be optimized to separate a single compound in a gas sample, and deliver it the detector. The atomic sieve was serviced in June 2015, optimizing its efficacy at separating compounds.

One source of analytical error is from improper zeroing of the GC. Detection peak intergrations on the GC are converted into SF_6 concentrations via comparison to calibration standard values, so if nitrogen blank "zeroes" are reading a number other than zero, this introduces a source of error. Here, great pains were taken to ensure that any standard or sample with an anticipated zero value returns an actual zero. These include nitrogen blanks, laboratory air samples, and nitrogen filled DI water blanks. Detections from these samples are understood to be air and water vapor detections due to improper pressure and timing settings in the plumbing and programming of the GC and controlling Chromatopac PC, so small adjustments have been made to eliminate these sources of error. Very small changes to pressure and timing settings can allow a small amount of air to be delivered to the detector along with SF_6, which results in additional background noise at best and a secondary peak at worst that must be manually observed and removed from reporting.

An additional source of error related to these calibrations is from poor pressure and valve timing complicating the automatic integration of detection peaks. If the detection peak arrives on a smooth portion of the "zero" curve, the Chromatopac can easily differentiate the detection curve from the preexisting trend and accurately integrate the area, which is converted into SF_6 concentration. Problems arise when the initial setup parameters result in the SF_6 detection peak arriving superimposed on a dip or peak in the "zero" curve, which are artifacts of pressure changes when valves change position as the plumbing system cycles a

sample through. In such a case, the Chromatopac may not be able to accurate assess what part of the detection peak is in excess of the “zero” curve resulting in an incorrect value being attributed to the area within the detection peak. As with ensuring that all blank samples produce true zeroes, optimization the GC to minimize errors in peak area integration were conducted.

Daily Calibrations

Concentrations of SF_6 in samples are determined by analyzing standard SF_6 gases and fitting an equation to the graph of the SF_6 standard concentration versus the area under the detection peak. The GC is generally consistent as long as pressure and timing settings are static, but even so, daily drift occurs. Neira (2014) method was to run daily calibrations to verify that the GC detector output was similar enough to an initial calibration curve produced early in her work, but no specification was listed for what statistically constituted a value close enough to the calibration values. In place of using a single calibration curve relationship, standard gases were analyzed on each day that sample analyses took place in order to use a unique daily calibration curve for each sample run.

Validation

All the above modification to Neira (2014) method have increased the accuracy and precision of data from the GC. None of the modification invalidate data produced prior, but the improvements, which are estimated to be in the 1%-3% range for each modification, potentially

add up to enough cumulative increase in analytical performance to explain at least part of the noticeable difference in triplicate clustering and data scatter between prior work and data from 2015 analyses. These improvements must be considered when making conclusions about the aquifer system, i.e. without knowing that analytical precision has been increase, one might erroneously conclude that the shallow zone sampled by the wellhead sampler systems are inherently more chaotic. This may still be the case, but analytical precision issues may play a part in the data scatter as well.

Analytical work and method modifications are validated by good scientific method procedures. Sample were not run in consecutive numerical order, single-coil analyses were run across multiple days with unique calibration curves for each day, and some of the prepared Vacuatainers were retained for several weeks before testing. These methods eliminate the possibility of daily or long-term drift causing artificial trends in data, and are validated by very good triplicate clustering and excellent continuity in trends within individual coils and across multiple coils from the same wells. In June 2015, near the middle of sample analyses for the 1362B Downhole samples, the GC had to be complete reset due to a planned power outage. Even with this hard reset of all GC nitrogen pressure settings and valve timings, which resulted in a dramatic change in detector output in response to SF_6 standards, trend continuity in 1362B was excellent.

Sample Archiving

An additional finding invalidates the prior sample archiving methods. One-meter lengths of coil are commonly analyzed, but analysis for daily (~1 m) temporal precision is time consuming and often not necessary. Instead, three consecutive 1-meter sections are analyzed at intervals of 10 to 20 meters. The remaining sections are archived for possible future analysis. Intact stored coils and pre-cut lengths of coil were stored sealed on both ends with machined steel noble gas sampling clamps that cold weld the thin copper coil into an effective seal, but the hundreds of archived sections of coil leftover interval analyses precluded the use of expensive machined clamps for archival purposes. Instead, plyers were used to doubly crimp the coils at both ends and attempt to form a similar cold weld seal.

In an attempt to verify prior results and support procedural changes, approximately twenty archived sections of coil were prepared and analyzed in 2015. The adjacent meters of coil to these had been analyzed in 2013 and 2014, producing the results reported in Neira (2014) and Neira et al. (2016). Those prior analyses all detected SF_6, with some detections higher than any samples analyzed in 2015.

When archived samples were tested for SF_6 in 2015, no samples contained detectable quantities of SF_6. We conclude that crimping coils with plyers does not form a seal that prevents SF_6 from escaping. Unfortunately, this finding was made most of the way through the additional sample analyses, so archived coil sections adjacent to sections analyzed in 2015 are also not useful for SF_6 verification. In their paper documenting methods with dissolved ion analytes, Jannasch et al. (2004) only recommends that tubing be “pinched”, which appears to

be adequate for such analyses. Our samples were retained for other analyses, as the crimped sealing method is effective for retaining water and dissolved solutes in the coils, provided the solutes do not become volatile at 1 atm. Such an analysis was performed without complication for a dissolved cesium salt tracer injected in parallel with our SF_6 tracer. The strength of our seals should have been tested following the procedures from Lapham et al. (2013) to ensure preservation of dissolved SF_6.

Continuity Between Coils

The earliest wellhead OS systems installed at site 1362B in 2011 suffered from plumbing leaks that allowed ocean bottom water to dilute the formation water samples, complicating data interpretation (Fig. 3B). Systems installed downhole in 2010 and at wellheads in 2013 and 2014 had no such issues. Major ion concentrations were consistent with hydrothermal formation water, and, in the case of the downhole samplers, excellent continuity was achieved between sampling coils assembled in series. Continuity appears to be briefly lost in the first and last ten to twenty meters of in-series coils, likely caused by delayed sealing when the coils were disconnected. This is especially apparent at the beginning and end of coil 4 and the end of coil 3, seen at approximately 1200 m, 900 m, and 600 m (Figure 3.4), and supports the need to minimize gas loss during preparation and analysis procedures. Trend continuity returns after 10-20 meters, so minimal temporal resolution is lost by discarding data from that interval.

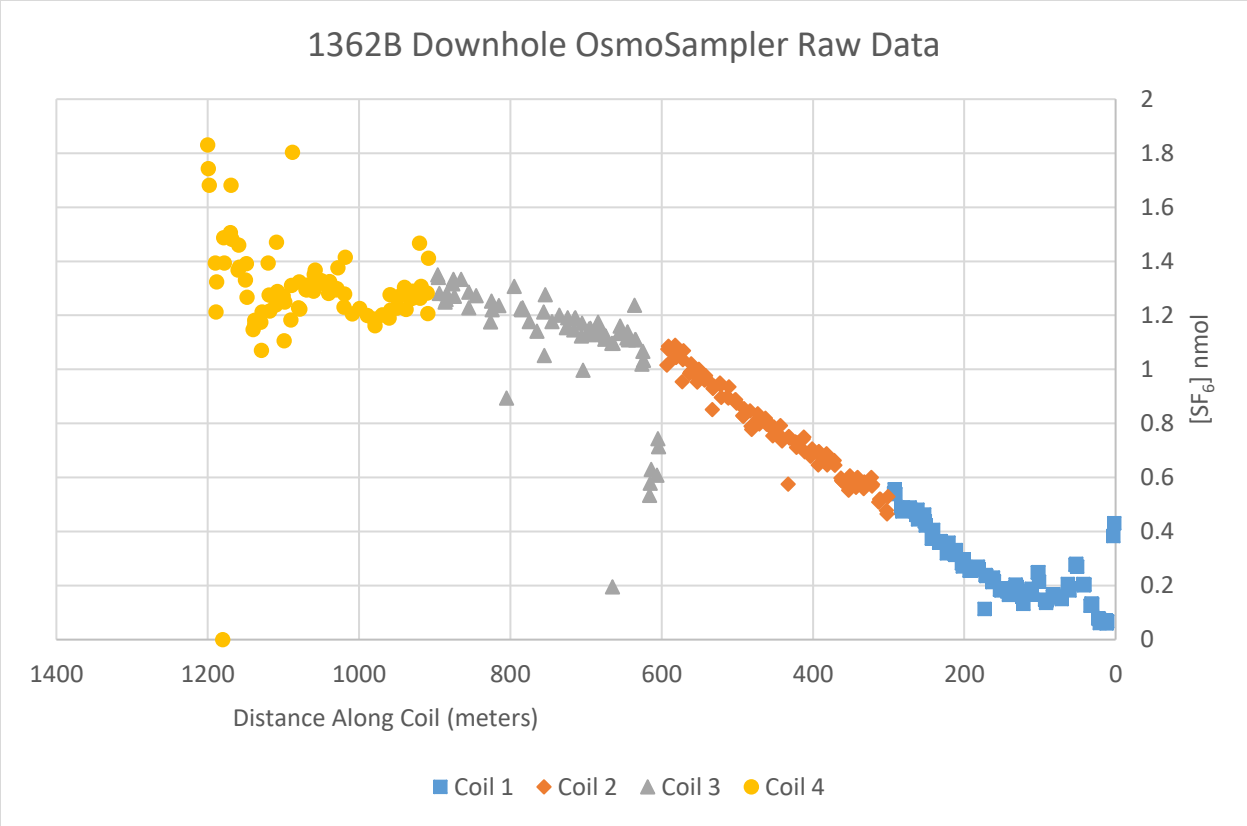

Figure 3.4 – Continuity between in-series sampler coils. Sample loss at coil ends due to faulty connectors or inadequate sealing during storage is present, but general continuity is apparent.

Duplicate Record

On one wellhead serviced in 2013, two wellhead OS systems were deployed. These were intended to sample from different locations in the borehole, but were erroneously plumbed to sample from the same location, providing an opportunity to assess replicability. Both curves matched, with only a slight offset between the two at higher concentrations (Fig. 3.5). From these duplicate datasets, it is reasonable to conclude that sampling and analytical methods are sound and replicable.

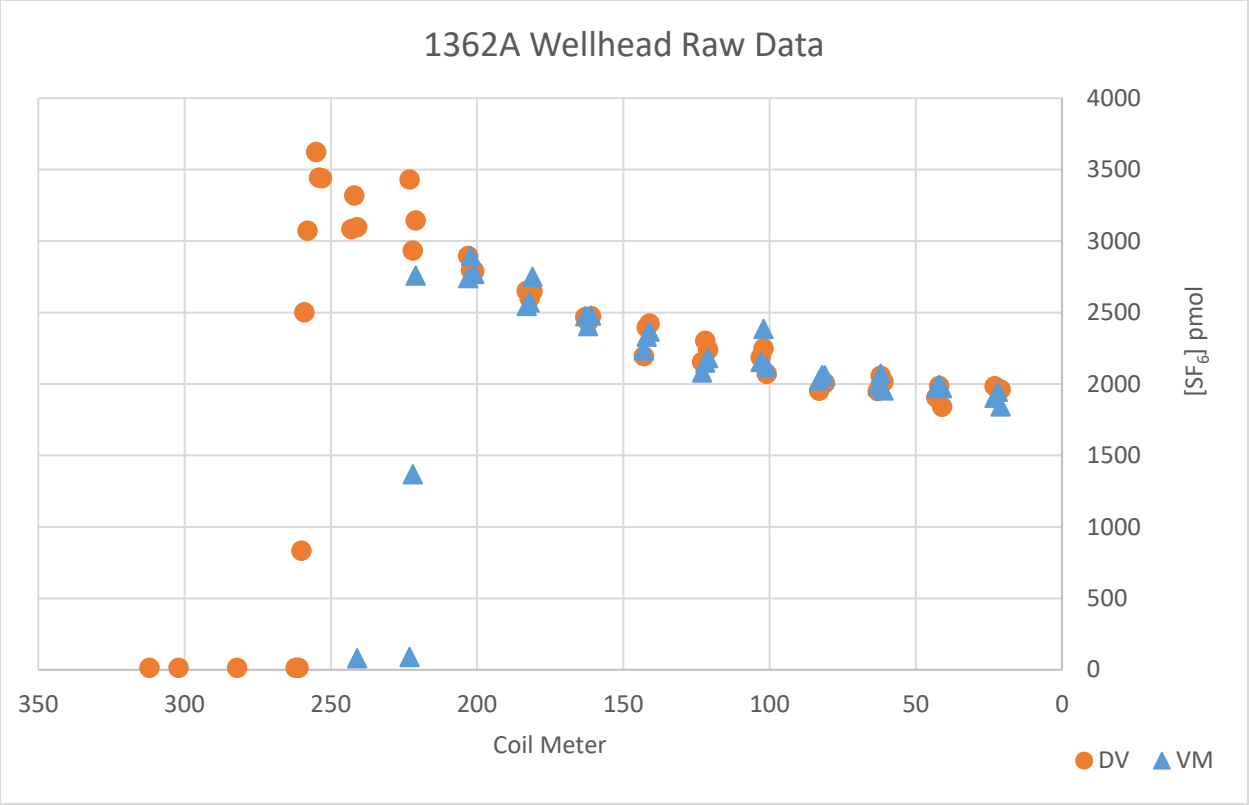

Figure 3.5 – Duplicate samples from Borehole 1362A Deep Vent (DV) and Vent Meter (VM) samplers.

Laboratory Equipment Rest

In April 2015, a sample loading error flooded part of the GC plumbing with water, necessitating an unplanned shutdown of the GC while it dried out. This interrupted sample analysis at meter 101 of the 1362B downhole coil 2, corresponding to cumulative sample meter 401 on Figure 3.4. The uncut portion of the coil was clamped with NG clamps for storage, but some samples had already been loaded into Vacutainers.

When analyses resumed approximately one month later, data showed excellent continuity despite the interruption. There was some concern that sensitivity drift in the GC

could affect results over time, but results from this unfortunate interruption demonstrated that with proper GC calibration and sample storage procedures, dissolved gas tracer analyses can be robust. Further supporting this assertion, some samples were run on an alternate GC machine, yielding equally continuous data.

Storage Test Results

Concurrent with sample analysis, a controlled storage test has been conducted. A homogenized solution of SF_6 dissolved in deionized water was prepared in early July 2014. This solution was loaded into a length of new copper tubing identical to the coils attached to the OsmoSamplers in the field.

The storage test tubing was stored similar to the field samples with noble gas sampling clamps sealing both ends. Periodically, a 3-5 m length of tubing was removed, and the water extracted and analyzed via the standard method. The most recent analysis was completed in July 2016, and results indicate no reduction in SF_6 concentration during the two-year duration of the test. Over the two-year duration, storage test samples were analyzed at long intervals, with different equipment settings, and even on two different GCs, as one experienced an electronics failure in 2016 so another was brought online. These results (Fig. 3C) help validate the GC calibration and analytical procedures.

Additionally, storage test results obtained through June 2015 were prepared using Neira (2014) methods. Though these results are internally consistent, showing no sample loss trend, samples beyond that point were prepared using the truncated method described above.

Results yield an apparent increase in concentration of approximately 9%. It is highly unlikely that the increase is real, and more likely related to the changes in method as described above, so this result supports the truncated methods and validates the storage procedure.

As OS's were retrieved from the seafloor in August 2014 and sample analysis was completed less than two years later in December 2015, the storage test results validate the storage method for field samples, indicating no tracer loss during extended storage.

Dispersion and Temporal Resolution

As has been the case with other OS experiments in the literature, our study was largely planned using Jannasch et al. (2004) as a reference. One concern when deploying a long-term OS device is "smearing", which is a loss of temporal resolution due to dispersion and diffusion of fluid and dissolved components within the OS coil. These effects are a result of two processes: molecular diffusion of a dissolved component due to concentration gradients, and dispersion caused by interactions with the coil walls as the fluid is continuously pumped through the coil. Jannasch et al. (2004) conclude that these effects are minimal, largely due to the small ID of the coil, and presents theoretical calculations and laboratory experiments that have been referenced to plan this and other experiments. What seems to have been overlooked is that Jannasch et al. (2004)'s oft-cited figure is only one set of calculations using "typical" dispersivity and diffusivity values for dissolved salt ions near room temperature.

Jannasch et al. (2004) calculated resolution using "typical" dispersion values at room temperature for a theoretical interface between DI water and saline solution. Using the

empirically-derived diffusion coefficient D_m of a solute, the diffusive step change in concentration across an initially planar interface is describes by an analytical solution derived from Fick's Law (Crank, 1975).

$$C(x,t) = \frac{C_0}{2}\,\mathrm{erf}\left(\frac{x}{2*\sqrt{D_m t}}\right) \quad (3.1)$$

This process occurs when fluid is pumped through tubing, motion-driven dispersion also contributes to smearing. Taylor (1953) derived an effective diffusion coefficient k, taking into account variations due to tubing radius (r), pumping velocity (v), and solute molecular diffusion coefficient (D_m).

$$k = \frac{r^2 v^2}{48D} \quad (3.2)$$

Peak gradient smearing attributed to both gradient- and flow-driven processes is approximated by summing D_m and k to obtain a combined effective diffusivion coefficient (k').

$$k' = k + D_m \quad (3.3)$$

Inputted in Eq 3.1 in place of D_m, *k'* allows smearing to be modeled. For their "typical" case, Jannasch et al. (2004) used D_m = 1.5 x 10^{-5} cm^2/s, approximately the diffusion coefficient of NH_3, and a 1.1 mm ID tubing pumped at 1 m/d. This indicates that after one year, 99.9% of the interface concentration will be contained within ± 1 m of the interface, thus giving a 2 m coil resolution.

When the calculations are redone with values appropriate for SF_6 at 65° C (Bullister et al., 2002; King et al., 1995), the operating temperature at our hydrothermal site, and 0.5 m/d pumping rate, this 99.9% resolution decreases to ± 1.5 m, indicating a resolution of 3 meters

after only one year of operation. At a 1 m/d pumping rate, this resolution would be further decreased to 4.6 m. Our downhole samplers were operating for four years, resulting in a theoretical resolution of approximately 6 m at 0.5 m/d pumping rate. When a year of diffusion during storage (prior to analysis) is included, this resolution decreases to 6.2 m. At pump rates of ~0.5 mL/d, this equate to smearing over 12.4 days at the oldest end of the coil. The youngest portion would effectively only be diffusing for one years, increasing the resolution to ± 2 m, or 4 days. In homogenous systems, this could manifest as artificial smoothing of data, but the natural variability produced by heterogeneous flowpaths is high in our fractured rock aquifer study site, and is well preserved (Fig. 3.4).

Temporal Resolution of Common Dissolved-Gas Analytes

Studies have proven OS to be effective in long-term autonomous deployments sampling for dissolved gases in water. In future deployments, care should be taken to design systems (pumping rate, tubing ID) specifically for the intended dissolved gas analyte and desired temporal resolution. Expanding from Jannasch et al. (2004)'s theoretical resolution of a "typical" ionic tracer, we present theoretical resolutions for various potential analytes. Noble gases and sulfur hexafluoride are useful as non-reactive conservative groundwater tracers (Clark et al., 2005; Visser et al., 2014) and a selection of other common analytes used for groundwater age and water quality are presented here, as OS could potentially be of use for long-term monitoring of groundwater transport dynamics and contamination levels.

Graphically, the difference between Jannasch et al. (2004)'s "typical" solute and dissolved gases is subtle (Figure 3.6), but the resulting resolution varies from 2 m ("typical") to 4.5 m (helium), a discrepancy which should be taken into account when interpreting results. These examples (Table 3.1A, 3.1B) use the diffusion coefficients for gases at 25° C, chosen because it is within the expected temperature range for groundwater tracer studies in the American Southwest. A positive correlation exists between temperature and diffusivity, so planning for studies sensitive to temporal resolution should evaluate the theoretical resolution of their system using specified parameters. For example, water quality analyses that require several milliliters of water might require more rapid pumping rates or larger ID tubing, which would result in poorer temporal resolution. In this 9-year hydrothermal system tracer study, resolution beyond 10 days is not necessary, but if OS were to be deployed for terrestrial groundwater contaminant or tracer monitoring, resolution may be more sensitive.

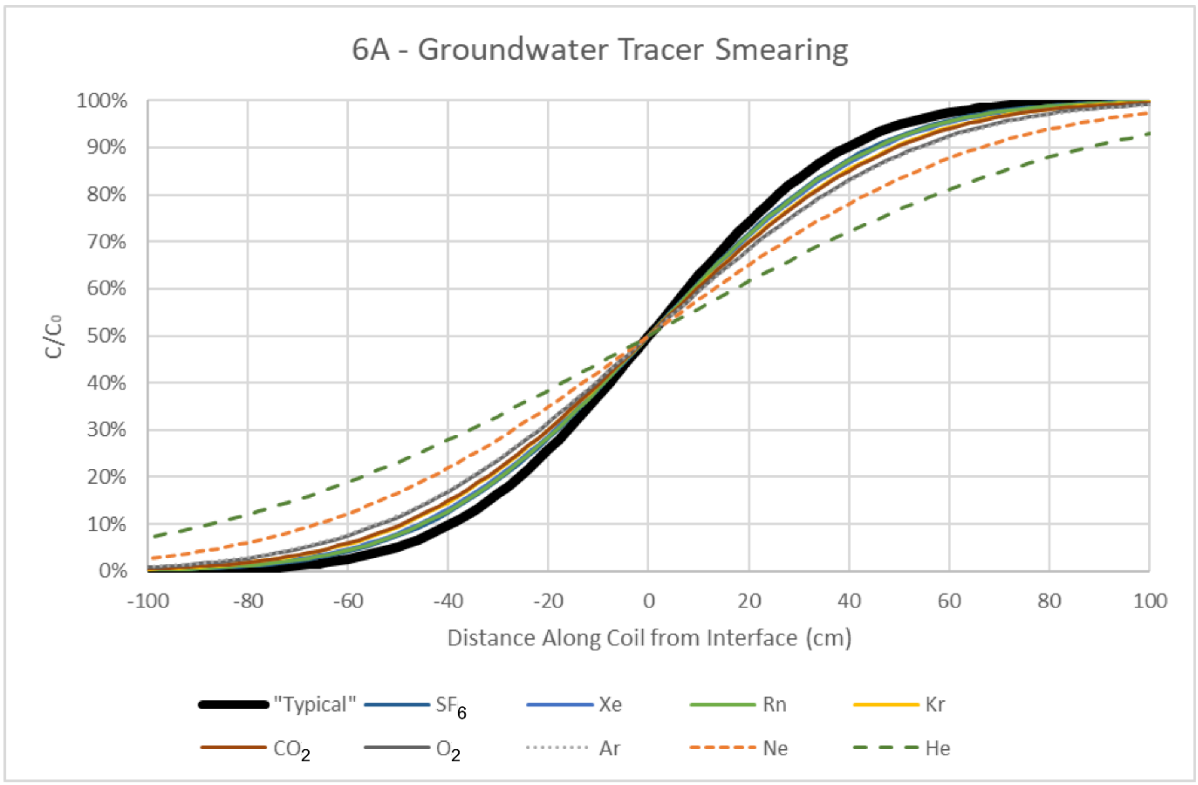
6A - Groundwater Tracer Smearing
100%
90%
80%
70%
60%
50%
40%
30%
20%
10%
0%
C/C₀
-100
-80
-60
-40
-20
0
20
40
60
80
100
Distance Along Coil from Interface (cm)
"Typical"
SF6
Xe
Rn
Kr
CO2
O2
Ar
Ne
He

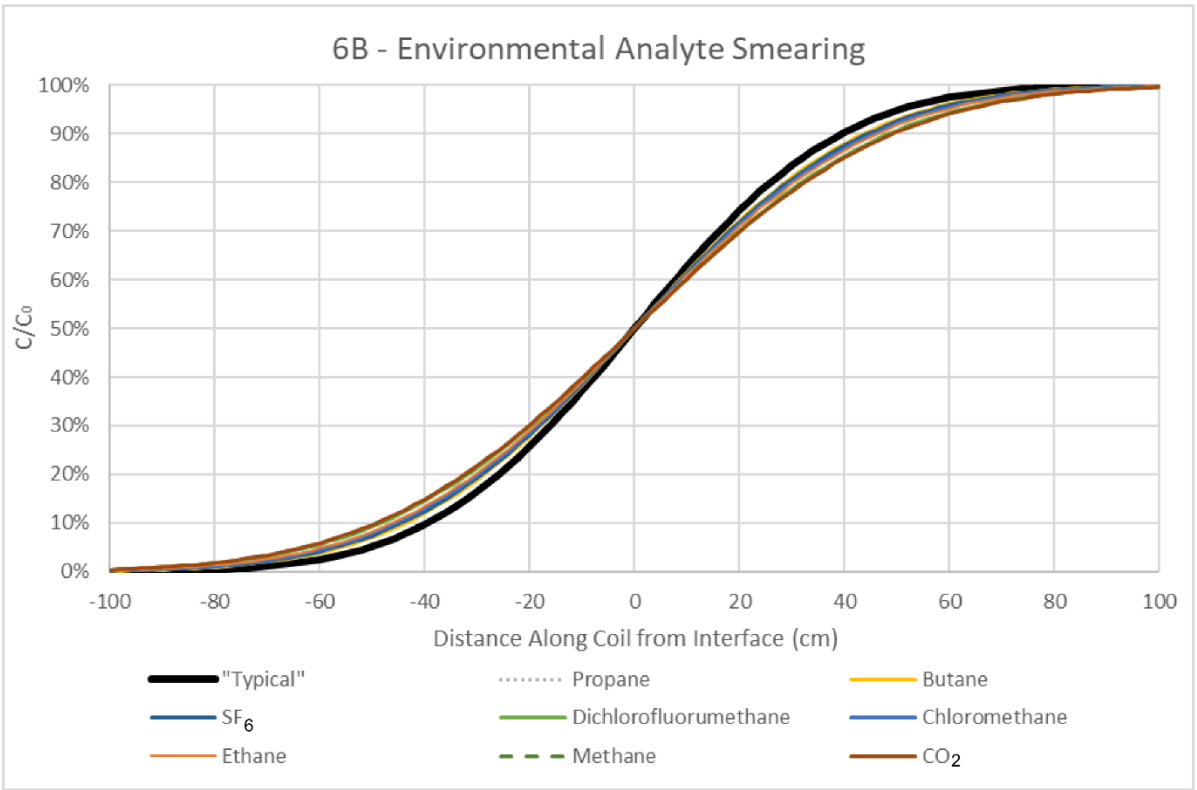
6B - Environmental Analyte Smearing
100%
90%
80%
70%
60%
50%
40%
30%
20%
10%
0%
C/C₀
-100
-80
-60
-40
-20
0
20
40
60
80
100
Distance Along Coil from Interface (cm)
"Typical"
Propane
Butane
SF6
Dichlorofluorumethane
Chloromethane
Ethane
Methane
CO2

Figure 3.6 – Theoretical smearing of groundwater tracers (A) and common environmental analytes (B).

Table 3.1A – Temporal Resolution of Groundwater Tracers. Data presented for 1.1 mm ID tubing pumped at 1 m/d at 25° C. Resolution defined as length of tubing containing 99.9% of original composition. A positive correlation exists between all three parameters and temporal resolution.

	He	Ne	Ar	Kr	Xe	Rn	SF_6	CO_2	O_2	"Typical"
D (cm^2s^{-1} x 10^5)	7.28	4.03	2.50	1.84	1.47	1.33	1.21	1.91	2.42	N/A
k' (cm^2s^{-1} x 10^5)	6.39	3.66	2.45	1.99	1.77	1.70	1.65	2.03	2.39	1.50
Resolution (d)	4.48	3.40	2.78	2.50	2.36	2.30	2.28	2.52	2.74	2.00

Table 3.1B – Temporal Resolution of Common Water Quality Analytes. Data presented for 1.1 mm ID tubing pumped at 1 m/d at 25° C.

	Methane	Ethane	Propane	Butane	Chloro-methane	Dichloro-fluorumethane	SF_6	"Typical"
D (cm^2s^{-1} x 10^5)	1.88	1.52	1.21	0.96	1.40	1.80	1.21	N/A
k' (cm^2s^{-1} x 10^5)	2.01	1.79	1.65	1.59	1.73	1.96	1.65	1.50
Resolution (d)	2.52	2.38	2.28	2.24	2.32	2.48	2.28	2.00

Dissolved vs Exsolved Gas and Pressure Implications

The above calculations show that SF_6 theoretically experiences greater smearing than assumed from the "typical" values used in Jannasch et al. (2004), complicating interpretation of OS results for dissolved gas. On our two duplicate sampler coils, 1362A Deep Vent and 1362A Vent Meter, samples across the sample-DI interface were analyzed, replicating Jannasch et al. (2004)'s laboratory experiment with our field samples. These samplers were deployed for one year and were analyzed less than one year after retrieval. They exhibit dispersion in excess of all models for that timespan, visually aligning to the 3-year dispersion solution (Figure 3.7), which

indicates that resolution is 3 m, or approximately 5 days at the rate these systems pumped. These samplers were in contact with 2° C bottomwater, a temperature at which the theoretical SF_6 dispersivity is less than the "typical" ionic solute value, so minimal smearing was expected. This suggests that other variables effect dispersion in this dissolved gas sampling system.

Dissolved gas studies are often conducted in deep sea or deep aquifer environments, under much higher pressure than in the laboratory. SF_6, while a gas at 1 atm, is a liquid at ~200 atm where our samplers were deployed. Estimated diffusion coefficients for SF_6 in the liquid phase are not available, but liquid-phase diffusion is generally orders of magnitude less than in gas-liquid phase diffusion, so these results are surprising. Dynamics not taken into account by the theoretical dispersion equation could be producing the enhanced smearing seen in the field samples. Designing a laboratory experiment to test this hypothesis is not possible with our present equipment, and is a study that should be considered in the future. In this paper, one example is the difference in method-change offset between the storage samples and the field samples: the storage samples, prepared at 1 atm, showed a ~9% increase, but the field samples showed a 40-50% increase, presumably because the pressurized system was more susceptible to gas loss. In the absence of controlled experiments, future OS deployments sampling for gases at depth should work under the assumption that temporal resolution is significantly poorer than theoretical estimates.

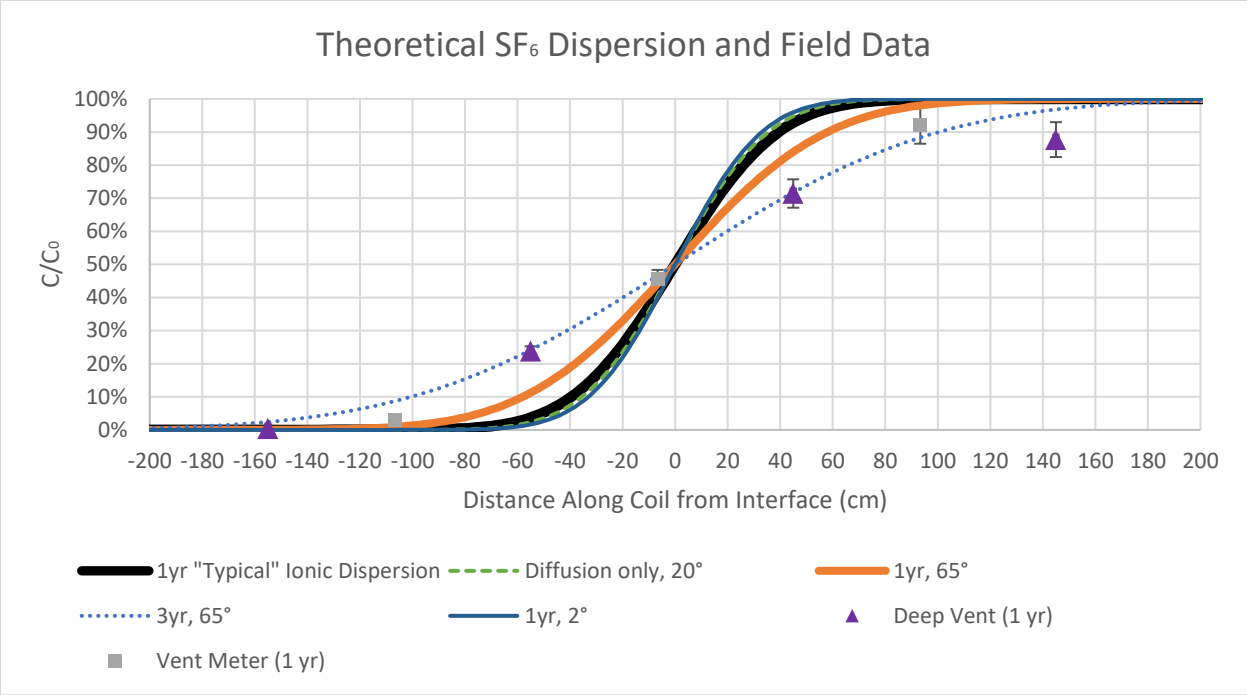

Figure 3.7 – Theoretical smearing of SF_6 at 65° after 1 year and 3 years of OS operation, 2° C for 1 year, diffusion due to storage for one year at room temperature, and "typical" dispersion as reported by Jannasch et al. (2004); compared to field data obtained from two wellhead-mounted OS. Both samplers were in contact with 2° C bottom water, so much lower smearing was expected. Error bars are 3-sigma analytical uncertainty.

Summary and Best Practices

This study utilized 12 OS deployed to study hydrothermal circulation on the Eastern Flank of the Juan de Fuca Ridge via an added sulfur hexafluoride gas tracer experiment. The planning, sample preparation, and analysis procedures were examined to identify potentially significant differences from procedures documented for ionic solutes in Jannasch et al. (2004). A storage test validated the long-term viability of OS data, but attempts to analyze archived samples demonstrated that procedures for dissolved gas tracers are different than those for ionic solutes. In two OS coils, our analyses across the sample – DI water interface indicated that smearing is greater than theoretical calculations predict, and differences between dissolved

compounds warrant examination rather than relying on the “typical” case presented in Jannasch et al. (2004).

Based on our observations, we recommend the following Best Practices for OS field deployment, sample preparation, and analysis when utilized with dissolved gases:

Pre-Deployment

- Calculate theoretical smearing for specific analyte properties, OS specifications, operating temperature
- Include 2x anticipated sampling coil to account for differences in calibrated pumping rate
- Duplicate systems for long term studies in case of membrane failure

Preparation, Analysis, and Data Interpretation

- Use noble gas clamps for archiving and storage
- Expediently cut coil and load to gas-tight containers to reduce gas loss, or follow Lapham et al. (2013) procedures to ensure optimal data quality
- Temporal resolution may be worse than theoretical estimates

Chapter 4

Implications of a Cross-Hole Subseafloor Tracer Injection Experiment on the Effective Porosity and Anisotropy of a Hydrothermal System, Juan de Fuca Ridge Flank

Abstract

Until recently, oceanic crust aquifer properties were estimated from single-borehole experiments and mathematical modeling. Here we present multi-tracer data from a cross-borehole tracer experiment in a hydrothermal system on the eastern flank of the Juan de Fuca Ridge. A rapid tracer breakthrough induced by a ~570 m^3 fluid injection suggests that effective porosity is several orders of magnitude lower than bulk material porosity and ridge-parallel anisotropy may have a large effect on fluid flow in shallow ocean crust. The low effective porosity precludes application of the conventional point-source model for tracer experiments and necessitates the development of a new conceptual model to explain observed tracer breakthroughs and derive aquifer properties. The average linear flow velocity at this site is found to be ~1 m/d. At the 10^2 – 10^3 m scale encompassing this field site, we constrain a representative elemental volume (REV) for future use in more accurately modeling oceanic crust as a porous medium.

Introduction and Setting

The International Ocean Discovery Program (IODP) and its precursors have visited the Juan de Fuca Plate seafloor on several scientific cruises over the last three decades. Among other areas of research, IODP studies have sought to enhance our understanding of subseafloor

hydrothermal systems through heat flux surveys (Fisher et al., 2003), the collections of sample transects (Elderfield et al., 1999), borehole drilling (Davis et al., 1991), and seafloor observatory installations (Davis et al., 1996). In August 2010, IODP Expedition 327 initiated a project to explore hydrothermal aquifer properties via multi-borehole tracer-injection experiments.

The setting of this study is on the eastern flank of the Endeavor segment of the Juan de Fuca spreading center, approximately 230 kilometers west of northern Washington State (Figure 4.1). At this rift zone ridge, new basaltic oceanic crust is continually created, with the eastern half being conveyed eastward to eventually be subducted under the North American plate at the Cascade Subduction Zone, giving rise to the Coast Ranges and volcanic Cascade Mountains in the Pacific Northwest (MacDonald, 2001).

Where exposed, ocean bottom water infiltrates the porous basalt driving hydrothermal flow. Continental sediment covers the Juan de Fuca plate to a depth of several hundred meters, confining the flow and insulating the system (Griggs et al., 1969). Away from the ridge axis, topographic basement highs protruding above the sediment may act as either recharge or discharge locations, driving low-temperature ridge-parallel convection systems operating on a scale of tens of kilometers (Fisher et al., 2003; Winslow et al., 2013; Winslow et al., 2016).

Four boreholes equipped with sealed borehole observatories ("CORKs") were instrumented with autonomous osmotically-driven OsmoSamplers that were utilized to collect formation fluid for this study (Jannasch et al., 2004). These installations function to seal open boreholes, vital to studying natural conditions in this confined hydrothermal system, and facilitate research activities via engineered reentry cones and platforms on the seafloor.

Dissolved sulfur hexafluoride gas[1] (SF_6), cesium (Cs), and plastic microspheres were injected into a single borehole over a twenty-four hour period beginning on August 23, 2010. Nine years of autonomous fluid sampling followed, with site visits in 2011 and 2013 to retrieve samples and download temperature and pressure loggers from the seafloor platforms and conduct additional experiments. Neira et al. (2016) presented data and interpretations from these visits. In August 2014, additional sampling systems, including downhole OsmoSamplers were collected from the project site. In June 2019, two remaining sampling systems were retrieved. As of this publication, no samplers are currently installed at the site. This paper presents new results and interpretations from the complete nine-year data record.

Methods

Field Methods

This study utilizes four IODP boreholes located along a buried basement ridge between two basalt outcrops, Baby Bare and Mama Bare (Figure 4.1), which function as discharge points, driving a flow system conducting hydrothermal water in a northeasterly direction away from Grizzly Bare, a primary recharge outcrop 52 km to the southwest (Wheat et al., 2008; Fisher et al., 2003; Hutnak et al., 2006). The tracer study commenced in August 2010 and concluded with the removal of all sampling equipment in June 2019. Various wellhead samplers operated

[1] While SF_6 was introduced as a gas on the drill ship, it would have condensed into a liquid due to pressure at depths greater than approximately 160 m water depth,so it should behave as a gas solute tracer in the seafloor.

for the duration of the experiment, but downhole samplers were only deployed between 2010 and 2014.

SF_6, Cs, and plastic fluorescent microbead tracers were injected into borehole 1362B. Prior to beginning the experiment, samplers were installed in the injection borehole, two downgradient boreholes (1362A and 1026B), and one upgradient borehole (1301A). The distances between these holes varied from approximately 235 m to approximately 550 m (Figure 4.1). The fine-grained sediment above the basalt basement is approximately 200 - 300 m thick in the study area, and the holes extended 48 m to 292 m into the basement aquifer (Figure 4.2).

Geochemical tracer samples were obtained from high-resolution Osmosamplers that function to continuously filled small diameter copper and plastic tubing stored in coils both at the wellheads and suspended from the drillstring inside the borehole. These sampling devises require no power; they operate using the principle of osmotic pressure. The small inner diameter (<1 mm) limits longitudinal smearing and diffusion, producing a temporal resolution <10 days, depending on timing and ambient temperature conditions (Jannasch, et al. 2004). Deionized (DI) water is pre-loaded into the tubing, which is drawn into a hypersaline reservoir across a membrane system or pump.

In the summer of 2010, a tracer injection occurred at borehole 1362B. Surface seawater was pumped downhole for 24 hours at ~6.7 L/s, totaling ~570 m^3 fluid injected (borehole volume = ~21 m^3). For 7 minutes at 3 hours into the injection and 8 minutes at 19 hours into the injection, cesium chloride (CsCl) salts were added to the injectate. Other metal salts

injected included erbium chloride hexahydrate (ErCl3·6H2O), and holmium chloride hexahydrate (HoCl3·6H2O). Fluorescent microspheres and stained bacteria were injected from hours 20-21.5, and freshwater was injected in place of seawater from hours 1-2 and 20-21.

Ball valves installed on borehole 1362A and 1362B CORKs were operated to induce flow of over-pressured fluids from the hydrothermal aquifer. In summer 2011, approximately one year post injection, the ball valve on 1362B was opened to draw tracer fluid back toward the borehole and discharge it into the overlying ocean. Approximately 4 L/s flowed from this borehole until summer 2013, when the 1362B borehole was closed (Neira et al., 2016) and the 1362A borehole opened, discharging water presumably at a similar rate. In addition, borehole 1301A is not properly sealed. Bottom water flowed into this borehole from 2004-07, at which point it spontaneous reversed, discharging at approximately 5 L/s (Neira et al., 2016). These operations are summarized in Table 4.1.

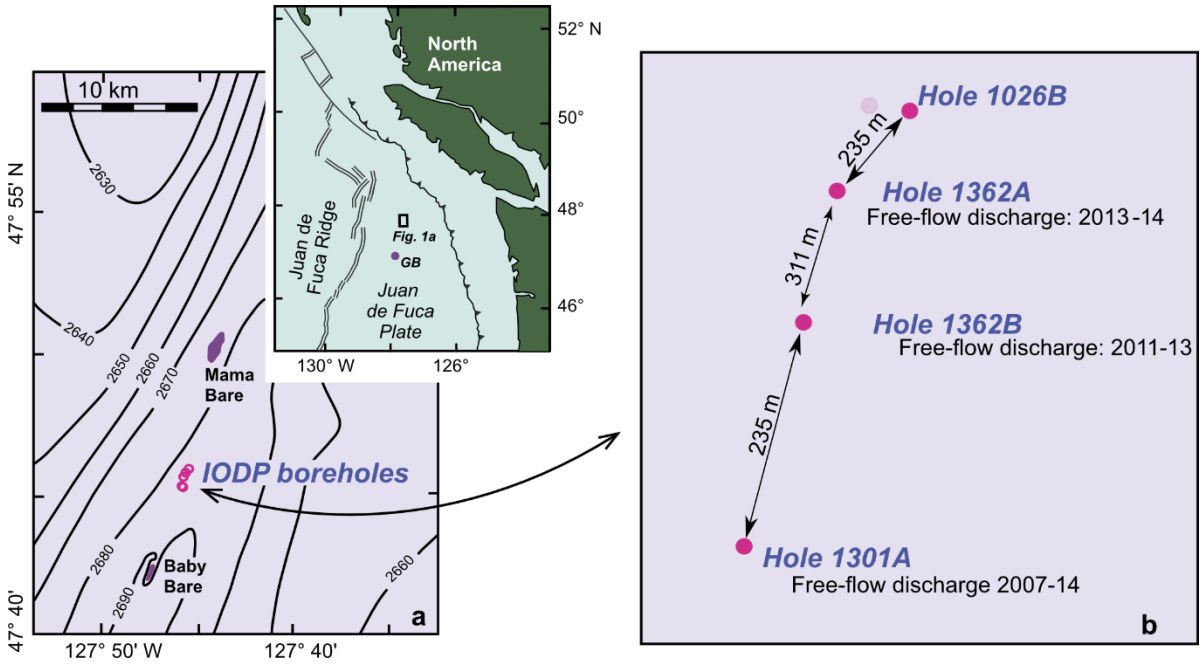

Figure 4.1 – Site maps at various scales modified from Neira et al. (2016). (a) Map of region surrounding experimental boreholes (Expedition 301 Scientists, 2005; Expedition 327 Scientists, 2011a; Shipboard Scientific Party, 1997) on the eastern flank of the Juan de Fuca Ridge. Inset index map shows location of Grizzly Bare outcrop (purple dot, "GB"), a known site of hydrothermal recharge (Wheat et al., 2000; Fisher et al., 2003; Hutnak et al., 2006). (b) Detail map showing distances between boreholes and timing for key tracer test operations described in the main text.

Table 4.1 - Summary of borehole and CORK configurations and operations, arranged from south to north on 3.5 M.y. old seafloor, eastern flank of the Juan de Fuca Ridge. Adapted from Neira et. al (2016).

	Hole:	1301A	1301B	1362B	1362A	1026B
Sediment thickness [a]	m	262.2	265.2	242	236	247.1
Drilled/cored depth [b]	mbsf	369.7	582.8	359	528	295.2
	msb	107.5	317.6	117	292	48.1
Final depth [c]	msb	34	-	106	283	22.8
Borehole casing depth [d]	mbsf	277.1	351.2	272	308.5	248.5
	msb	14.9	86	30	72.5	1.4
Open volcanic crust [e]	m	19.1	-	76	210.5	21.4
CORK installed [f]	year	2004/2008	2004/2008	2010	2010	2004
	IODP Exp.	301/321T	301/321T	327	327	301
Volcanic crustal levels [g]		1	2	1	2	1
Rapid fluid flow [h]	down	2004-07	2004-08	-	-	-
	up	2007-14	-	2011-14	-	-
Tracer [i]		M	M	I/M	M	M
Seafloor OsmoSamplers [j]	years of record	2010-14	ND	2011-14	2011-14	2010-14
Downhole OsmoSamplers [k]	years of record	ND	ND	2011-14	ND	2010-14

[a] Sediment thickness above volcanic crust determined during drilling. Hole locations shown in Fig. 4.1.
[b] Maximum depth of drilling, mbsf = meters below seafloor, msb = meters sub-basement.
[c] Hole depth prior to CORK installation, often less that drilled depth because of hole collapse. Final depth was not confirmed in Hole 1301B prior to CORK installation.
[d] Casing is metal pipe installed to stabilize borehole, isolates hole from formation.
[e] Thickness of open crustal rock interval between end of casing and final hole depth.
[f] Year and IODP expedition when CORKs were installed. CORKs in Holes 1301A and 1301B were not sealed during initial deployment, but were cemented on a later expedition.
[g] Number of crustal intervals intended to be isolated and monitored using CORKs
[h] Cold water was pumped and flowed into all holes when they were drilled. Hole 1026B has wept formation fluid at a slow rate since installation in 2004. Holes 1301A and 1301B were not sealed when originally installed, and cold bottom water flowed rapidly into these holes for several years. The flow direction in Hole 1301A spontaneous

reversed to outflow of warm formation fluid between 2006 and 2007. Holes 1301A and 1301B were cemented in an attempt to stop flow in 2008. Hole 1301B was sealed but Hole 1301A continued to discharge fluid. Flow from Hole 1362B was initiated in 2011 as part of a cross-hole perturbation experiment, at a flow rate of 4±2 L/s (Neira et al., 2016).

[i] I = location of tracer injection, M = location of tracer monitoring (wellhead and/or downhole)

[j] Years of record recovered by seafloor OsmoSamplers. Seafloor systems were installed prior to tracer injection on Holes 1026B, 1301A, and 1301B, but were installed one year after injection for Holes 1362A and 1362B. Expedition delay in 2012 resulted in sample/data gap, with length of gap varying by hole (Fig. 4). ND: no data, no samples were recovered from Hole 1301B.

[k] Years of record recovered by downhole OsmoSamplers. Downhole systems were installed prior to tracer injection on Holes 1026B, 1301A, 1362A, and 1362B. ND: no data, sampler was not recovered from 1301A, sampler malfunctioned in 1362A, no sampler was installed in 1301B.

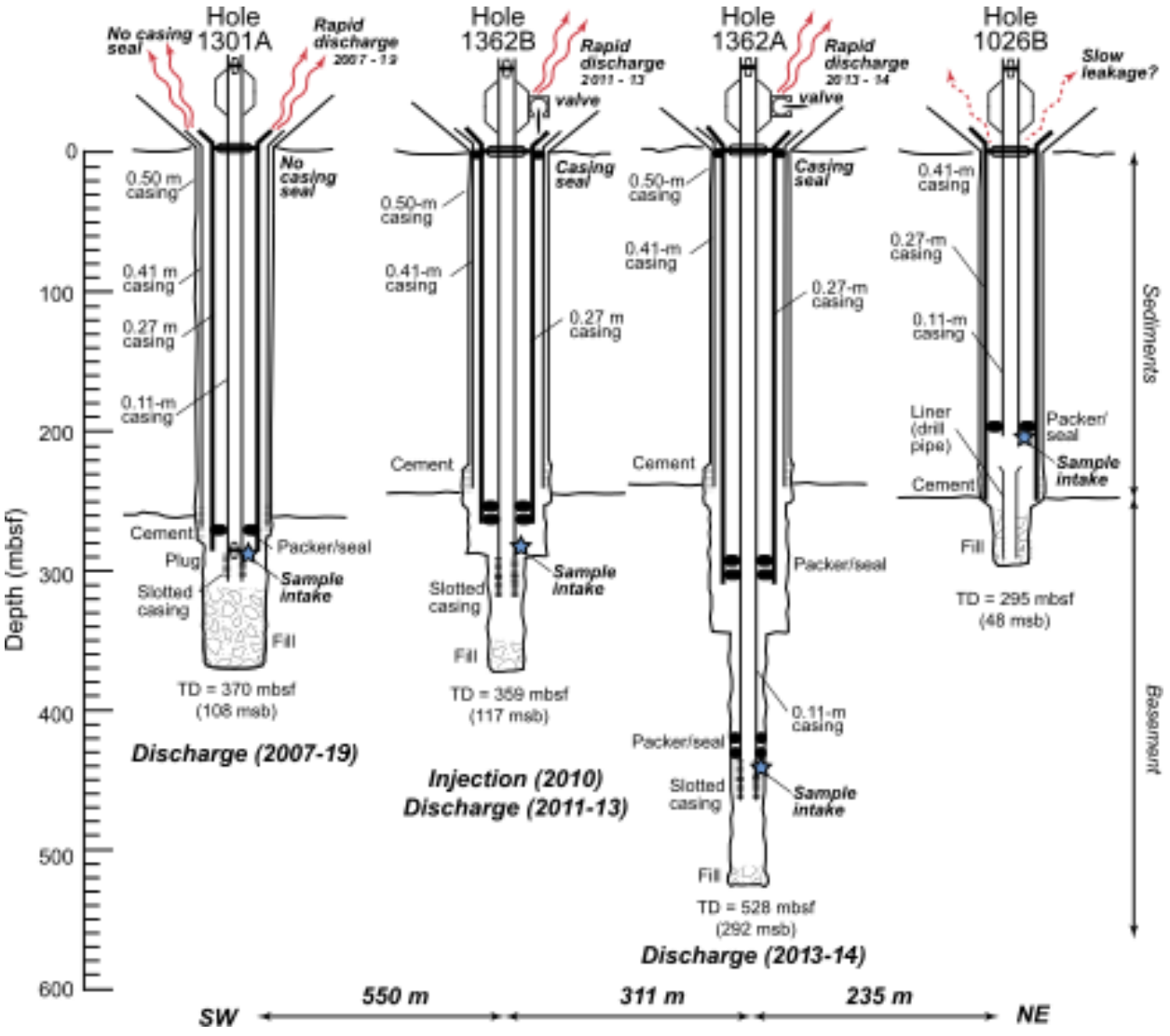

Figure 4.2 – Schematic diagram of CORKS and boreholes, vertically to scale (adapted from Neira et al. 2016).

Several observations and hypotheses guided interpretations of the multi-tracer experiment:

1. Ridge-Parallel Flow Direction

Several studies provide indirect evidence that ridge-parallel hydrothermal systems drive convective flow between basement protrusions. Geochemical analyses of porewater from transects show a compositional evolution from bottom water to formation fluid (Elderfield et al., 1999; Mottl and Wheat, 1994), and mathematical modeling demonstrates that convection cells can operate on a scale of tens of kilometers between basement outcrop recharge and discharge sites (Winslow et al., 2013, 2016). Specific to this study site, observations and heat flux measurements (Fisher et al., 2003; Hutnak et al., 2006, Wheat and Mottl, 2000; Davis et al. 1992; Mottl et al., 1998) in the vicinity of the Grizzly Bare, Mama Bare, and Baby Bare outcrops indicate bottom water recharge at the southern Grizzly Bare outcrops and heated discharge from the northern Mama and Baby Bare locations (Figure 4.3).

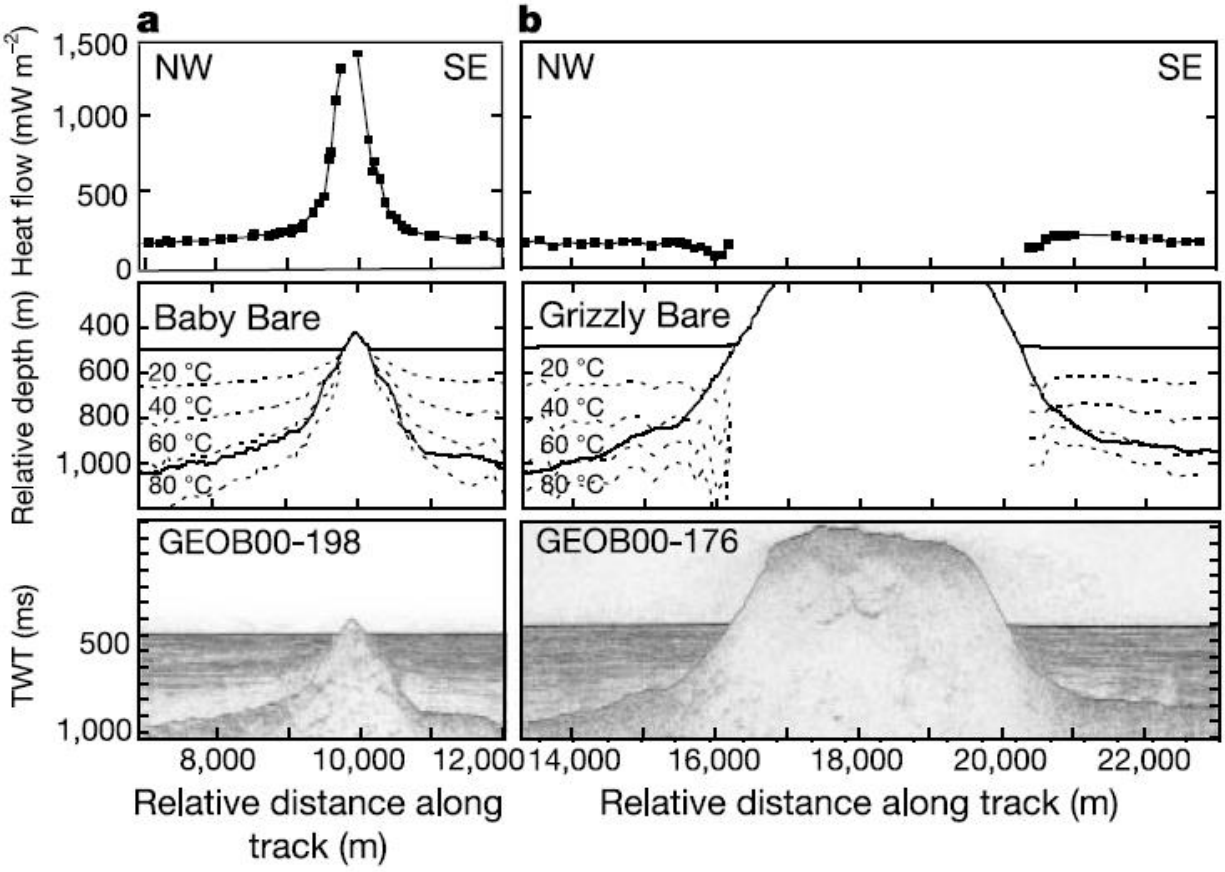

Figure 4.3 – Sediment heat flux transects demonstrating bottom water recharge at Grizzly Bare and hydrothermal discharge at Baby Bare (from: Fisher, 2003).

2. Aquifer Thickness of at least 200 meters

Spreading center geologic cross sections exposed on land as ophiolites display a predictable sequence: extrusive seafloor pillow basalts overlie sheeted dike complexes, beneath which is intrusive crystalline gabbro (Moores and Vine, 1971). Permeability is expected to decrease with depth as the formation becomes more massive and less fractured, but the depth at which low permeability effectively halts fluid flow is not well known (Fisher, 2005). Coupled 3-D modeling indicates that an aquifer thickness of 100-300 m is required to sustain convection in a system with the geometry of this project site (Winslow et al., 2013, 2016). Depths up to 600 m were

evaluated, but produced vigorous local convection and heat fluxes not consistent with observations.

3. Average linear velocity and borehole interconnectivity was unknown when the experiment was initiated.

On a $10^4 – 10^5$ m scale, geochemical transects and mathematical modeling supported linear average flow rates (V_L) on the order of 0.3 – 30 m/y (Fisher and Becker, 2000). Hutnak (2006) supported specific discharge of 10-20 m/y, indicating that linear velocities may approach 1 m/d if effective porosity is significantly less than bulk porosity. Even so, borehole interconnectivity adequate to facilitate cross-hole tracer arrivals was not assumed. The multi-tracer experiment results directly address these topics and tracer detections at all four boreholes provide invaluable data for estimating important aquifer properties.

4. Effective Porosity is much lower than Bulk Porosity

Physical analyses of drill cores indicate that pillow basalts contain approximately 10^{-1} (10%) bulk porosity (Bartetzko and Fisher, 2008), but the volume of pores sufficiently connected to conduct fluid is much less. Winslow et al. (2013; 2016) and other modeling efforts utilized 10^{-1} as the estimated effective porosity in fractured subseafloor basalt aquifer systems, but this estimate may be orders of magnitude larger than reality. Bulk porosity is a scale-dependent parameter, and this tracer study represents the first field-scale attempt to directly quantify it.

Analytical Methods

Samplers for Cs utilized Teflon tubing, and samples were prepared at the Monterey Bay Aquarium Research Institute (MBARI) and analyzed by inductively coupled plasma mass spectrometry (ICP-MS) at the University of California, Santa Cruz (UCSC). SF_6 requires gas-tight copper tubing, which was prepared and analyzed via gas chromatography at the University of California, Santa Barbara (UCSB).

The water-filled tubing is cut into lengths for analyses (typically one meter), and timing is determined by locating the interface between the DI water and formation water in the tubes and assuming a constant collection rate.

Summary of Neira et al. (2016) Results

Results obtained from the 2011 and 2013 sample retrievals were presented and interpreted by Neira et al. (2016). They built a conceptual model coupling 2010-2013 tracer results with modeling work by Hutnak et al. (2006) and Winslow et al. (2016), supported by physical observations from previous ODP/IODP cruises, such as borehole coring and packer testing. Lacking near-time data, Neira (2016) assumed that the injection fluid volume was accommodated near borehole 1362B and represented it as an instantaneous point-source patch. The model predicts that the natural gradient advected and dispersed the patch primarily in the northerly direction, following the buried ridge direction, and is supported by persistent tracer at boreholes 1362B and 1362A and tracer detection at 1026B. Unfortunately, a planned

2012 cruise to collect early-time samples was delayed, causing the loss of data that could have recorded the initial SF_6 breakthrough at the downgradient 1362A borehole. Interestingly, SF_6 tracer also was detected at southernmost borehole 1301A, contradicting the northerly flow hypothesis. This anomaly was explained by the presence of a preferential flowpath or localized convection cell that delivered a small amount of tracer some distance upgradient, which was then captured by the cone of depression formed by leakage from the 1301A well seal. Hutnak et al. (2006) and Winslow et al. (2016) concluded that "vigorous local convection" developed under the range of modeled parameters.

Neira et al. (2016) concluded that the average linear transport velocity was substantially faster than expected. The south to north flow direction hypotheses was supported by continued detection at downgradient borehole 1362A, and the V_L estimate of 2-3 m/day was derived from the travel time from 1362B to 1362A. A major conclusion was that effective porosity is orders of magnitude lower than the bulk porosity of basalt basement. Based on mass flux calculations from tracer discharge at 1301A, Neira et al. (2016) concluded that effect porosity ranged from 10^{-4} – 10^{-3}, orders of magnitude lower than the bulk porosity of 10^{-1} measured by Bartetzko and Fisher (2008).

New Results

The August 2014 and June 2019 sample collections provided additional SF_6 data, and, crucially, downgradient borehole 1362A tracer breakthrough of Cs. No other tracers were detected, likely due to their non-conservative nature and low signal-to-noise ratio in formation

fluid. Microbead tracers were also not detected beyond the injection hole, but the additional SF_6 and Cs data more strongly support some of the original hypotheses and suggest a re-evaluation of the conceptual model used in Neira et al. (2016) is needed.

SF_6 Data

The additional SF_6 tracer data, including the downhole OsmoSamplers, build upon Neira et al. (2016) conclusions regarding flow direction at the project site. Continued tracer persistence at 1362A and 1362B, coupled with no additional detections at 1301A support a south to north flow direction. Persistent attenuating signal at 1362A and 1362B continued for the duration of the experiment, through summer 2019. Additionally, two SF_6 breakthroughs were observed at farther downgradient (north) borehole 1026B at approximately 350 and 1343 days post injection (dpi) also supporting the flow direction hypothesis (Figure 4.4).

Cs Tracer Data

The most crucial data obtained since the publication of Neira et al. (2016) are the addition of Cs tracer data. Formation water at this location has a background concentration of approximately 8 nmol/L and Cs is not a completely conservative tracer (Saiers & Hornberger, 1996), so results derived from it serve as minimum estimates for parameters such as linear velocity. Comparing relative [Cs] with known conservative tracer [SF_6] provides some insight into aquifer properties and underscores that hydrothermal fluid linear velocity (V_L) and mass transport estimations derived from Cs data are likely underestimates. Despite this limitation,

the Cs tracer additions were adequate to produce a clear signal at borehole 1362A, 311 m downgradient from the injection site.

At the injection borehole 1362B, the Cs concentration initially declined as the natural gradient transported the tracer away, but concentrations remain approximately an order of magnitude higher than background for the duration. This illustrates the non-conservative nature of Cs, contrasting with the SF_6 results, which show similar concentrations at both 1362A and 1362B. An abrupt increase in [Cs] occurred between 310 and 321 dpi in Hole 1362B, followed by a gradual decline. This confirms that opening the ball valve on 1362B at 315 dpi induced significant changes in the injection hole, drawing Cs-rich fluid from around the borehole.

Despite the early SF_6 detection at 1301A, no Cs was detected at that 550 m upgradient borehole, though this can be explained by the non-conservatism and low signal-to-noise ratio achieved by the Cs tracer injection. The same reasoning can be applied to the 532 m downgradient borehole 1026B.

At 311 m downgradient borehole 1362A, however, Cs was initially detected below background levels, likely a remnant of surface water introduced during CORK installation days prior to the tracer injection. Cs was then detected above background at 9 dpi. An intermediate peak occurred at 24 dpi and a higher peak concentration occurred at 290 dpi, after which the concentration slowly returned to background levels during the remainder of the experiment (Figure 4.4e, 4.5).

The near-immediate Cs detection at 1362A exceeds linear velocity estimates from Neira et al. (2016) and from SF_6 breakthrough data at 1026B. Calculated independently, the 350 dpi peak at 531 m downgradient borehole 1026B yields a V_L of 1.5 m/d, consistent with the estimate of Neira et al. (2016). But the same logic applied to the 24 dpi Cs arrival 311 m downgradient at 1362A indicates a flow rate an order of magnitude greater. Either the heterogeneous fracturing at the site is such that the tracer patch advected 311 m in <24 days (V_L = 13 m/d) and then slowed, advecting the remaining 220 m in 326 days (V_L = 0.7 m/d), or the simple point-source model is invalid.

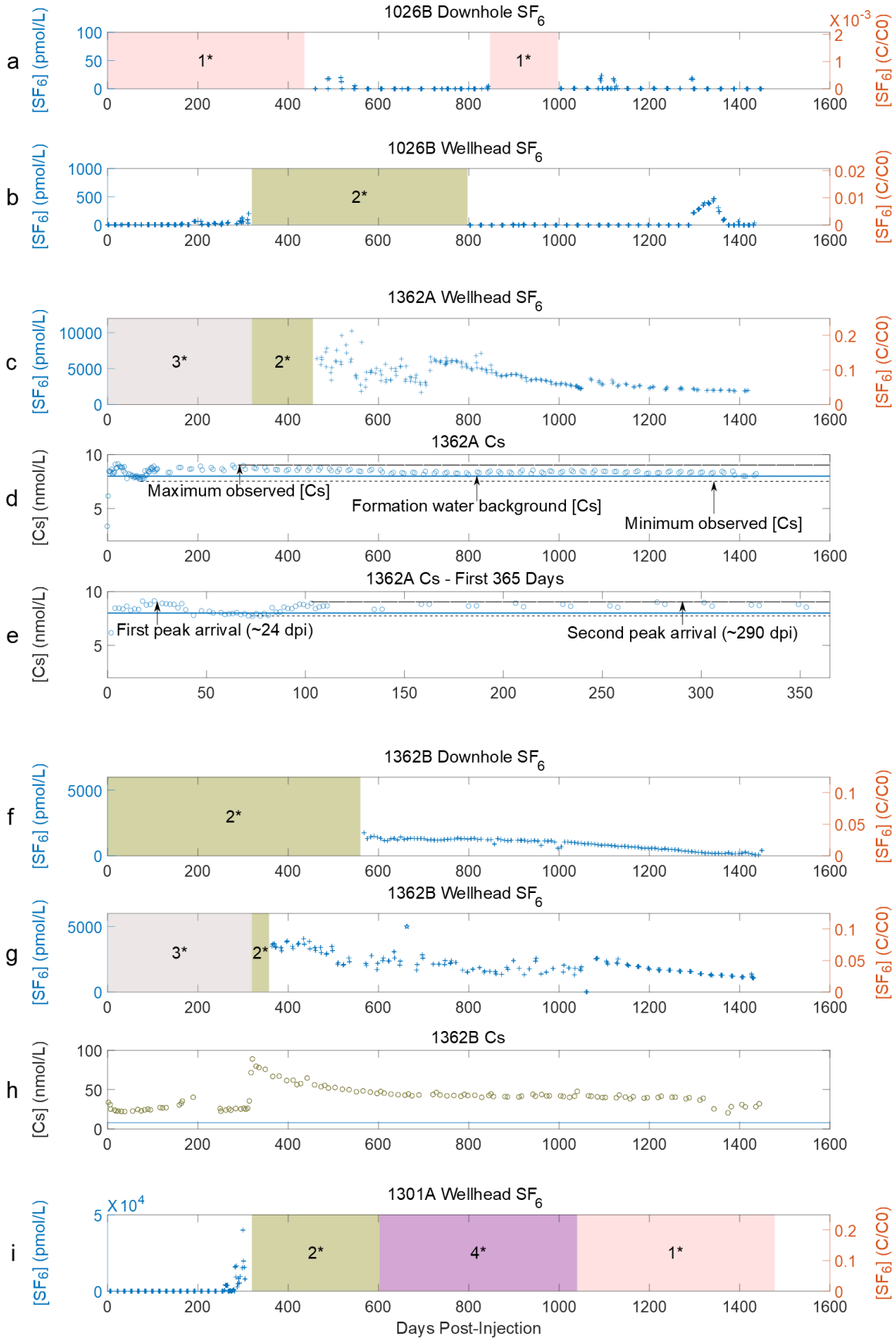
a
1026B Downhole SF6
[SF6] (pmol/L)
[SF6] (C/C0)
X 10-3
1*
1*
b
1026B Wellhead SF6
2*
c
1362A Wellhead SF6
3*
2*
d
1362A Cs
[Cs] (nmol/L)
Maximum observed [Cs]
Formation water background [Cs]
Minimum observed [Cs]
e
1362A Cs - First 365 Days
First peak arrival (~24 dpi)
Second peak arrival (~290 dpi)
f
1362B Downhole SF6
2*
g
1362B Wellhead SF6
3*
2*
h
1362B Cs
i
1301A Wellhead SF6
X 10^4
2*
4*
1*
Days Post-Injection

Figure 4.4 (previous page) – Compilation of all tracer results up to August 2014. For times indicated with: 1* (pink) - All samples below detection limit; 2* (green) - Samples lost due to overpumping of Osmosampler; 3* (gray) - No sampler deployed; 4* (purple) - Sporadic detections <25 pmol/L. See Appendix 4.1 for enlarged and rotated data through June 2019.

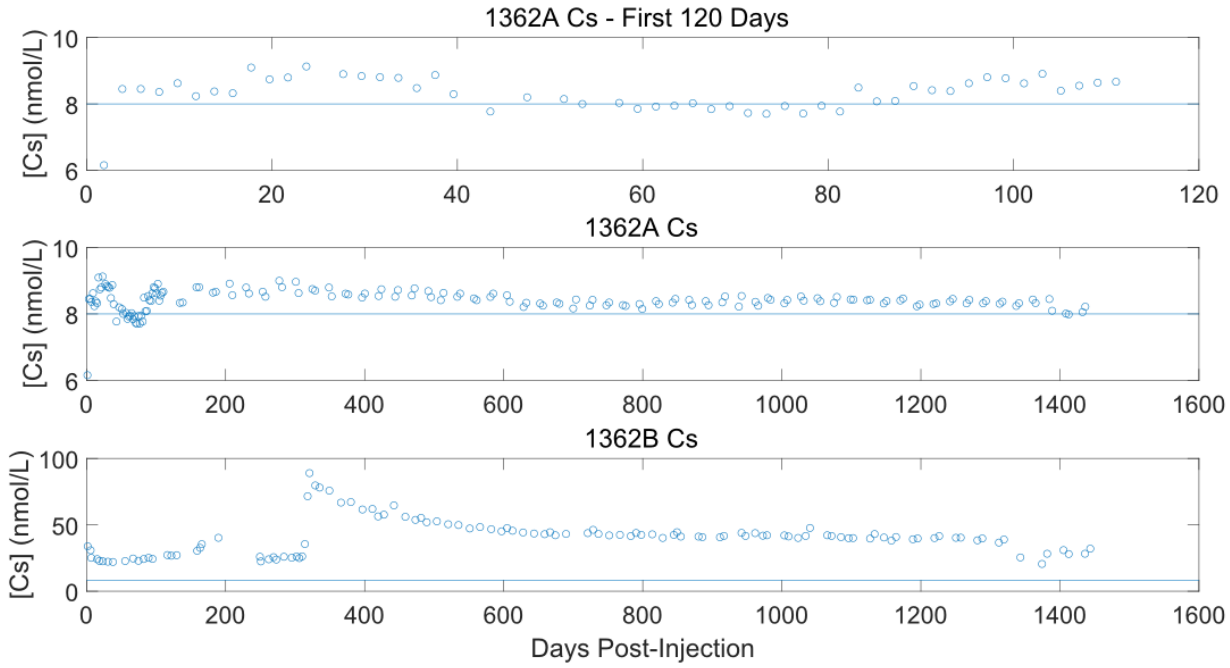

Figure 4.5 – Compilation of Cs tracer results, rescaled. Rescaled y-axes emphasize detections below natural background concentration (thin line, ~8 nmol/L) 40-80 dpi in 1362A.

Discussion

A Revised Site Model

To reconcile the unexpected results from the additional data two hypotheses are proposed:

1. Effective porosity is sufficiently low to invalidate terrestrial point source model assumptions used in previous interpretations.

The original interpretations were based on limited data and modeled after terrestrial aquifer studies, where high effective porosity allows the injection event to be approximated as a point source located at the borehole, although a careful inspection of the Borden Aquifer Natural Gradient Experiments reveals that on Day 1, the tracer patch was significantly larger than the injection wells volume (see figure 8a in Mackay et al., 1986). But if an injection were to take place in an aquifer with dramatically lower effective porosity, the injection should displace fluid a considerable distance from the injection hole. Winslow et al. (2013; 2016) modeling efforts assumed effective porosity to be between 10^{-2} and 10^{-1}, so any major revision of this parameter has implication for interpreting their model results and any future modeling efforts.

2. The low effective porosity explains some effects from leaking boreholes and ball-valve operations meant to induce "pumping" conditions.

In confined aquifers, the capture zone of "pumping" wells is inversely related to its storage coefficient, a major component of which is porosity (Heath, 1983). If the effective porosity is extremely low, leaking boreholes and ball valve operations meant to induce pumping effects similar to terrestrial "push-pull" tests would induce larger than anticipated capture zones. Upgradient borehole 1301A is one of the "leaking" boreholes, so injection fluid displacement towards this hole overlapping with a large capture zone might explain why there was a brief "upgradient" SF_6 breakthrough.

Several assumptions are required. While some missing data could build a stronger case, the revised simple model is internally consistent.

Assumptions:

1. Boreholes 1362B and 1362A are aligned approximately in the direction of flow.

Boreholes are aligned along a buried basement ridge, parallel to the spreading center ridge and vector between the hypothesized recharge and discharge seamounts, but the lack of sampling from an off-axis borehole normal to the injection borehole makes it impossible to say with certainty that the boreholes are not at some angle to the primary gradient direction. A small angular misalignment would have little effect at close distances, but the two most distant boreholes are each over 500 m from the injection hole, so a misalignment could result in detections representing the edges of the main tracer patch transiting a borehole rather than the main body of the patch (Figure 4.6).

2. Injection fluid displacement of formation water occurs in both the downgradient and upgradient directions, with a force sufficient to displace fluid approximately the same distance in both directions.

If the injection displaced fluid most of the 311 m distance between injection borehole 1362B and downgradient borehole 1362A, and the natural gradient is not sufficiently strong, a similar displacement should occur in the upgradient direction, toward borehole 1301A.

3. Aquifer properties are sufficiently homogenous at the scale of this experiment.

On a hand-sample scale, fractures in basalt are highly heterogeneous. But on a larger scale such as the $10^2 – 10^3$ m scale in this study, the geologic processes controlling fracture density and alignment should be such that a homogenous bulk model is valid (Fisher, 1998).

This paper attempts to describe a representative elemental volume (Bear, 1984) on a scale of 10^2-10^3 meters, constrained by cross-hole tracer results, for use in future modeling efforts.

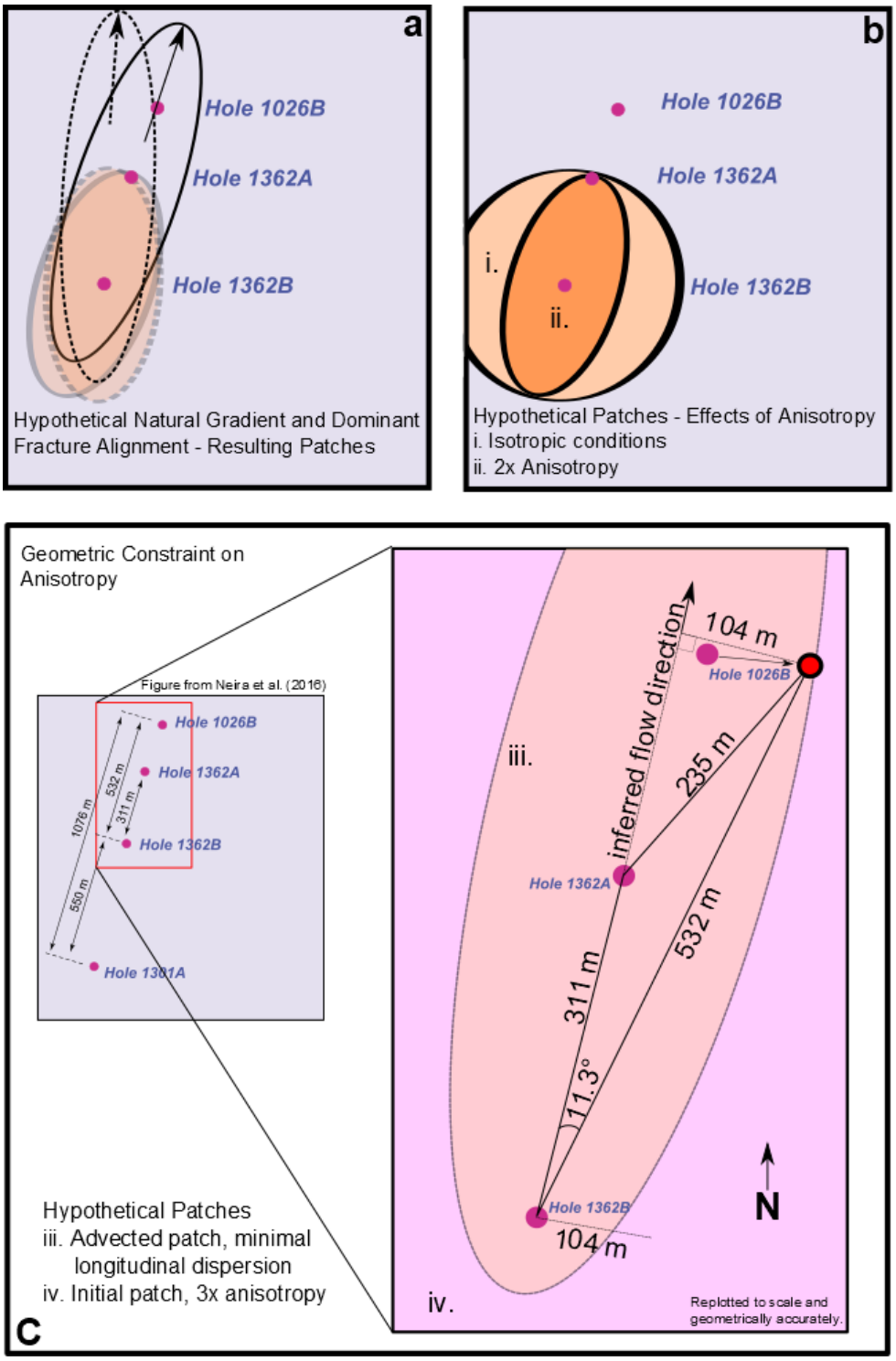

Figure 4.6 – Effects of a) borehole misalignment and b) anisotropy on tracer injection fluid displacement extent and advection. c) Geometric limit on anisotropy, with 1026B accurately plotted.

The Dual Cs Breakthrough

At borehole 1362A, Cs was initially found to be below background levels. This can be explained by either the rapid arrival of freshwater that was injected between hours 1 and 2 during the 24 hour fluid injection or by the introduction of seawater during drilling. Cs tracer, which was injected beginning at hour 3, was detected in 1362A above background levels after 9 dpi, but enhanced resolution sampling indicates two arrivals: an initial peak at 24 dpi, and a secondary peak at 104 dpi. These breakthroughs are followed by persistent Cs concentrations above background until 500 dpi. Between these two peaks, Cs concentrations dropped below formation background values (i.e., 40 – 80 dpi), indicating a lower [Cs] water such as the surface ocean seawater of which the injectate was composed (Figure 4.5).

The Cs injection was not continuous over the 24 hr injection period. Solid Cs salts were mixed with surface seawater injectate during two short intervals: for 7 minutes at 3 hours into the injection, and for 8 minutes at 19 hours into the injection. It was anticipated that mixing in vicinity of the borehole would homogenize the Cs tracer into a single pulse (Fisher et al., 2011), but a simple analysis of the borehole construction geometry and fluid injection rate questions this assumption. The volume of the unsealed portion of the 359 m deep borehole totals ~21 m^3, while ~570 m^3 of fluid were injected, a volume approximately 27 times larger.

In a terrestrial aquifer with 10-30% porosity, such a volume would easily be accommodated within a few meter radius of the injection hole, validating the point-source approximation. Injection borehole 1362B extends 117 m into the basement, contains ~21 m^3 volume, and constitutes a vertical line source for injection fluid. In a hypothetical homogenous

isotropic aquifer with an effective porosity of 10%, injected tracer spreads predominantly laterally, displacing formation fluid in an approximately cylindrical distribution, causing displacement to a radial distance of less than 4 m from the borehole. In fractured seafloor basalt the high end of previous estimates of effective porosity is only 0.1%. In this environment, the injection would create a cylinder with a 100 times greater radius.

The Simple Elliptic Cylinder Model

In a homogeneous, isotropic aquifer, injection fluid displacement can be simply modeled as a cylinder centered on the injection borehole. For a fixed volume of injection fluid, the extent of the cylinder is controlled by its height (in this case the aquifer thickness), radius (displacement distance), and the effective porosity of the cylinder material. Anisotropy is likely in subseafloor hydrothermal systems with fault-parallel fracturing, so a slightly more complex elliptic cylinder model seems more appropriate, with anisotropy represented by ratio of the long to short axis of the ellipse. More complex geometry is likely due to heterogeneous fracturing and stratified hydrogeologic properties, but we lack 3-D and discrete depth sampling needed to justify a more unique model.

Borehole geometry dictates that the cylinder is at least 200 m deep. The open portion of borehole 1362A begins approximately 200 m into the basement rock, so tracer had to have penetrated at least that deep into the formation. This deduction is supported by modeling data requiring 100 - 600 m of aquifer thickness to sustain hydrothermal circulation (Winslow et al.,

2016), and borehole packer experiments and thermal logs indicating permeability to at least 320 m (Becker, et al.2013; Fisher and Becker, 2000; Winslow et al., 2013).

The range of previous effective porosity estimates is approximately 0.1% - 0.01% (Neira 2016). Anisotropy estimates vary over orders of magnitude ($10^0 – 10^3$), so it is useful to constrain the remaining variable: long axis radius.

Using this model, the dual Cs arrivals at 1362A are explained by their short tracer injection durations separated by 16 hours of surface ocean water fluid injection with no added Cs. This sets up a simple one-dimensional system of algebraic expressions to solve for the displacement distance and nature gradient velocity, with three equations and two unknowns (Table 4.2).

The center of mass Cs arrival times are picked as they represent the mean linear velocity. The ratio of the distance each plume was displaced is also known, defined by the ratio of the respective fluid injection times after each Cs injection. The first injection occurred three hours into the 24-hour injection, and thus was displaced for 21 hours, and the second Cs injection occurred at 19 hour and was displaced for 5 hour until the end of the fluid injection.

Table 4.2: Variables, definitions, and values used to derive mean linear transport velocities from breakthrough curves.

Variables	Definition	Value
T_1	First Cs arrival center of mass (days)	24 dpi
T_2	Second Cs arrival center of mass (days)	290 dpi
D_0	Distance between boreholes 1362B and 1362 A (m)	311 m
D_1	Injection displacement distance of first Cs arrival (m)	Calculated
D_2	Injection displacement distance of second Cs arrival (m)	Calculated
V_L	Mean linear groundwater velocity (m/d)	Calculated
t_1	Displacement time for first Cs injection (hr)	21 hr
t_s	Displacement time for first Cs injection (hr)	5 hr

System of equations:

$$T_1 = \frac{D_0 - D_1}{V_L} \tag{4.1}$$

$$T_2 = \frac{D_0 - D_2}{V_L} \tag{4.2}$$

Mean arrival time is the remaining distance divided by the velocity and the displacement distances are not known, but the ratio of the two is known from the ratio of injection times following each Cs injection. Therefore, solutions for V_L, D_1, and D_2:

$$V_L = \frac{D_0 - D_O * \left(\frac{t_1}{t_2}\right)}{T_2 - T_1 * \left(\frac{t_1}{t_2}\right)} \tag{4.3}$$

$$D_1 = D_0 - V_L * T_1 \tag{4.4}$$

$$D_2 = D_0 - V_L * T_2 \quad (4.5)$$

This simple math indicates that the first Cs injection was displaced 291 m towards 1362A, the second injection 69 m, and both were then advected at 0.83 m/d (Figure 4.6). The temporal and spatial gap between the two Cs pulses would have been filled with injection fluid composed of surface ocean water that contains four times less Cs than formation water (Elderfield et al., 1999; Wheat and Mottl, 2000); this "negative concentration tracer" patch is recorded as the Cs concentration dips below formation water composition in the interval between Cs breakthroughs at 1362A, and is apparent between approximately 40 dpi and 80 dpi (Figure 4.5). At borehole 1362B, prior to a perturbation caused by opening a ball valve at 313 dpi, [Cs] was initially ~40 nmol/L and then decreased in concentration before peaking once more at approximately 200 dpi. This is consistent with the new model: the Cs displaced upgradient of the borehole by injected seawater was then advected back toward it.

These results can be applied to the initial SF_6 arrival at 1026B, 532 m downgradient from the injection borehole. The rapid Cs breakthrough at 1362A and later SF_6 arrival at 1026B are primary reasons a new hypothesis was proposed. The same algebra used for Cs dual-breakthrough is applied here. The SF_6 injection began shortly after (20 minutes) the onset of the fluid injection, thus was displaced farther than either Cs patches (328 m). This yields V_L of 0.58 m/d for the remaining distance to 1026B. The short duration of the 1026B breakthrough and the difference between this value and the 0.83 m/d calculated from the Cs dual-pulse suggests that the boreholes are not aligned precisely in the primary gradient direction and 1026B samplers recorded a lateral edge of the main tracer patch (Figures 4.6a, 4.6c). Even so,

these values are within a reasonable range, much less than the order of magnitude difference using the point-source analog.

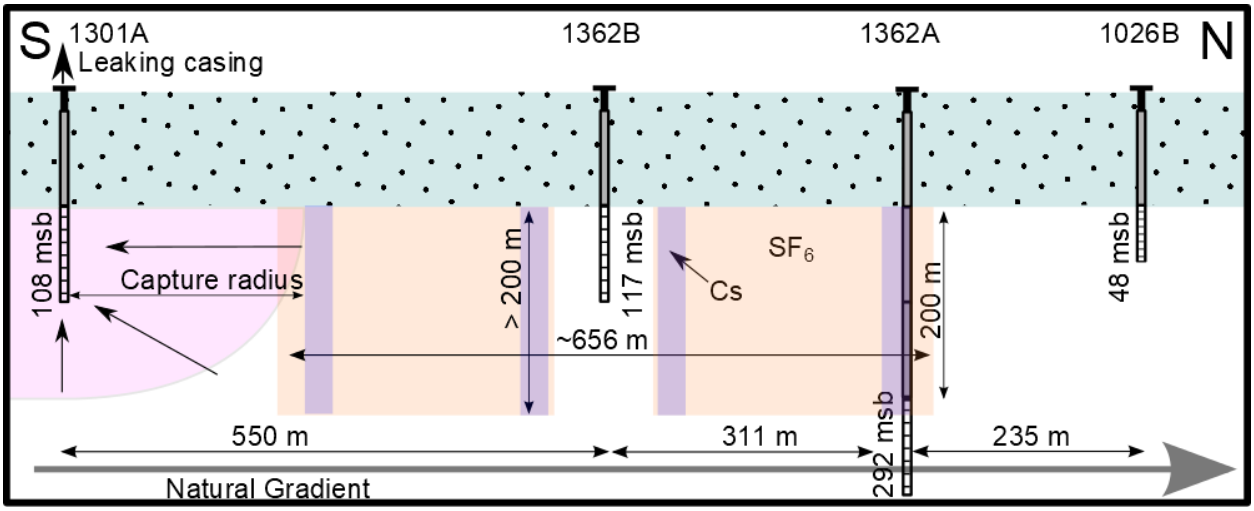

Figure 4.7 – Simplified to-scale cartoon of tracer distribution immediately after 24 hour fluid injection. To scale. "msb" = meters sub-basement. Solid casing at 1362A extends to 210.5 msb with a packer seal between the casing and formation at 200 msb. The borehole is open to formation to 292 msb.

Revised Effective Porosity and Anisotropy Estimates

Expanding the one-dimensional model into three dimensions, we use the injectate plume extent as the long axis of an elliptic cylinder.

One unconstrained variable is the short axis of the ellipse. Obviously, varying the cylinder geometry changes its volume. Tracer was continuously present at 1362A and only sporadically detected at 1026B, so we posit that the dispersed lateral fringe of the patch was advected past 1026b. Neira et al. (2016) presented the boreholes in an approximate straight line; here we plot them with geometric accuracy to illustrate the feasibility of this scenario. This limits the lateral anisotropy to approximately 3x (Figures 4.2 and 4.6c; Table 4.1). Smaller

anisotropy would result in a more constant tracer presence, and anisotropy significantly greater would result in the patch missing the borehole entirely. The extent of dispersion from the original patch emplacement dimensions is unknown, so there is uncertainty in this value. A monitoring borehole located normal to the flow direction and 10's of meters east or west of 1362B would have greatly aided in determining this value.

The remaining unconstrained variable in our simple model is the effective depth of the cylinder. Permeability must extend at least 200 m, as tracer was detected in borehole 1362A, which was cased to that depth in the upper ocean crust aquifer (Figure 4.7). Within a cylinder of that depth, fluid may be more concentrated in tabular strata of higher porosity and permeability, but these results are intended to provide estimates of bulk aquifer properties on the $10^2 – 10^3$ m scale of this experiment.

The volume of the cylinder is not fully composed of injection fluid, rather it represents the space where connected porosity is intruded by the injection event. This allows exploration of the relationship between the depth of permeability, lateral anisotropy, and effective porosity (n_e).

Greater anisotropy, represented by a greater ratio between the fixed long-axis and unconstrained short axis, decreases the volume of the cylinder. As the fluid volume is known and constant, decreasing the cylinder volume correlates with increased effective porosity in order to accommodate the fluid. Varying the cylinder depth is similarly conversely related to effective porosity.

Table 4.3: Variables, definitions, and values for the elliptical cylinder model.

Variables	Definition	Value
C	Elliptic cylinder volume (m^3)	Unconstrained
V	Injectate volume minus borehole volume (569 - 21 m^3)	548 m^3
n_e	Effective porosity range	10^{-2} - 10^{-5}
D_1	Long axis length or displacement distance (m)	328 m
A	Lateral anisotropy	10^0 – 10^1
H	Depth (m)	> 200 m

Using geometric constraints, the simplified elliptical model, the long axis length (328 m) and a range for the other parameters (Table 4.3) relationships between variable parameters can be estimated (Figure 4.8). The application of our tracer data can be used to support and refine conclusions from theoretical models developed by Winslow et al. (2013; 2016). A major limitation is the neglect of vertical anisotropy and the assumption of vertically homogenous porosity. While these assumptions may be close approximations in the upper tens to hundreds of meters of pillow basalts, increased pressure and secondary mineral deposition do decrease porosity and permeability with increasing depth (Fisher, 2005).

Anisotropy is commonly discussed in virtually all research involving permeability in fractured basalt hydrothermal systems (Becker, 2000; Fisher et al., 1997; Fisher, 1998; Winslow et al., 2013; 2016), but field-scale measurements to define the range of possible values were lacking, so these discussions are mostly limited to qualitative speculation, i.e. “enormous permeability anisotropy” (Fisher, 1998). Modeling efforts either arbitrarily limit anisotropy to values such as 10^2 (Rosenberg and Spera, 1990; Rosenberg et al., 1993), or omit anisotropy

entirely (Winslow et al., 2016). Neira at al. (2016) also neglected anisotropy in calculating effective porosity at this site with mass-based methods.

The simple tracer and borehole geometry-derived model supports a lateral permeability anisotropy factor of 10^0 – 10^1. In agreement with Neira et al. (2016), these results suggest effective porosity is multiple orders of magnitude less than bulk porosity values obtained from drill cores, ranging from 10^{-4} to perhaps as low as 10^{-5}. These calculations assume complete saturation of connected porosity during the injection event, but observed 1362A [SF_6] suggest that back-projected C/C_0 immediately following the injection may have been nearer 0.5, indicating that injectate was mixed with formation fluid rather than completely displacing it via piston flow. Applied to our idealized results, this increases the effective porosity by up to one order of magnitude (Figure 4.8). Even so, a n_e of 10^{-3} is at least an order of magnitude smaller than bulk porosities observed in drill core samples.

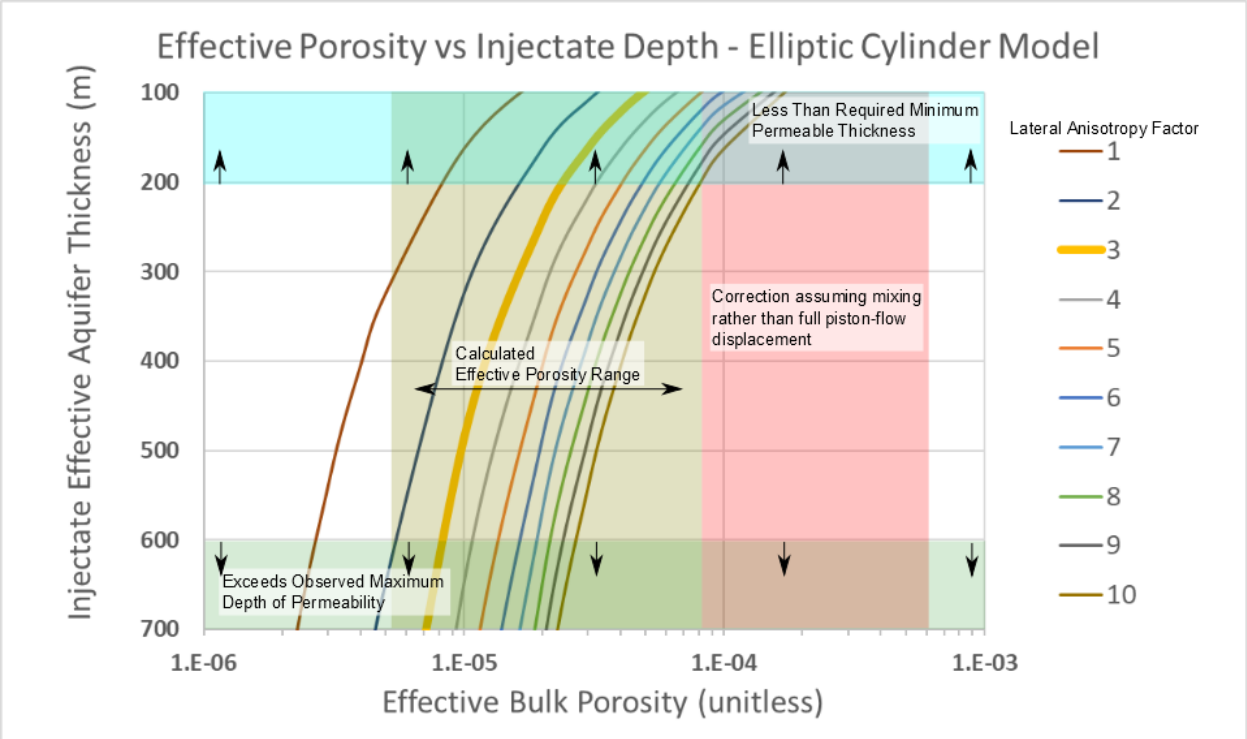

Figure 4.8 – The relationship between lateral anisotropy, effective porosity, and aquifer thickness in our simple three-dimensional model.

1301A Upgradient Arrival

The early 1301A SF_6 arrival seems to contradict the hypothesized flow direction, but the limited 1301A detection coupled with the persistent tracer detections at the inferred downgradient boreholes 1362B, 1362A, and 1026B do indicate that flow is from south to north.

In our revised model, SF_6 tracer was displaced approximately 330 m both up- and downgradient from the borehole during the 24 hr injection period. This constitutes over half the distance between the injection hole and 1301A, but something must then have induced it to advect the remaining 222 m. As it turns out, despite repeated efforts to cement the rentry cone in 2006, 2007, and 2009 (Fisher et al., 2011), borehole 1301A leaks. Initially, cold bottom water flowed into the unsealed borehole after drilling in 2005, but this flow spontaneously reversedat some point between 2006 and 2007, and leaked at an estimated rate of 5 ± 2 L/s (Neira et al., 2016) for the duration of this experiment. These leaks are the result of spontaneous flow from the overpressured hydrothermal aquifer confined beneath fine grained sediment, and induce "pumping" conditions at this borehole.

A pumping well in a confined aquifer develops a large cone of influence; in the presence of a natural gradient a capture zone extends downgradient to a stagnation point, where the natural and induced gradients are equal and opposite. Higher anisotropy and lower conductivity, permeability, and/or effective porosity results in the well capturing fluid a larger distance downgradient. As indicated by previous theoretical models and our simple tracer-

based model, effective porosity of shallow ocean crust may be much less than 10^{-2} and lateral anisotropy may be up to 10^{1} or greater, so it is conceivable that the leaking 1301A casing induced a capture zone that overlaps with the fluid displaced upgradient from injection hole 1362B (Figure 4.7).

Cs data from 1362B shows the large effect of such discharge. As part of planned operations, a ball valve was opened during the 2011 site visit in order to induce pumping conditions in the hopes of conducting a "push-pull" single borehole experiment. This disturbance occurred approximately 313 dpi, and is evident from the increase in [Cs] (Figures 4.4h, 4.5), as Cs was pulled back to the hole within ten days. Such an effect may be ongoing at 1301A, and the cone of depression that developed over the three years from 2007 – 2010 may encompass a large area.

Summary

Additional SF_6 and Cs tracer data have helped fill in and extend the initial data presented by Neira et al. (2016). The rapid Cs tracer detection at borehole 1362A triggered a reevaluation of the basic conceptual model used to interpret tracer breakthrough curves. The primary finding is a rejection of the point-source model for calculating flow velocities and constraining aquifer properties. Previous estimates of extremely low effective porosity by Neira et al. (2016) are supported; it is likely that effective porosity is as much as five orders of magnitude lower than drill core-scale bulk porosity in seafloor basalt, which has significant implication for numerically modeling basement hydrothermal convection systems. Lateral anisotropy is likely

in fault-guided fractured rock aquifers, with a factor ranging from 10^0 – 10^1. Tracer results are consistent with the depth of permeability constraints developed in Winslow et al. (2016), indicating that permeability likely does not extend below approximately 300 m subbasement. Both the south to north ridge-parallel flow direction and the hydrothermal convection cell theory is supported at this site on the Flank of the Juan de Fuca Ridge. Further study involving a field of non-linear boreholes will be indispensable to enhancing understanding of subseafloor hydrothermal aquifer anisotropy.

Current ocean crustal fluid flow modeling literature has utilized the bulk porosity of basalt (10^{-1}) under isotropic conditions. These results indicate that future modeling efforts should broaden possible aquifer property ranges to include effective porosities as low at 10^{-5} and lateral ridge-parallel anisotropy as high as 10^1. The field scale of this tracer experiment supports these properties on a 10^2 – 10^3 m REV scale.

Implications for Geochemical Tracer Interpretations

These results also complicate the use of intrinsic tracers to determine hydrothermal fluid age, as decreased effective porosity limits the substrate available for geochemical exchanges. The fractured aquifer nature of the oceanic crust aquifer increases the chances of dead end pores and stagnant water effecting these results (Fisher, 2004). Fluid traveling between two points may interact with older reservoirs of stagnant porewater, exchanging components and imparting an older apparent age to the active hydrothermal fluid flow. Correcting for this interaction requires inputting aquifer layer porosity and thickness, two values which are constrained in this study.

$$u = [(1 + F)\Delta x]/\Delta t_a \quad (4.6a)$$

$$F = (n_{con}h_{con})/(n_{aqf}h_{aqf}) \quad (4.6b)$$

Equation 4.6 – Correcting apparent tracer ages or fluid velocities due to interaction with stagnant porewater from Fisher (2004), where n = porosity, h = layer thickness, subscripts aqf and con refer to the aquifer and confining layers, respectively. Δx is the lateral spacing between two sample locations; and Δt_a is the apparent age difference between fluids at each location.

Decreasing aquifer thickness or porosity increases this correction factor, which has been estimated to be 10-50, based on thicknesses of 10-500 m and porosities of 1-5%. Preliminary results from this study suggest that the effective aquifer thickness is on the short end of that range, and Fisher (1998) points out that even the lowest porosity values may also be erroneously high due to most flow occurring in limited connected porosity, lowering the effective porosity.

In order to utilize geochemical tracer results to obtain actual ages and flow velocities of hydrothermal fluid, the various correction factors detailed above rely on assumed ranges of aquifer properties to account for complications due to stagnation and geochemical exchange. Enhanced aquifer property estimates from this deliberate tracer study provide more accurate values for these properties, and could improve velocity estimates from intrinsic tracers. Ideally, a more comprehensive understanding of the hydrothermal model will rectify discrepancies between methods, such as the 3-4 order of magnitude difference between SF_6 tracer velocities and those derived from other tracers. Improving the carbon budget constraints using data from

this study could have applications in radiocarbon, oxygen isotope, and other tracer studies in terrestrial fracture-flow potable aquifers.

Acknowledgements

We thank the skilled dedicated technicians, officers, crews, engineering, and operations staff of the *DR/V J. Resolution*, *R/V Atlantis*, submersible *Alvin*, and ROV *Jason*. This research was supported by NSF grants OCE-1031352 and OCE-1260353 (J.F.C.), OIA-0939564 and OCE-1260408 (A.T.F.), OCE 1260548 (C.G.W.), Consortium for Ocean Leadership Projects T327A7 and T327B7 (A.T.F.).

Chapter 5
Well Capture in an Anisotropic Aquifer

Introduction

Water withdrawn from a well is physically removed from the surrounding aquifer. In an unconfined terrestrial isotropic aquifer, the effect is intuitive: under continuous pumping, the water level declines in the well and for some radial distance from the well. Beyond that distance, the water level remains unchanged from static conditions. In a productive aquifer, continuous pumping eventually yields a pseudo-steady state, where the volume of water extracted is matched by the volume flowing towards the well, and the pumping water level stabilizes. No natural aquifer is truly infinite, but for extraction rates that are limited relative to the total storage, transmissivity, and recharge potential, steady state conditions are realized in practice.

Similar dynamics apply to wells screened in confined aquifer systems. Piezometric pressure replaces physical water levels, and the variables upon which the areal extent affected by pumping differ, but the concept remains the same.

That areal extent is known as the *radius of influence*. Within the radius of influence, pressure in the aquifer is decreased relative to static conditions, and the natural aquifer gradient is altered, sloping towards the well as extracted water volumes are replaced by water from the surrounding aquifer matrix. In two dimensions (length and depth), the piezometric

surface is commonly referred to as the *cone of depression*. Analytical solutions and three-dimensional models can be used to delineate a well's *capture zone*, which is the three-dimensional space from which extraction physically draws water.

In terrestrial hydrogeology, capture zone analysis is an important tool used in assessing systems and designing infrastructure to meet a variety of needs. In a simple case, adjacent wells may have overlapping capture zones that manifest as *interference* which increases drawdown and decreases the available yield from any single well in a wellfield relative to its independent capacity. Capture analysis is also crucial if nearby groundwater contaminants are a concern. If a well's radius of influence overlaps with a preexisting contaminant patch, plume, or source area, contaminants may be drawn to the well and negatively impact water quality. If remediation or filtration is not feasible, the pumping rate might be adjusted to exclude contaminants from a well's capture zone.

Alternately, some wells are designed specifically to capture and treat wells contaminants. These *pump-and-treat* systems might be engineered to intercept contaminants upgradient of a potable or irrigation supply well, or simply to remove anthropogenic contaminants for regulatory and environmental health purposes.

Confined or unconfined, terrestrial or otherwise, capture zone analysis relates the areal extent of influence of a well to two main groupings of variables: well design characteristics and the intrinsic aquifer properties.

In this chapter, capture zone analysis is applied to tracer results from the four subseafloor IODP boreholes utilized in this tracer study. These boreholes are analogous to

partially-penetrating wells in confined terrestrial aquifers in that they are (nominally) sealed at the surface, cased through the overlying fine-grained confining sediments, and open in the bedrock aquifer interval. Overpressure in the hydrothermal aquifer allowed for “pumping” via operation of ball valves at two wellheads, and leakage from an imperfect seal at a third also induced discharge conditions.

As is the case with much of this study, many poorly-constrained variables and data gaps exist, but there are sufficient data to describe, both conceptually and analytically, how well-capture driven by intentional and incidental discharge from various borehole explains observed tracer results and provides further internally-consistent support for the low porosity conceptual model described in Chapter 4.

Well Capture Theory

Well capture analysis seeks to delineate a pumping well’s capture zone either in steady state or transient conditions. Analytical solutions exist in the literature for many idealized scenarios. The ideal steady-state cone of depression forms in the simplest case: a well pumping for an infinite amount of time in an infinite, homogenous, isotropic, aquifer with no gradient. Of course, no such ideal aquifers exist in reality, but conditions can approach the ideal if an aquifer is sufficiently transmissive relative to the pumping rate, and pumping does not proceed for long enough that the radius of influence encounters any boundary conditions, such as faults, geologic discontinuities, and are other impermeable material. No real-world scenario is ideal, but by understanding the effects of non-ideal parameters such as spatial heterogeneities and anisotropy, the idealized solutions can be applied as limiting cases for complex systems. Three-

dimension modeling can also determine flow paths and capture zones, but a model is only as good as the input parameters used to form it, and thus rely on the same assumptions and limitations for systems with a high degree of parameter uncertainty.

In a homogenous, isotropic aquifer, a pumping well will develop a circular capture zone in plan view, taking a conical form in three dimensions, leading to the term *cone of depression*. Under idealized conditions within a hypothetical infinite aquifer, pure analytical solutions do not exist, as, in actuality (and mathematically), the radius of influence grows infinitely with time, only reaching a steady state asymptotically. Several semi-empirical and empirical solutions exist (Table 5.1) to approximate the distance at which drawdown is "negligible" (Bear, 2007).

Table 5.1: Radius of Influence Approximations, modified from Bear (2007, p 306)

$R = H\left(\frac{K}{2N}\right)^{\frac{1}{2}}$	Lembke (1886, 1887)	(5.1)
$R = 2.45\left(\frac{HKt}{n_e}\right)^{\frac{1}{2}}$	Weber (Schultze, 1924)	(5.2)
$R = 1.9\left(\frac{HKt}{n_e}\right)^{\frac{1}{2}}$	Kusakin (Aravin and Numerov, 1953)	(5.3)
$R = 3000 s_w K^{\frac{1}{2}}$	Siechardt (Chertousov, 1962)	(5.4)
$R = 575 s_w (HK)^{\frac{1}{2}}$		(5.5)

Variables	Definition	Units
R	Radius of influence	Length
H	Head in well	Length
K	Hydraulic conductivity	Length/Time
N	Porosity	Unitless
t	Pumping duration	Time
n_e	Effective porosity	Unitless
s_w	Aquifer storage coefficient	

For many scenarios, pumping time is not sufficient to develop pseudo-steady state conditions. Under transient conditions, for a well fully penetrating a confined aquifer, drawdown at any radial distance at any time can be calculated with the established Theis (1935) equation (Eq. 5.6a), relating drawdown (s) to discharge (Q), transmissivity (T) and the infinite series *well function* [w(u)]. The well function operator is determined by aquifer and pumping parameters, namely the radial distance in question (r), storativity (S), transmissivity, and pumping time (t).

$$s = \left(\frac{Q}{4\pi T}\right) w(u) \tag{5.6a}$$

$$u = (r^2 S)/(4Tt) \tag{5.6b}$$

$$w(u) = -0.5772 - \ln(u) + u - \frac{u^2}{2*2!} + \frac{u^3}{3*3!} - \frac{u^4}{4*4!} + \cdots \tag{5.6c}$$

Hantush (1961) solved for the partially penetrating case (Eq. 5.7a). These solutions are transient and drawdown reduces to zero as radial distance approaches infinite; thus, they do not explicitly solve for the radius of influence. In practice, some threshold for minimum

drawdown is selected, determined by factors such as measurement uncertainty, signal-to-noise ratio as determined by natural background water level fluctuations, or regulatory statutes.

Hantush (1961) solved for transient drawdown in partially penetrating wells by adding additional correction terms to the Theis equation. In addition to the same aquifer parameters and well discharge variables as the Theis equation (Eq. 5.6), the solution incorporates aquifer well construction details such as aquifer thickness (b), well screen length (*l*), depth to top of screen (d), and a modifier for vertical anisotropy in hydraulic conductivity (K_z and K_r). Hantush (1961) shows that a partially penetrating well affects drawdown at a greater distance than a fully penetrating well, all else equal.

$$s = Q/(4\pi T)\left[w(u) + 2b/(\pi(l - d))\sum_{n=1}^{\infty}\left(\frac{1}{n}\right)\left(\sin\left(\frac{n\pi l}{b}\right) - \sin\left(\frac{n\pi d}{b}\right)\right)\cos\left(\frac{n\pi z}{b}\right)w(u,\beta)\right] \quad (5.7a)$$

$$\beta = \sqrt{\frac{K_z}{K_r}} * \frac{n\pi r}{b} \quad (5.7b)$$

The simple cases described above assume that water mass displacement in the aquifer is only affected by pumping from a well. If a natural gradient exists, water will naturally flow from high to low pressure, driving the system in one direction. In this case, the cone of depression is altered in the flow direction, lengthening in the upgradient direction and

shortened downgradient, as the natural gradient drives water toward and away from the well. Under such conditions, water directly upgradient will eventually be captured by the well, along with water some distance normal to the gradient direction, determined by the aquifer properties and well discharge rate. Immediately downgradient of the well, the natural gradient is overwhelmed by the induced gradient and water also flows toward the well. At some distance directly downgradient, the natural gradient and induced gradient are in balance, producing a point where the theoretical water velocity is zero. This stagnation point (X_s) marks the farthest downgradient capture point. Flow beyond X_s can still be retarded by the pumping influence, but net advection proceeds in the direction of the natural gradient. Using only the pumping well discharge (Q_w), specific discharge (q_0), and aquifer thickness (B), the Bear and Jacobs (1965) solution solves for X_s (Figure 5.1).

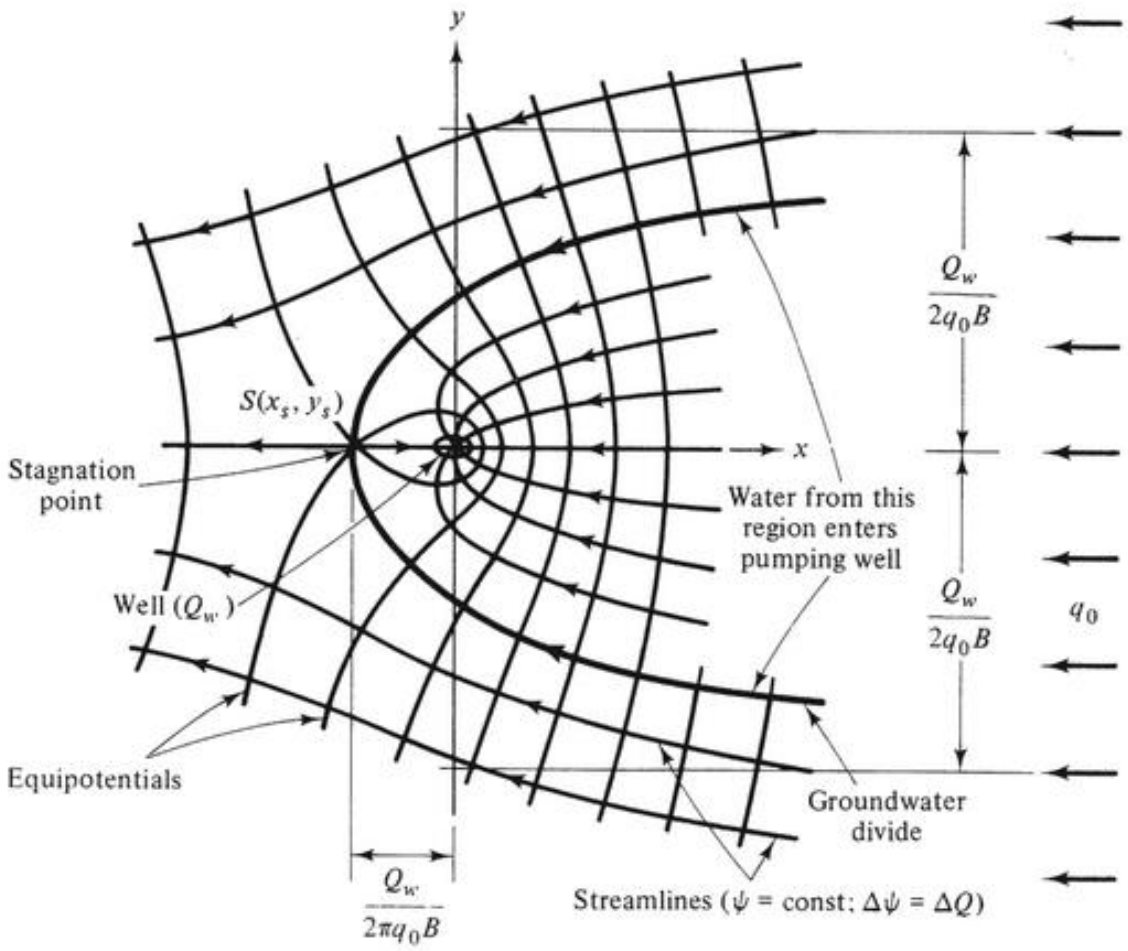

Figure 5.1 – Graphic detailing Jacob and Bear (1965) stagnation point solution for a single well in uniform flow, from Bear (2007, p 368).

$$X_s = -\frac{Q_w}{2\pi q_0 B} \tag{5.8}$$

Bounding Observations

In this study, valve operations at two boreholes and unintentional leakage from one overpressured borehole are analogous to pumping wells. The timing and discharge rates of these events are reasonably constrained, and observations and calculations from Chapter 3 and Fisher (2008) constitute limits on the remaining variables necessary to conduct capture zone analyses. Three "pumping events" occurred at the study site, from boreholes 1301A (leakage), and 1362A/B (ball valve operations). Tracer results described in Chapter 4 establish hypothesized captured zones. The analytic results presented here are intended to support the low-effective porosity conceptual model by expanding the body of internally consistent evidence.

Pumping Well Analogs

Borehole 1301A was drilled during IODP Expedition 301 in July 2004. Initially, cool, dense ocean water flowed into the borehole. Despite attempts to seal 1301A, temperature sensors indicated that flow into the borehole continued for several years, until formation pressure overcame the density-driven downward flow, and flow reversed at some point in Fall 2007. 1301A then discharged formation fluid for the duration of this tracer study, "pumping" at 5±2 L/s (Neira et al., 2016).

At 1362B, tracers were injected following drilling and casing on IODP Leg 327 in July 2010. Tracers drifted for approximately one year, until a ball valve on the 1362B wellhead was opened in the summer of 2011 to conduct a tracer recovery experiment. This experiment was

intended to last one year, but the 2012 cruise was delayed until the summer of 2013, resulting in two years of discharge at 4±1 L/s.

Upon closing the 1362B ball valve in Summer 2013, an identical valve on 1362A was opened, causing discharge at a presumably similar rate, until the valve was closed in the summer of 2014.

Aquifer Property Constraints

Discharge and timing from the various "pumping" events constrain well discharge Q_w and time t for application in capture zone analyses. Fisher et al. (2008) analyzed the cross-borehole pressure response to post-drilling fluid flow at the 1301A, 1301A, and 1026B boreholes. These results provide crucial constraints on aquifer transmissivity (T) and storativity (S). Winslow et al. (2016) determined that crustal aquifer thickness B of 100 - 300 meters allows hydrothermal convection, and borehole geometry at this site dictates that $B \geq 200$ m. Neira et al. (2016) determined discharge from ball valve operations, presented tracer results from the first three years of the nine-year study, and estimated that effective porosity is two to three orders of magnitude less than bulk porosity.

Table 5.1 - Model Parameters

Variable	Description	Minimum	Maximum	Units	Source
Q_w (1301A)	1301 Discharge	3	7	L/s	Fisher et al. (2008)
Q_w (1362B)	1362B Discharge	3	5	L/s	Neira et al. (2016)
Q_w (1362A)	1362A Discharge	3	5	L/s	Assumed
t_{1301A}	1301A Pump Time at 2010 injection	2.5	3	years	Fisher (et al. 2008)
t_{1362B}	1362B Pump Time at 2013 Expedition	2		years	Observed
t_{1362A}	1362B Pump Time at 2014 Expedition	2		years	Observed
T	Transmissivty	5×10^{-3}	1.2×10^{-2}	m^2/s	Fisher et al. (2008)
S	Storativity	1×10^{-3}	3×10^{-3}	unitless	Fisher et al. (2008)
V_x	Linear Velocity	0.5	1.0	m/d	Chapter 4
n_e	Efective Porosity	1×10^{-4}	1×10^{-1}	unitless	Chapter 4
B	Aquifer Thickness	200	300	m	Winslow et al. (2016)

Conceptual Capture Zones

In Chapter 4, a conceptual model was hypothesized that several specific tracer results can be explained by well capture analysis. The primary set of observations is the near-immediate and persistent tracer arrival at downgradient borehole 1362A coupled with the transient upgradient tracer arrival at 1301A.

The conceptual model hypothesizes that the 500 m^3 tracer injection displaced fluid through the low effective porosity fracture system approximately 328 m radially from the injection location, emplacing a tracer patch extending from 1362B to 1362A. Concurrently, fluid would be displaced a similar distance in the opposite direction, approximately two thirds of the distance from the injection hole to upgradient hole 1301A. This results in the patch extending

to within approximately 220 m of 1301A. The gradient direction appears well-established by the persistent tracer signals at 1362B and 1362A for the duration of the nine-year study, so an explanation is needed for the 1301A signal. Localized convection and preferential flowpaths might be invoked, but here a case that leakage from 1301A, which was sufficient to induce a capture zone extending into the emplaced tracer patch, is presented.

Interestingly, ball valve operations at 1362B and 1362A seemed to have no observable effect on the respective non-discharging boreholes. This suggests that the combination of discharge rate and time at these locations was not sufficient to induce a significant response at over 300 m distance. Even in the discharging boreholes themselves, response to ball valve operations in the respective tracer records are inconsistent.

At 1362B, there is a clear and immediate response in the Cs signal, indicative of the nonconservative ionic tracer being remobilized from weak bonding on surfaces near the borehole. Unfortunately, SF_6 data from that time were lost due to over pumping. Neira et al. (2016) postulated that isolated extremely high SF_6 detections in 1362B at approximately 700 DPI were a return pulse drawn to the borehole, but it is difficult to support this conclusion owing to the lack of significant rising or falling limb components of these detections. Dispersion as calculated in Chapter 2 and field and laboratory data from 1026B, 1362A, and storage study coils indicate that dispersion on a scale of ±10 m (equating to 20-40 days) at a minimum is expected, so these detections are possibly the result of laboratory error.

At 1362A, Cs concentrations were close to background levels, making changes difficult to discern. The SF_6 record does span the closing of the 1362B ball valve and opening at 1362A.

In isolation, the SF_6 data appears to show a response to discharge at 1362A, but a similar response is seen at 1362B at the same time. This corresponds with the start of new wellhead coils at both locations and changes in analytical procedures. As explained in Chapter 3, evidence suggests that those changes resulted in apparent [SF_6] increases at all instances when new analytical methods superseded old methods.

If operations truly did not induce measurable [SF_6] responses in the discharging boreholes 1362B and 1362A, this is a peculiar result that demands explanation. If the tracer patch emplacement resulted in a relatively homogenized filling of all effective porosity in the area spanning the two boreholes, it is possible that discharge increased formation fluid throughput past the sampler intakes without significantly changing the conservative-behaving SF_6 tracer concentration.

Borehole 1026B was not completed with a wellhead ball valve, and suspected slight leakage was not likely to induce significant well capture. However, the 235 m distance between 1362A and 1026B is shorter than the spacing between any other pair of boreholes, so the one year of discharge from 1362A may have been adequate to draw some tracer back across 1026B. As 1026B is not precisely aligned with the other boreholes, it is also possible that only the dispersed fringe of the tracer patch reached 1026B, complicating conclusions drawn from observations there.

Table 5.2 - Conceptualized Capture Zones

Variable	Description	Minimum	Maximum	Units	Source
X_s (1301A)	1301A Stagnation Point	220	550	m Towards 1362B	Chapter 4
X_s (1362B)	1362B Stagnation Point	Unknown	<311	m Towards 1362A	Chapter 4
X_s (1362A)	1362A Stagnation Point	235	<311	m Towards 1026B	Chapter 4

Analytical Solutions

Progressing from the simplest solution to the more complex, applications of well capture analysis solutions are presented using the paraments described in previous sections. While numerous assumptions and ranges of parameter values are applied to these solutions, the results from conservative and maximized sets of parameters are used to establish meaningful constraints. These results demonstrate that analytical solutions using parameters from Table 5.1produce results consistent with the conceptualized capture zones drawn from tracer results and summarized in Table 5.2.

Theis Transient Drawdown Solutions

For the conceptual model to be supported, discharge from 1301A must induce a capture zone that overlaps with the hypothesized tracer patch centered at borehole 1362B. This equates to a distance > 220 m from 1301A. Parameters for calculating drawdown using Equation 5.1 include Transmissivity (T), Storativity (S), Discharge (Q_w), and time (t). By

reorganizing these parameter ranges according to their respective effects on drawdown at a given distance (Table 5.3), the following results were obtained (Table 5.4):

Table 5.3 - Theis Parameters and Effects

Variable	Description	Minimizing	Maximizing	Units	Source
Q_w (1301A)	1301A Discharge	3	7	L/s	Fisher et al. (2008)
Q_w (1362A)	1362B Discharge	3	5	L/s	Neira et al. (2016)
Q_w (1362B)	1362A Discharge	3	5	L/s	Assumed
t_{1301A}	1301A Pump Time at 2010 Injection	2.5	5	years	Fisher et al. (2008)
t_{1362B}	1362B Pump Time at 2013 Expedition	2		years	Known
t_{1361A}	1362B Pump Time at 2014 Expedition	2		years	Known
T	Transmissivity	5×10^{-3}	1.2×10^{-2}	m^2/s	Fisher et al. (2008)
S	Storativity	3×10^{-3}	1×10^{-3}	Unitless	Fisher et al. (2008)

Table 5.4 - Theis Results

Variable	Description	Minimized	Maximized	Unit
S_{220} (1301A)	Drawdown from 1301A at 220 m	0.19	0.22	m
S_{550} (1301A)	Drawdown from 1301A at 550 m	0.15	0.19	m
S_{311} (1362B)	Drawdown from 1362B at 311 m	0.17	0.21	m
S_{235} (1362A)	Drawdown from 1362A at 235 m	0.16	0.20	m
S_{311} (1362A)	Drawdown from 1362A at 311 m	0.17	0.65	m

Hantush Partially Penetrating Transient Drawdown Solutions

Winslow et al. (2016) showed that crustal convection on a 10^1 km scale is best supported by a 100 - 300 m aquifer thickness (B). Results presented here indicate that the system is permeable to at least 200 m, but only borehole 1362A extends past approximately 100 m into the basalt basement. As well depth approaches B and radius, r, approaches 1.5 x B (assuming vertical isotropy), the effects of partial penetration do become negligible (Hantush, 1961), but the effect cannot be ignored for discharge from 1301A, which was drilled only 108 meters into the basement. The well construction details were applied to Equation 5.2, using the conservative estimates of B = 300 meters, to show that the effects of partial penetration are measurable but relatively small (Table 5.5).

Table 5.5 - Comparison of Theis and Hantush Results

Variable	Description	Minimized		Units
		Theis	Hantush	
S_{220} (1301A)	Drawdown from 1301A at 220 m	0.19	0.22	m
S_{550} (1301A)	Drawdown from 1301A at 550 m	0.15	0.19	m
S_{311} (1362B)	Drawdown from 1362B at 311 m	0.17	0.21	m
S_{235} (1362A)	Drawdown from 1362A at 235 m	0.16	0.20	m
S_{311} (1362A)	Drawdown from 1362A at 311 m	0.17	0.19	m

Stagnation Point Analyses

The Theis and Hantush results indicate that drawdown reasonably can be induced at the required distances using parameters within the established ranges. Conversely, at the maximum allowable distances, drawdown is possibly negligible. It is important to note that

these solutions assume homogeneous, isotropic conditions, *with no natural gradient driving flow in the system*. If a gradient is applied, natural flow would decrease drawdowns in the downgradient direction and result in stagnation points at distances from each respective discharging well less than the respective calculated radii of influence. Applying the parameters in Table 5.1 to Equation 5.8, steady state stagnation points for each discharge event can be calculated. Effective porosity is the most poorly-constrained variable (10^{-3} to 10^{-1}), so by holding X_s constant at the conceptualized values, B to 300 m, and V_x to 0.83 m/d, while varying n_e, it can be determined if values within the range could produce the required X_s.

Table 5.6 - Stagnation Point Results for Fully Penetrating Wells in Uniform Isotropic Flow

Discharge Well	Stagnation Point X_e (m)	n_e (min Q_w)	n_e (max Q_w)
1301A	>200	7.0×10^{-4}	1.6×10^{-3}
1301A	<550	3.1×10^{-5}	3.1×10^{-5}
1362A/B	<311	5.3×10^{-4}	8.9×10^{-4}
1362A	>235	7.8×10^{-4}	1.2×10^{-3}
Average Values		5.1×10^{-4}	1.1×10^{-3}
10^1 Correction		5.1×10^{-3}	1.1×10^{-2}
10^2 Correction		5.1×10^{-2}	1.1×10^{-1}

The stagnation points at the limiting distances can be achieved within the range of n_e values calculated in Chapter 4 (Table 4.5). The resulting values, however, are all on the extreme low end of those estimates. Conclusions in Chapter 4 suggest that lateral anisotropy is up to a factor of 10, which would elongate the capture zones and displace the stagnation points farther downgradient. Partially penetrating well effects would also positively displace the stagnation points, though to a lesser extent than anisotropy. If vertical anisotropy is also a factor, this

would further elongate the capture zones. It thus is appropriate to apply a correction factor to account for these variables, ranging from one to two orders of magnitude.

Conclusions

These results illustrate that observed tracer results interpreted as well capture phenomena can be analytically achieved with existing capture zone analysis solutions using parameters consistent with site-specific literature (e.g., Fisher et al., 2008; Neira et al., 2016; Winslow et al., 2016) and supports the new conceptual model developed in this work. Discharges from the various boreholes can reasonably produce radii of influence to the necessary extents, and low effective porosity values consistent with Neira et al., (2016) and the new conceptual model establish stagnation points at appropriate locations. Corrections for vertical and horizontal anisotropy establish a range of effective porosity values limited at the maximum at the observed bulk porosity in basalt cores (approximately 10^{-1}) and, at a minimum, approximately 5×10^{-3}, consistent with estimates developed using mass-balance methods in Neira et al. (2016). Ultimately, capture zone analyses provide additional internally consistent support for the low effective porosity hypothesis.

References

Aravin, V.I. and Numerov, S.N., *Theory of Motion of Liquids in Gases in Undeformable Porous Media* (Russian), Gostekhizdat, Moscow, pp 616. (English translation by A. Moscona, Isreal Prof. for Scientific Transfer, pp 511, 1965), 1953.

Bartetzko, A., & Fisher, A. T. (2008). Physical properties of young (3.5 Ma) oceanic crust from the eastern flank of the Juan de Fuca Ridge: Comparison of wireline and core measurements with global data. Journal of Geophysical Research: Solid Earth, 113(5). http://doi.org/10.1029/2007JB005268

Bartetzko, A., & Fisher, A. T. (2008), Physical properties of young (3.5 Ma) oceanic crust from the eastern flank of the Juan de Fuca Ridge: Comparison of wireline and core measurements with global data, J. Geophys. Res., 113, B05105, doi:10.1029/2007JB005268.

Bear, J., & Bachmat, Y., "Transport Phenomena in Porous Media-Basic Equations," Fundamentals of Transport Phenomena in Porous Media, J. Bear and M. Y. Corapcioglu, eds., Martinus Nijhoff Publishers BV, The Hague, The Netherlands, 1984, pp. 3–62.

Bear, J., Jacobs, M., On the movement of water bodies injected into aquifers*, Journal of Hydrology*, Volume 3, Issue 1, 1965, Pages 37-57,ISSN 0022-1694, https://doi.org/10.1016/0022-1694(65)90065-X.

Bear, Jacob. *Hydraulics of Groundwater*. Dover Publications, 2007. Pp 386

Becker, K., Fisher, A. T., & Tsuji, T. (2013). New packer experiments and borehole logs in upper oceanic crust: Evidence for ridge-parallel consistency in crustal hydrogeological properties. Geochemistry, Geophysics, Geosystems, 14(8). http://doi.org/10.1002/ggge.20201

Bullister, J. L., Wisegarver, D. P., & Menzia, F. A. (2002). The solubility of sulfur hexafluoride in water and seawater, 49, 175–187.

Carson, B., Baker, E. T., Hickey, B. M., Nittrouer, C. a., DeMaster, D. J., Thorbjarnarson, K. W., & Snyder, G. W. (1986). Modern sediment dispersal and accumulation in Quinault submarine canyon — A summary. *Marine Geology*, *71*(1-2), 1–13. doi:10.1016/0025-3227(86)90030-7

Carson, B., Yuan, J., Myers, P. B., Barnard, W. D., & Barnard, W. D. (1974). Initial Deep-Sea Sediment Deformation at the Base of the Washington Continental Slope : A Response to Subduction. *Geology*, (November), 561–564. doi:10.1130/0091-7613(1974)2<561

Chapin, T. P. (2015). Applied Geochemistry long-duration water sampling in acid mine drainage studies : A short review of current methods and recent advances in automated water samplers. Applied Geochemistry, 59, 118–124. http://doi.org/10.1016/j.apgeochem.2015.04.004

Christensen, N. I., & Ramananantoandro, R. (1988). Permeability of the oceanic crust based on experimental studies of basalt permeability at elevated pressures. Tectonophysics, 149(1–2), 181–186. http://doi.org/10.1016/0040-1951(88)90126-6

Clark, J. F., G. B. Hudson, and D. Avisar. (2005). "Gas transport below artificial recharge ponds:

Insights from dissolved noble gases and a dual gas (SF_6 and ^3He) tracer experiment." Environmental Science and Technology 39: 3939-3945.

Crank, J. 1975. The mathematics of diffusion, 2nd ed. Oxford, pp 89-103.

Davis, E. E., Chapman, D.S., Mottl, M. J., Bentkowski, W.J., Dadey, K., Forster, C., Harris, R., Nagihara, S., Rohr, K., Wheat, G., Whiticar, M. (1992). FlankFlux: an experiment to study the nature of hydrothermal circulation in young oceanic crust. Can. J. Earth Sci. 29, 925–952

Davis, E. E., Mottl, M. J., & Fisher, A. T. (1991). Scientific Report - Ocean Drilling Progam, Leg 139 Preliminary Report, Middle Valley, Juan de Fuca Ridge.

Davis, E., Fisher, A. T., & Firth, J. (1996). Ocean Drilling Program Leg 168 Preliminary Report Hydrothermal Circulation in the Oceanic Crust : Eastern Flank of the Juan De Fuca Ridge.

Davis, E., Mottl, M., Fisher, A. (1991), Ocean Drilling Program Leg 139 preliminary report, Middle Ridge, Juan de Fuca Ridge. Preliminary Report No. 39, Proceedings of the Ocean Drilling Program, Texas A&M University.

Duncan, R. A., & Hogan, L. G. (1994). Radiometric dating of young MORB using the 40Ar- 39Ar incremental heating method. Geophysical Research Letters, 21(18), 1927–1930. http://doi.org/10.1029/94GL01375

Elder, J. W. (1965). Physical Processes in Geothermal Areas. Terrestrial Heat Flow, 8, 211–239.

Elderfield, H., Wheat, C. G., Mottl, M. J., Monnin, C., & Spiro, B. (1999). Fluid and geochemical transport through oceanic crust: A transect across the eastern flank of the Juan de Fuca

Ridge. Earth and Planetary Science Letters, 172, 151–165. http://doi.org/10.1016/S0012-821X(99)00191-0

Expedition 321T Scientists, (2009). Juan de Fuca hydrogeology: cementing operations at the Hole U1301A and Hole U1301B borehole observatories (CORKS). IODP Preliminary Report, 321T. doi:10.2204/iodp.pr.321T.2009

Fisher, A. T. (1998). Permeability Within Basaltic Oceanic Crust. Physics of the Earth and Planetary Interiors, 145(97), 143–182. http://doi.org/8755-1209/98/97RG-02916515

Fisher, A. T. (2004). Rates of flow and patterns of fluid circulation. Hydrogeology of the Oceanic Lithosphere, 339–377.

Fisher, A. T. (2005). Marine hydrogeology: Recent accomplishments and future opportunities. Hydrogeology Journal, 13, 69–97. http://doi.org/10.1007/s10040-004-0400-y

Fisher, A. T., Becker, K., & Davis, E. E. (1997). The Permeability of Young Oceanic Crust East of Juan de Fuca Ridge Determined Using Borehole Thermal Measurements. Geophysical Research Letters, 24(11), 1311–1314.

Fisher, A. T., Cowen, J., Wheat, C. G., & Clark, J. F. (2011). Preparation and injection of fluid tracers during IODP Expedition 327, eastern flank of Juan de Fuca Ridge. Proceedings of the Integrated Ocean Drilling Program (IODP), 327, 1–26. http://doi.org/10.2204/iodp.proc.327.108.2011

Fisher, A. T., Davis, E. E., and Becker, K. (2008), Borehole-to-borehole hydrologic response across 2.4 km in the upper oceanic crust: Implications for crustal-scale properties*, J. Geophys. Res.*, 113, B07106, doi:10.1029/2007JB005447.

Fisher, A. T., Tsuji, T., & Petronotis, K. (2011). Site U1301. Proceedings of the Integrated Ocean Drilling Program (IODP), 327, 1–10. http://doi.org/10.2204/iodp.proc.327.104.2011

Fisher, A. T., Urabe, T., & Klaus, A. (2005). IODP Expedition 301 Installs Three Borehole Crustal Observatories, Prepares for Three-dimensional, Cross-Hole Experiments in the Northeastern Pacific Ocean. Scientific Drilling, (1). http://doi.org/10.2204/iodp.sd.1.01.2005

Fisher, A. T., Urabe, T., & Klaus, A. (2005). Site U1301. Proceedings of the IODP, 301, 1–181. doi:10.2204/iodp.proc.301.106.2005

Fisher, A. T.; Becker, K. (2000). Channelized fluid flow in oceanic crust reconciles heat-flow and permeability data. Nature, 403(January), 71–74.

Fisher, A., Davis, E., Hutnak, M., Spiess, V., Zühlsdorff, L., Cherkaoui, A., Christiansen, L., Edwards, K., Macdonald, R., Villinger, H., Mottl, M. J., Wheat, C.G., Becker, K. (2003). Hydrothermal recharge and discharge across 50 km guided by seamounts on a young ridge flank. Nature, 421(February), 618–621. http://doi.org/10.1038/nature01352

Fisher, A.T., and Davis, E.E., (2000). An introduction to the scientific results of Leg 168. In Fisher, A.T., Davis, E.E., and Escutia, C. (Eds.), Proc. ODP, Sci. Results, 168: College Station TX (Ocean Drilling Program), 3–8.

Fisher, A.T., Becker, K., Clark, J., Cooper, S., Cowen, J., Edwards, K., Glazer, B., Hulme, S., Orcutt, B., Wheat, C.G., (2011), Preliminary Cruise Report for R/V Atlantis/ROV Jason-II Expedition AT18-07:Hydrogeologic, Geochemical, and Microbiological Experiments in Young Ocean Crust of the Northeastern Pacific Ocean Using Subseafloor Observatories

Fisher, A.T., Becker, K., Clark, J., Cooper, S., Hsieh, C., Jungbluth, S., Orcutt, B., Steward, G., Wheat, C.G., (2013), Preliminary Cruise Report for R/V Atlantis/ROV Jason-II Expedition AT26-03: Hydrogeologic, Geochemical, and Microbiological Experiments in Young Ocean Crust of the Northeastern Pacific Ocean Using Subseafloor Observatories

Fisher, A.T., Urabe, T., Klaus, A., and the Expedition 301 Scientists, (2005). Proceedings of IODP, 301: College Station TX (Integrated Ocean Drilling Program Management International, Inc.). doi:10.2204/iodp.proc.301.2005

Gelesh, L., Marshall, K., Boicourt, W., & Lapham, L. (2016). Methane concentrations increase in bottom waters during summertime anoxia in the highly eutrophic estuary, Chesapeake Bay, USA. Limnology and Oceanography, 61(2011), 253–266. http://doi.org/10.1002/lno.10272

Gkritzalis-Papadopoulos, A. (2009). Development of an autonomous water sampler.

Griggs, G. B., Carey, A. G., & Kulm, L. D. (1969). Deep-sea sedimentation and sediment-fauna interaction in Cascadia Channel and on Cascadia Abyssal Plain. Deep Sea Research and Oceanographic Abstracts, 16(2), 157–170. doi:10.1016/0011-7471(69)90071-0

Gutiérrez-Pastor, J., Nelson, C. H., Goldfinger, C., & Escutia, C. (2013). Sedimentology of seismo-turbidites off the Cascadia and northern California active tectonic continental margins, northwest Pacific Ocean. Marine Geology, 336, 99–119. doi:10.1016/j.margeo.2012.11.010

Hantush, M.S., Drawdown around a partially penetrating well, *Journal of Hydraulics Division*, Vol. 87, Issue 4, Pp 83-98, 1961.

Haymon, R. Growth history of hydrothermal black smoker chimneys. Nature 301, 695–698 (1983). https://doi.org/10.1038/301695a0.

Heath, R. C. (1983). Basic Ground-Water Hydrology. Water-Supply Paper 2220. USGS.

Hutnak, M., Fisher, a. T., Zühlsdorf, L., Spiess, V., Stauffer, P. H., & Gable, C. W. (20i06). Hydrothermal recharge and discharge guided by basement outcrops on 0.7-3.6 Ma seafloor east of the Juan de Fuca Ridge: Observations and numerical models. Geochemistry, Geophysics, Geosystems, 7. http://doi.org/10.1029/2006GC001242

Jannasch, H. W., Johnson, K. S., Sakamoto, C. M., Bay, M., Avenue, C., & Grove, P. (1994). Submersible, Osmotically Pumped Analyzers for Continuous Determination of Nitrate in Situ. Analytical Chemistry, 66(20). http://doi.org/10.1021/ac00092a011

Jannasch, H. W., Wheat, C. G., Plant, J., Kastner, M., & Stakes, D. (2004). Continuous chemical monitoring with osmotically pumped water samplers: OsmoSampler design and applications. Limnology and Oceanography: Methods, 2, 102–113. http://doi.org/10.4319/lom.2004.2.102

King, D. B., and E. S. Saltzman (1995), Measurement of the diffusion coefficient of sulfur hexafluoride in water, J. Geophys. Res., 100(C4), 7083–7088, doi:10.1029/94JC03313.

Knudson, K. P., & Hendy, I. L. (2009). Climatic influences on sediment deposition and turbidite frequency in the Nitinat Fan, British Columbia. Marine Geology, 262(1-4), 29–38. doi:10.1016/j.margeo.2009.03.002

Lapham, L., Wilson, R., Riedel, M., Paull, C. K., & Holmes, M. E. (2013). Temporal variability of in situ methane concentrations in gas hydrate-bearing sediments near Bullseye Vent , Northern Cascadia Margin, 14(7). http://doi.org/10.1002/ggge.20167

Leap, D. I., and Kaplan, P. G. (1988), A single-well tracing method for estimating regional advective velocity in a confined aquifer: Theory and preliminary laboratory verification, Water Resour. Res., 24(7), 993– 998, doi:10.1029/WR024i007p00993.

Lembke, K.E., Groundwater flow and the theory of water collectors (Russian), *The Engineer*, J. of the Ministry of Communication, no. 2, 1886 and nos. 17-19 1887.

Lister, B. (1972). On the Thermal Balance of a Mid-Ocean Ridge, 515–535.

MacDonald, K. C. (2001). MOR Tectonics, Volcanism, Geomorphology. Marine Geology, Earth 449, 1798–1813. http://doi.org/10.1006/rwos.2001.0094

Macdonald, K. C., Becker, K., Spiess, F.N., Ballard, R.D., (1980) Hydrothermal heat flux of the “black smoker” vents on the East Pacific Rise, Earth and Planetary Science Letters, Volume 48, Issue 1, 1980, Pages 1-7, ISSN 0012-821X, https://doi.org/10.1016/0012-821X(80)90163-6.

McQuillan, J. S., & Robidart, J. C. (2017). Molecular-biological sensing in aquatic environments: recent developments and emerging capabilities. Current Opinion in Biotechnology, 45, 43–50. http://doi.org/10.1016/j.copbio.2016.11.022

Moores, E. M., & Vine, F. J. (1971). The Troodos Massif, Cyprus and other Ophiolites as Oceanic Crust: Evaluation and Implications. Philosophical Transactions of the Royal Society A: Mathematical, Physical and Engineering Sciences, 268(1192), 443–467. http://doi.org/10.1098/rsta.1971.0006

Mottl, M. J. (1998). Warm springs discovered on 3.5 Ma oceanic crust, eastern flank of the Juan de Fuca Ridge. Geology 26, 51–54

Mottl, M. J., & Wheat, C. G. (1994). Hydrothermal circulation through mid-ocean ridge flanks: Fluxes of heat and magnesium. Geochimica et Cosmochimica Acta, 58(10), 2225–2237. http://doi.org/10.1016/0016-7037(94)90007-8

Moyer, C. L., Wheat, C. G., Jannasch, H. W., Plant, J. N., & Sansone, F. J. (2000). Continuous Sampling of Hydrothermal Fluids From Loihi Seamount After the 1996 Event.

Neira, N. M., Clark, J. F., Fisher, A. T., Wheat, C. G., Haymon, R. M., & Becker, K. (2016). Cross-hole tracer experiment reveals rapid fluid flow and low effective porosity in the upper oceanic crust. Earth and Planetary Science Letters, 450, 355–365. http://doi.org/10.1016/j.epsl.2016.06.048

Orcutt, B.N., Carr, S., Nigro, O., Rappe, M., (2019), Cruise Report for R/V Atlantis + ROV Jason Expedition AT42-11

Pitman, C., Herron, E. M., & Heirtzler, J. R. (1968). Magnetic anomalies in the Pacific and sea floor spreading. Journal of Geophysical Research, 73(6), 2069–2085. http://doi.org/10.1029/JB073i006p02069

Riedel, M., Collett, T.S., Malone, M.J., and the Expedition 311 Scientists, (2006), Expedition 311 summary, Proceedings of the Integrated Ocean Drilling Program, Volume 31

Rosenberg, N. D., & Spera, F. J. (1990). Role of anisotropic and/or layered permeability in hydrothermal convection. Geophysical Research Letters, 17(3), 235–238.

Rosenberg, N. D., Spera, F. J., & Haymon, R. M. (1993). The relationship between flow and permeability field in seafloor hydrothermal systems. Earth and Planetary Science Letters, 116, 135–152. http://doi.org/10.1016/0012-821X(93)90050-J

Saiers, J. E., & Hornberger, G. M. (1996). Migration of 137Cs through quartz sand: Experimental results and modeling approaches. Journal of Contaminant Hydrology, 22(3–4), 255–270. http://doi.org/10.1016/0169-7722(95)00094-1

Silver, E. A. (1972). Pleistocene tectonic accretion of the continental slope off Washington. Marine Geology, 13, 239–249.

Theis, C. V. (1935), The relation between the lowering of the Piezometric surface and the rate and duration of discharge of a well using ground-water storage, *Eos Trans. AGU*, 16(2), 519– 524, doi:10.1029/TR016i002p00519.

Tréhu, A.M., Bohrmann, G., Rack, F.R., Torres, M.E., et al., (2003), Leg 204 Summary, Proceedings of the Ocean Drilling Program, Initial Reports, Volume 204

Tryon, M. D., Henry, P., & Hilton, D. R. (2012). Quantifying submarine fluid seep activity along the North Anatolian Fault Zone in the Sea of Marmara. Marine Geology, 315–318, 15–28. http://doi.org/10.1016/j.margeo.2012.05.004

Underwood, M. B., & Hoke, K. D. (2000). Composition and provenance of turbidite sand and hemipelagic mud in northwestern Cascadia Basin. Proceedings of the Ocean Drilling Program, Scientific Results, Hydrothermal Circulation in the Oceanic Crust, Eastern Flank of the Juan de Fuca Ridge; Covering Leg 168 of the Cruises of the Drilling Vessel JOIDES Resolution, San Francisco, California, to , 168, 51–65.

Visser, A., Singleton, M., &Esser, B. (2014). Xenon Tracer Test at Woodland Aquifer Storage and Recovery Well. Project Report, Livermore, CA: Lawrence Livermore National Laboratory.

Wheat, C. G., & Mottl, M. J. (2000). Composition of pore and spring waters from Baby Bare: Global implications of geochemical fluxes from a ridge flank hydrothermal system. Geochimica et Cosmochimica Acta, 64(4), 629–642. http://doi.org/10.1016/S0016-7037(99)00347-6

Winslow, D. M., Fisher, A. T., & Becker, K. (2013). Characterizing borehole fluid flow and formation permeability in the ocean crust using linked analytic models and Markov chain Monte Carlo analysis. Geochemistry, Geophysics, Geosystems, 14(9), 3857–3874. http://doi.org/10.1002/ggge.20241

Winslow, D. M., Fisher, A. T., Stauffer, P. H., Gable, C. W., & Zyvoloski, G. A. (2016). Three-dimensional modeling of outcrop-to-outcrop hydrothermal circulation on the eastern flank of the Juan de Fuca Ridge. *Journal of Geophysical Research: Solid Earth Research*,

121, 1365–1382. http://doi.org/10.1002/2016JB013304

Appendix A – Figures from Elderfield et al. (1999)

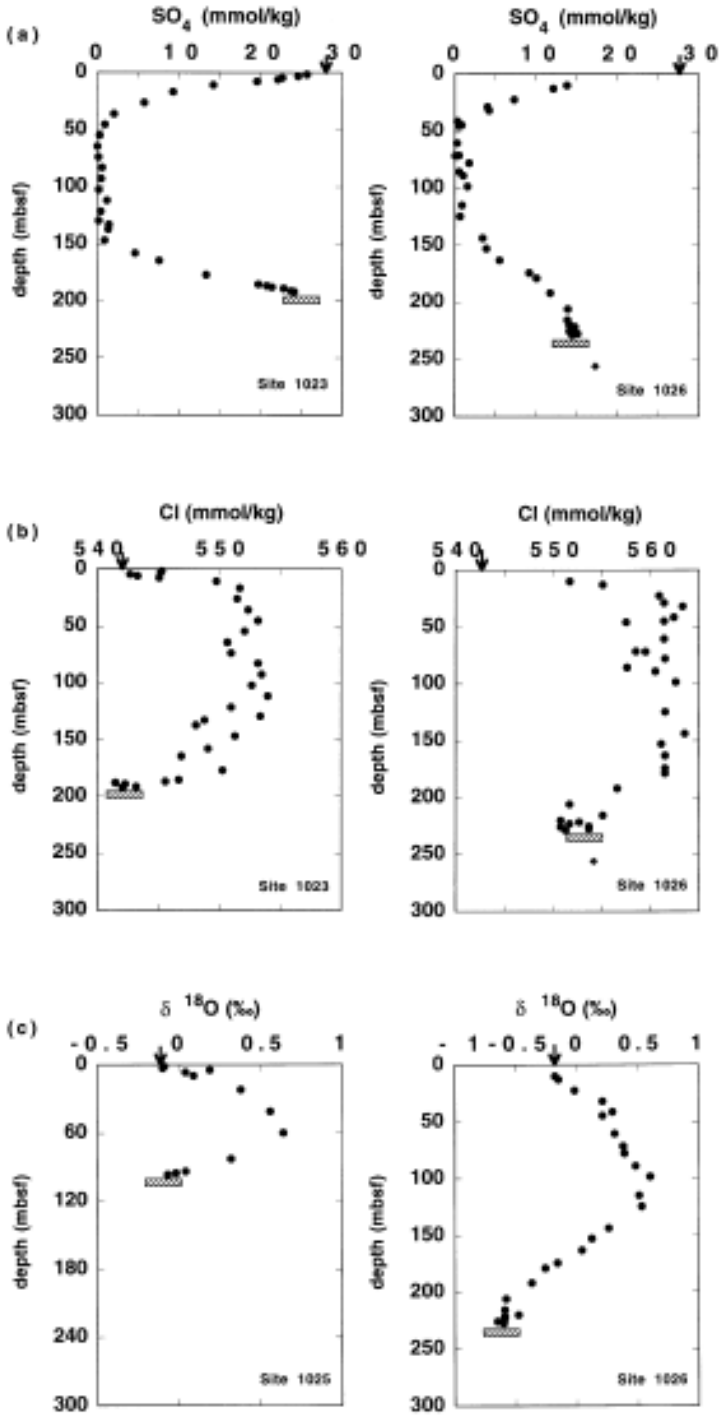

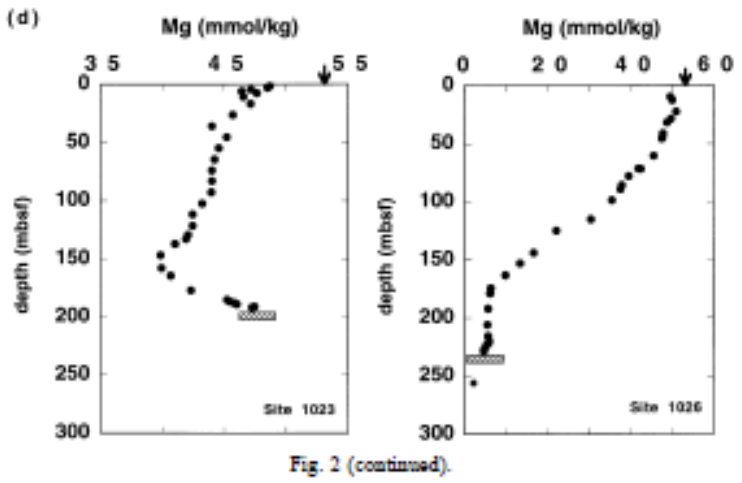

Fig. 2 (continued).

Figures (a) through (d) - Porewater profiles from ODP Sites 1023 and 1026 showing geochemical evolution in shallow sediment and trend toward younger water diffusing from basalt aquifer system.

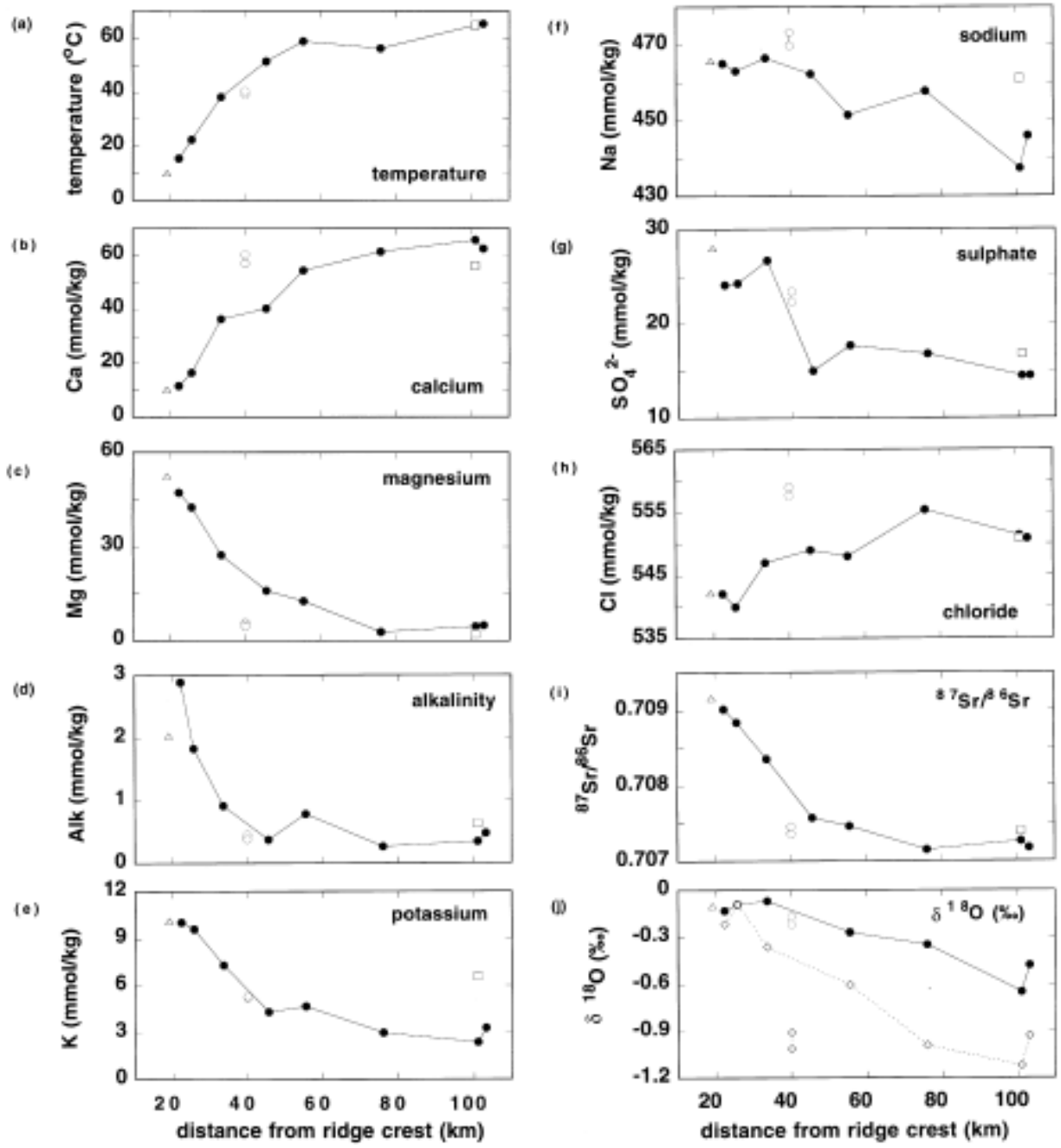

Figures (a) through (j) – Basal sediment water transects away from the Juan de Fuca ridge crest geochemical evolution from newly-infiltrated bottom water to formation water through exchange with basalt.

Appendix B - Tracer Results Plots

Plots:

Notes:

1. DL = detection limit
2. Downhole OS were installed through summer 2014
3. Wellhead OS were removed from 1026B and 1301A in summer 2014. Wellhead OS samplers for SF_6 continued operation at 1362A and 1362B until summer 2019

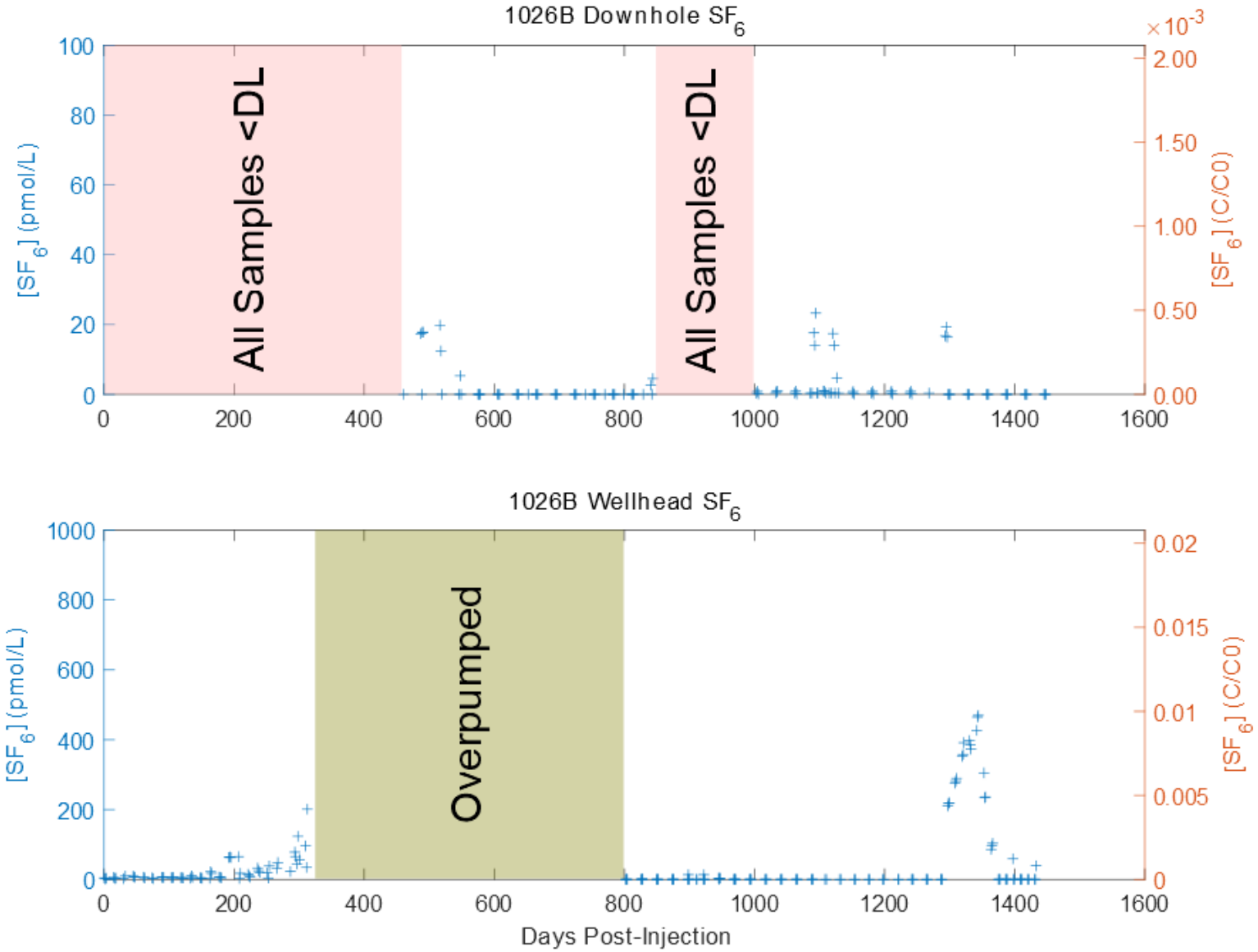
1026B Downhole SF6
All Samples <DL
All Samples <DL
[SF6] (pmol/L)
[SF6] (C/C0)
×10-3
1026B Wellhead SF6
Overpumped
[SF6] (pmol/L)
[SF6] (C/C0)
Days Post-Injection

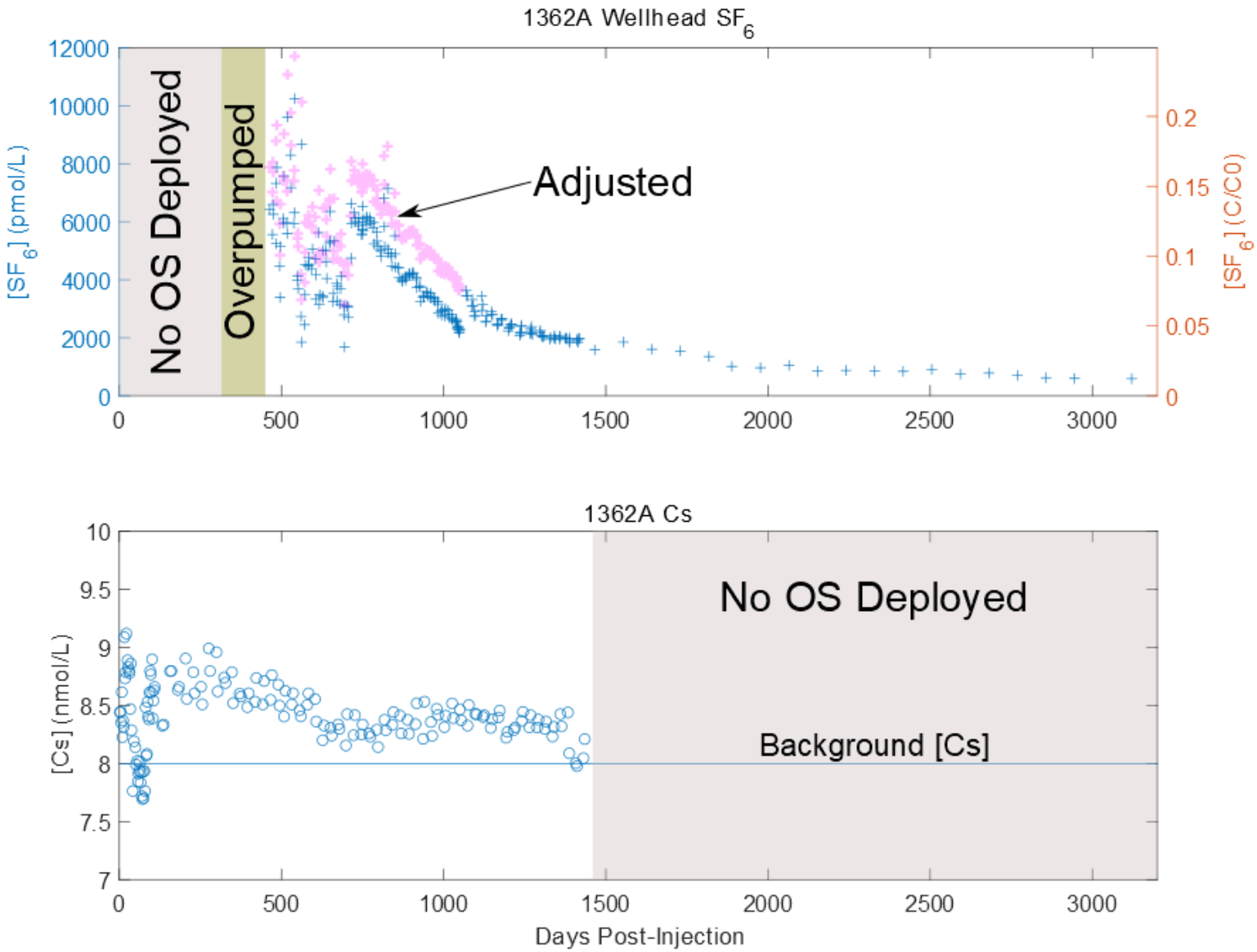
1362A Wellhead SF6
No OS Deployed
Overpumped
Adjusted
[SF6] (pmol/L)
[SF6] (C/C0)
0
2000
4000
6000
8000
10000
12000
0.05
0.1
0.15
0.2
0
500
1000
1500
2000
2500
3000
1362A Cs
No OS Deployed
Background [Cs]
[Cs] (nmol/L)
7
7.5
8
8.5
9
9.5
10
Days Post-Injection

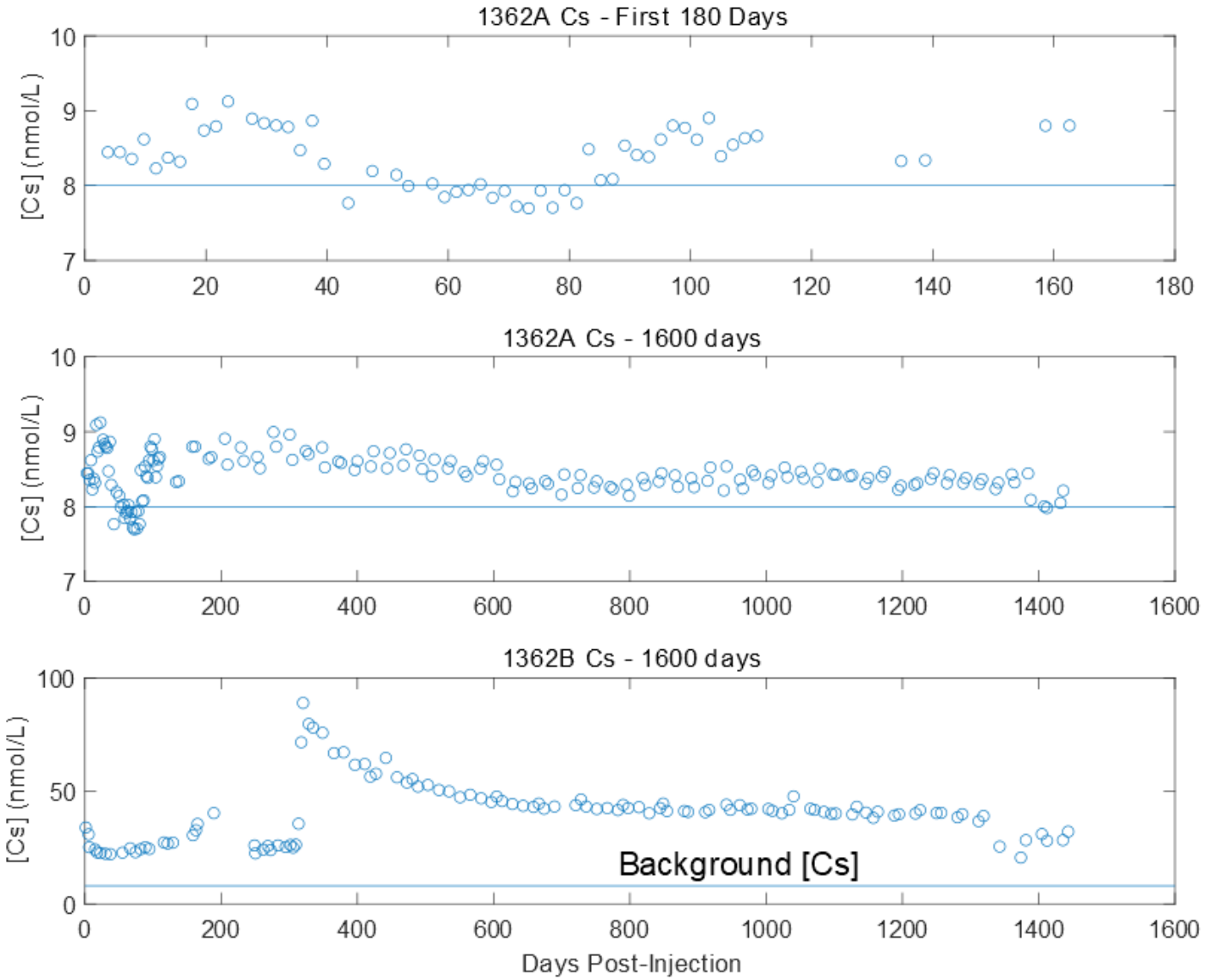
1362A Cs - First 180 Days
[Cs] (nmol/L)
10
9
8
7
0
20
40
60
80
100
120
140
160
180
1362A Cs - 1600 days
[Cs] (nmol/L)
10
9
8
7
0
200
400
600
800
1000
1200
1400
1600
1362B Cs - 1600 days
[Cs] (nmol/L)
100
50
0
Background [Cs]
0
200
400
600
800
1000
1200
1400
1600
Days Post-Injection

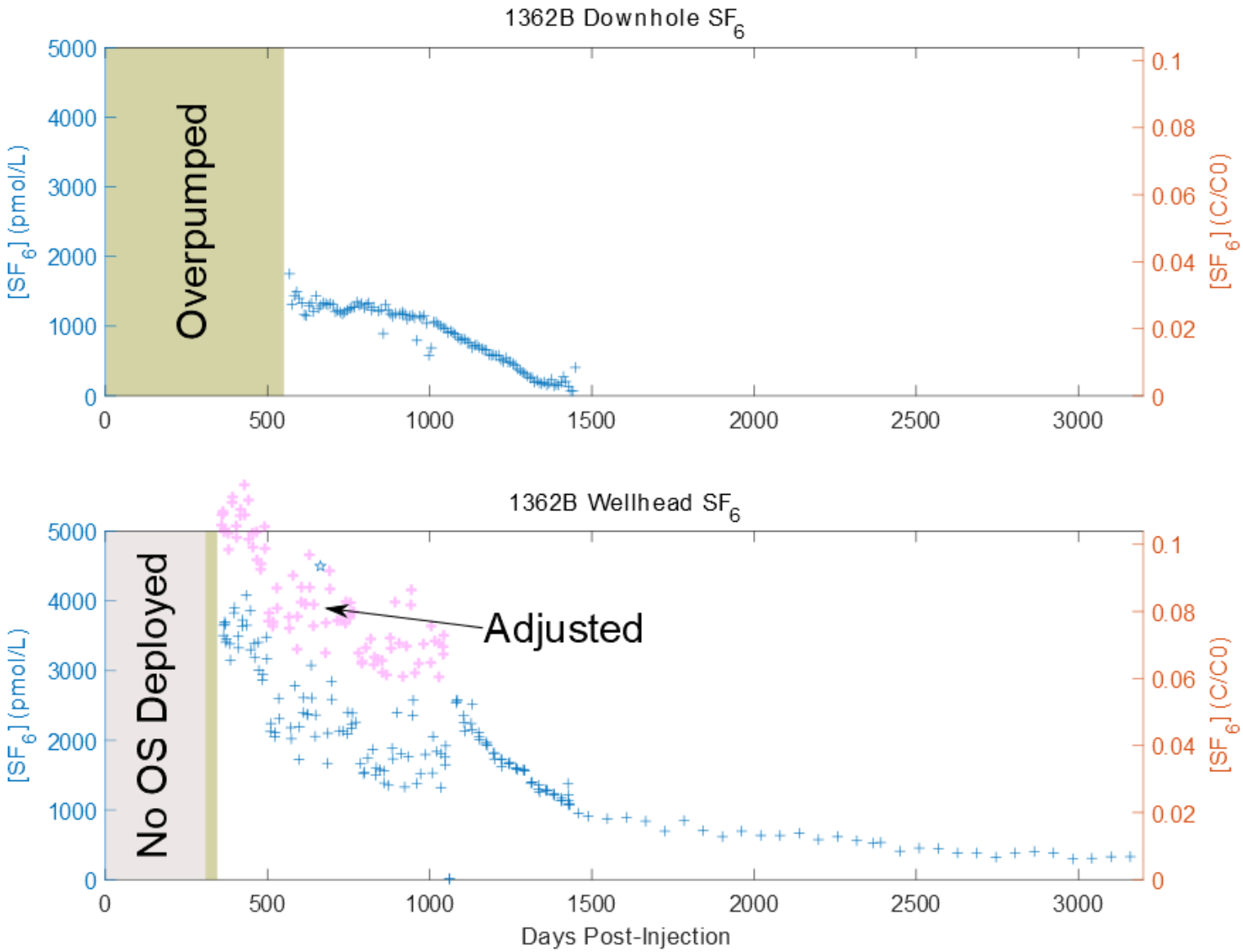
1362B Downhole SF6
Overpumped
[SF6] (pmol/L)
[SF6] (C/C0)
1362B Wellhead SF6
No OS Deployed
Adjusted
Days Post-Injection

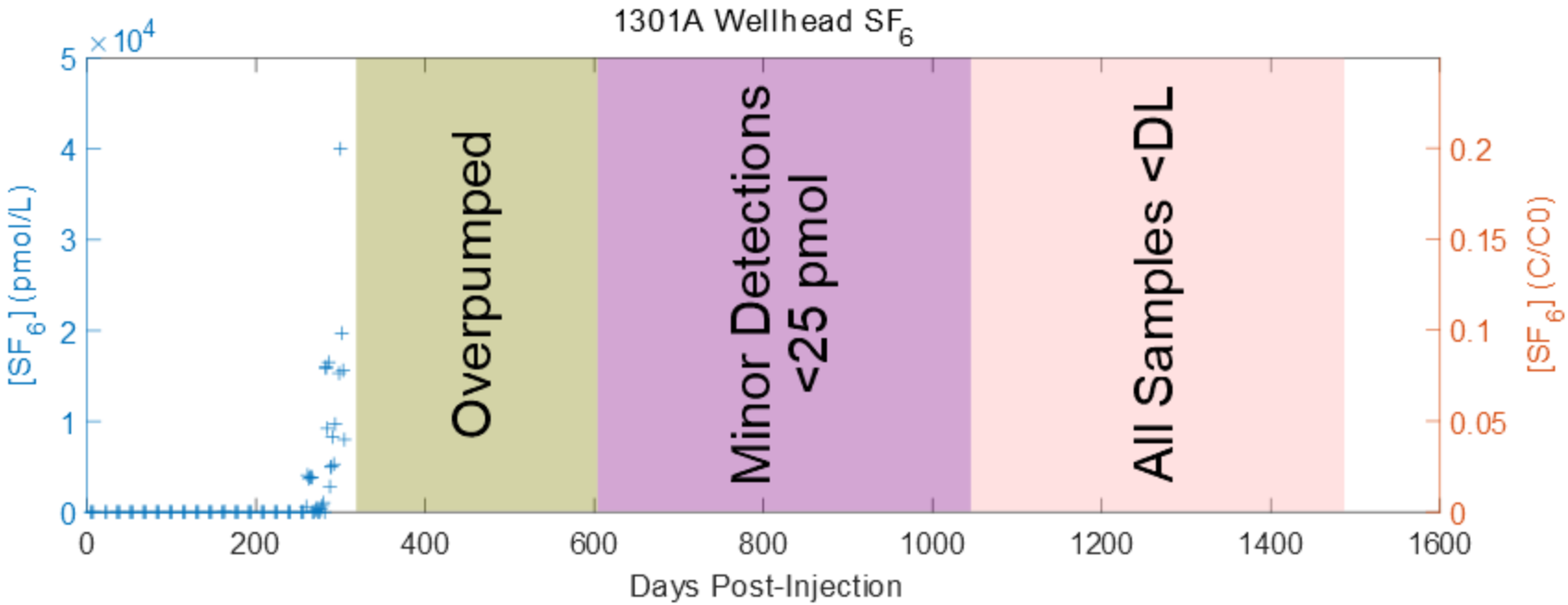
1301A Wellhead SF6
×10^4
5
4
3
2
1
0
[SF6] (pmol/L)
0.2
0.15
0.1
0.05
0
[SF6] (C/C0)
Overpumped
Minor Detections
<25 pmol
All Samples <DL
0
200
400
600
800
1000
1200
1400
1600
Days Post-Injection

Appendix C - Tracer Results Tables

Site: 1362B	Dataset: Downhole 2010-14	Analyte: SF6
Days Post Injection (DPI)	pmol/L	C/C0
575	1310.3	2.72E-02
583	1440.2	2.99E-02
590	1493.6	3.10E-02
598	1401.9	2.91E-02
605	1329.2	2.76E-02
613	1164.5	2.42E-02
620	1152.2	2.39E-02
627	1294.9	2.69E-02
635	1332.3	2.77E-02
642	1208.6	2.51E-02
650	1432.0	2.98E-02
657	1258.2	2.61E-02
664	1300.2	2.70E-02
672	1335.7	2.78E-02
679	1322.8	2.75E-02
687	1307.7	2.72E-02
694	1323.2	2.75E-02
701	1307.9	2.72E-02
709	1205.1	2.50E-02
716	1225.1	2.55E-02
724	1199.8	2.49E-02
731	1176.9	2.45E-02
738	1201.7	2.50E-02
746	1228.6	2.55E-02
753	1253.4	2.60E-02
761	1267.7	2.63E-02
768	1272.9	2.64E-02
775	1345.6	2.80E-02
783	1300.0	2.70E-02
790	1324.2	2.75E-02
798	1262.5	2.62E-02
805	1306.6	2.71E-02
812	1333.4	2.77E-02
820	1227.4	2.55E-02
827	1273.3	2.65E-02

842	1215.9	2.53E-02
850	1235.6	2.57E-02
857	893.8	1.86E-02
864	1306.9	2.72E-02
872	1224.6	2.54E-02
879	1177.1	2.45E-02
887	1141.5	2.37E-02
894	1180.0	2.45E-02
909	1176.7	2.44E-02
915	1201.1	2.50E-02
916	1167.5	2.43E-02
924	1175.1	2.44E-02
931	1097.6	2.28E-02
938	1143.4	2.38E-02
946	1156.0	2.40E-02
953	1121.1	2.33E-02
961	796.1	1.65E-02
968	1143.6	2.38E-02
975	1121.6	2.33E-02
983	1152.3	2.39E-02
990	1040.2	2.16E-02
998	581.0	1.21E-02
1005	688.8	1.43E-02
1012	1058.7	2.20E-02
1020	1058.7	2.20E-02
1027	1019.7	2.12E-02
1035	999.2	2.08E-02
1042	973.8	2.02E-02
1050	967.7	2.01E-02
1057	906.4	1.88E-02
1064	928.9	1.93E-02
1072	909.3	1.89E-02
1079	883.0	1.83E-02
1087	837.0	1.74E-02
1094	805.0	1.67E-02
1101	817.5	1.70E-02
1109	809.3	1.68E-02
1116	770.9	1.60E-02
1124	759.1	1.58E-02
1131	690.9	1.44E-02
1138	724.0	1.50E-02

1146	728.9	1.51E-02
1153	692.5	1.44E-02
1161	673.5	1.40E-02
1168	663.5	1.38E-02
1175	656.0	1.36E-02
1183	590.3	1.23E-02
1190	580.4	1.21E-02
1198	587.0	1.22E-02
1205	573.6	1.19E-02
1212	580.8	1.21E-02
1220	516.1	1.07E-02
1227	491.0	1.02E-02
1235	545.1	1.13E-02
1242	483.7	1.00E-02
1250	485.5	1.01E-02
1257	462.5	9.61E-03
1264	441.0	9.16E-03
1272	386.3	8.03E-03
1279	361.8	7.52E-03
1287	336.7	7.00E-03
1294	320.9	6.67E-03
1301	283.8	5.90E-03
1309	257.7	5.35E-03
1316	262.5	5.45E-03
1324	196.3	4.08E-03
1331	219.6	4.56E-03
1338	185.0	3.84E-03
1346	175.1	3.64E-03
1353	197.1	4.10E-03
1361	154.6	3.21E-03
1368	178.8	3.72E-03
1375	237.6	4.94E-03
1383	143.3	2.98E-03
1390	162.0	3.37E-03
1398	155.1	3.22E-03
1405	192.4	4.00E-03
1412	275.7	5.73E-03
1420	203.6	4.23E-03
1427	130.0	2.70E-03
1435	72.2	1.50E-03
1442	65.9	1.37E-03

1449	407.0	8.46E-03

Site: 1362B	Dataset: Downhole 2010-14	Analyte: Cs
Days Post Injection (DPI)	nmol/L	C/C0
2.3	33.5	N/A
6.5	30.5	N/A
7.4	24.8	N/A
16.0	23.8	N/A
19.1	22.5	N/A
24.0	22.2	N/A
31.3	21.9	N/A
38.6	21.7	N/A
56.2	22.4	N/A
67.6	24.3	N/A
75.3	22.6	N/A
82.8	23.9	N/A
89.9	24.8	N/A
95.6	24.0	N/A
116.9	26.9	N/A
122.6	26.4	N/A
130.3	26.8	N/A
159.7	30.1	N/A
164.0	32.3	N/A
166.4	35.1	N/A
190.3	39.9	N/A
250.0	25.6	N/A
251.3	22.1	N/A
262.7	23.7	N/A
269.6	25.3	N/A
273.6	23.5	N/A
284.5	25.6	N/A
295.8	24.9	N/A
302.7	25.8	N/A
306.7	24.6	N/A
310.7	25.9	N/A
314.7	35.2	N/A
318.6	71.2	N/A
321.3	88.6	N/A
329.6	79.3	N/A
335.9	77.7	N/A

349.9	75.4	N/A
358.3		N/A
366.6	66.4	N/A
380.8	66.8	N/A
397.5	61.2	N/A
411.8	61.6	N/A
420.0	56.0	N/A
428.3	57.3	N/A
442.7	64.3	N/A
459.2	55.7	N/A
473.7	53.4	N/A
481.8	54.9	N/A
489.9	51.6	N/A
504.5	52.3	N/A
520.8	50.1	N/A
535.6	49.5	N/A
551.8	46.9	N/A
566.6	48.0	N/A
582.7	46.4	N/A
597.6	44.8	N/A
605.5	47.2	N/A
613.4	45.2	N/A
628.5	43.9	N/A
644.3	43.1	N/A
659.5	42.6	N/A
667.3	44.1	N/A
675.0	41.8	N/A
690.3	42.8	N/A
721.5	43.4	N/A
729.2	45.9	N/A
736.9	42.8	N/A
752.4	41.7	N/A
767.8	42.1	N/A
783.4	41.2	N/A
791.0	43.5	N/A
798.5	42.1	N/A
814.3	42.5	N/A
829.4	39.8	N/A
845.3	42.1	N/A
849.9	44.1	N/A
855.4	40.8	N/A

880.8	40.8	N/A
886.4	40.4	N/A
911.7	40.3	N/A
917.4	41.3	N/A
942.7	43.6	N/A
948.5	41.3	N/A
962.3	43.4	N/A
973.4	41.5	N/A
979.3	41.8	N/A
1004.3	41.7	N/A
1010.3	40.9	N/A
1024.1	39.8	N/A
1035.0	41.3	N/A
1041.2	47.3	N/A
1066.0	41.8	N/A
1072.2	41.3	N/A
1085.8	40.4	N/A
1096.7	39.6	N/A
1103.1	39.7	N/A
1127.6	39.3	N/A
1134.1	42.7	N/A
1147.6	40.1	N/A
1158.3	37.8	N/A
1164.9	40.5	N/A
1189.2	38.8	N/A
1196.0	39.4	N/A
1220.2	39.7	N/A
1227.0	41.2	N/A
1251.1	39.9	N/A
1258.0	40.0	N/A
1282.0	38.0	N/A
1289.0	39.4	N/A
1312.9	36.3	N/A
1320.1	38.6	N/A
1343.8	25.1	N/A
1374.9	20.2	N/A
1382.3	27.9	N/A
1405.8	30.6	N/A
1413.3	27.7	N/A
1436.7	27.9	N/A
1444.3	31.7	N/A

Site: 1362B	Dataset: Wellhead 2010-14	Analyte: SF6
Days Post Injection (DPI)	pmol/L	C/C0
364	3503.1	7.28E-02
366	3652.4	7.59E-02
368	3700.9	7.69E-02
369	3668.0	7.62E-02
372	3406.6	7.08E-02
373	3450.8	7.17E-02
384	3385.0	7.03E-02
386	3152.1	6.55E-02
397	3829.5	7.96E-02
398	3906.8	8.12E-02
409	3490.7	7.25E-02
411	3326.3	6.91E-02
422	3639.6	7.56E-02
423	3727.9	7.75E-02
434	4081.1	8.48E-02
436	3649.9	7.58E-02
447	3863.1	8.03E-02
448	3299.3	6.85E-02
459	3388.6	7.04E-02
461	3186.5	6.62E-02
472	3404.3	7.07E-02
473	3005.1	6.24E-02
484	2866.6	5.96E-02
486	2948.5	6.13E-02
497	3481.4	7.23E-02
498	3167.5	6.58E-02
509	2125.5	4.42E-02
511	2240.8	4.66E-02
522	2051.0	4.26E-02
523	2110.6	4.39E-02
534	2599.6	5.40E-02
536	2309.3	4.80E-02
572	2182.7	4.54E-02
573	2021.6	4.20E-02
585	2780.9	5.78E-02
597	1722.3	3.58E-02
598	2190.8	4.55E-02

610	2397.5	4.98E-02
611	2612.1	5.43E-02
622	2374.7	4.93E-02
623	2369.2	4.92E-02
635	3075.9	6.39E-02
636	2608.4	5.42E-02
647	2056.0	4.27E-02
648	2362.2	4.91E-02
660	33931.5	7.05E-01
661	39465.6	8.20E-01
671	10282.9	2.14E-01
672	52520.5	1.09E+00
685	1669.2	3.47E-02
686	2101.0	4.37E-02
697	2846.4	5.91E-02
698	2585.9	5.37E-02
721	2131.5	4.43E-02
734	2132.0	4.43E-02
746	2094.3	4.35E-02
748	2401.7	4.99E-02
759	2174.1	4.52E-02
760	2227.1	4.63E-02
762	2389.6	4.96E-02
772	2260.3	4.70E-02
787	1667.3	3.46E-02
797	1519.6	3.16E-02
798	1545.5	3.21E-02
809	1742.5	3.62E-02
824	1868.9	3.88E-02
834	1498.9	3.11E-02
835	1606.1	3.34E-02
847	1576.0	3.27E-02
859	1558.8	3.24E-02
860	1386.9	2.88E-02
873	1352.9	2.81E-02
884	1883.5	3.91E-02
887	1732.3	3.60E-02
899	2398.4	4.98E-02
912	1807.3	3.76E-02
923	1329.0	2.76E-02
934	1764.4	3.67E-02

948	2356.2	4.90E-02
949	2574.3	5.35E-02
961	1381.0	2.87E-02
972	1518.1	3.15E-02
987	1795.9	3.73E-02
1009	1529.5	3.18E-02
1011	2053.6	4.27E-02
1022	1839.0	3.82E-02
1034	1322.2	2.75E-02
1036	1806.3	3.75E-02
1047	1759.1	3.65E-02
1048	1649.3	3.43E-02
1049	1921.5	3.99E-02
1060	8.0	1.67E-04
1062	14.6	3.04E-04
1082	2535.6	5.27E-02
1083	2567.0	5.33E-02
1085	2578.0	5.36E-02
1105	2351.3	4.89E-02
1106	2252.1	4.68E-02
1108	2130.8	4.43E-02
1128	2241.5	4.66E-02
1129	2153.8	4.47E-02
1131	2517.3	5.23E-02
1151	2111.7	4.39E-02
1153	2050.0	4.26E-02
1154	2009.0	4.17E-02
1174	1939.9	4.03E-02
1176	1974.8	4.10E-02
1177	1924.5	4.00E-02
1197	1812.9	3.77E-02
1199	1817.0	3.78E-02
1200	1730.9	3.60E-02
1220	1730.5	3.60E-02
1222	1625.9	3.38E-02
1223	1720.4	3.57E-02
1243	1663.1	3.46E-02
1245	1664.5	3.46E-02
1246	1680.0	3.49E-02
1266	1602.3	3.33E-02
1268	1596.4	3.32E-02

1269	1580.2	3.28E-02
1289	1577.5	3.28E-02
1291	1567.0	3.26E-02
1293	1566.6	3.26E-02
1313	1385.9	2.88E-02
1314	1393.2	2.89E-02
1316	1399.5	2.91E-02
1336	1296.5	2.69E-02
1337	1354.8	2.81E-02
1339	1255.7	2.61E-02
1359	1286.3	2.67E-02
1360	1278.4	2.66E-02
1362	1281.3	2.66E-02
1382	1228.5	2.55E-02
1383	1225.5	2.55E-02
1385	1210.8	2.52E-02
1405	1130.6	2.35E-02
1406	1168.3	2.43E-02
1408	1132.1	2.35E-02
1426	1379.6	2.87E-02
1427	1218.7	2.53E-02
1428	1133.0	2.35E-02
1429	1087.8	2.26E-02
1429	1070.8	2.22E-02
1431	1077.0	2.24E-02

Site: 1362A	**Dataset: Wellhead 2010-13**	**Analyte: SF6**
Days Post Injection (DPI)	pmol/L	C/C0
464	6415.9	1.33E-01
472	5559.3	1.16E-01
474	6593.8	1.37E-01
475	6255.0	1.30E-01
483	7321.6	1.52E-01
485	5241.4	1.09E-01
486	7867.7	1.63E-01
494	4465.7	9.28E-02
496	3388.8	7.04E-02
497	5146.8	1.07E-01
505	6106.0	1.27E-01
507	5952.6	1.24E-01

508	7567.7	1.57E-01
516	5961.4	1.24E-01
518	5590.6	1.16E-01
519	9609.7	2.00E-01
529	8296.4	1.72E-01
530	7173.0	1.49E-01
538	5944.0	1.24E-01
540	6310.6	1.31E-01
541	10241.4	2.13E-01
549	3970.2	8.25E-02
551	4137.5	8.60E-02
552	3693.0	7.67E-02
560	2731.8	5.68E-02
562	1849.9	3.84E-02
563	8667.5	1.80E-01
571	2447.7	5.09E-02
573	3478.6	7.23E-02
574	4511.5	9.37E-02
582	4460.8	9.27E-02
584	4758.9	9.89E-02
585	4529.2	9.41E-02
593	4383.6	9.11E-02
596	5052.2	1.05E-01
604	4704.9	9.78E-02
606	3329.3	6.92E-02
607	4161.7	8.65E-02
615	5618.8	1.17E-01
617	3149.4	6.54E-02
618	3479.8	7.23E-02
626	3434.7	7.14E-02
628	3381.8	7.03E-02
629	5011.1	1.04E-01
637	5026.4	1.04E-01
639	4615.7	9.59E-02
640	4044.6	8.40E-02
648	5270.1	1.09E-01
650	5321.3	1.11E-01
651	6349.8	1.32E-01
659	3244.1	6.74E-02
661	3524.8	7.32E-02
662	5333.0	1.11E-01

670	3868.9	8.04E-02
672	3267.3	6.79E-02
673	3768.3	7.83E-02
681	3162.5	6.57E-02
683	3697.3	7.68E-02
684	4115.4	8.55E-02
692	3082.3	6.40E-02
694	2784.9	5.79E-02
695	1682.1	3.49E-02
703	3092.9	6.43E-02
705	3061.0	6.36E-02
706	2696.8	5.60E-02
714	4740.4	9.85E-02
716	6622.4	1.38E-01
717	5945.9	1.24E-01
724	6307.9	1.31E-01
727	6138.4	1.28E-01
728	6002.9	1.25E-01
736	5960.1	1.24E-01
738	5861.5	1.22E-01
739	6125.5	1.27E-01
747	5568.6	1.16E-01
749	5559.3	1.16E-01
749	5746.2	1.19E-01
750	5970.6	1.24E-01
750	6530.2	1.36E-01
751	5695.2	1.18E-01
752	6103.8	1.27E-01
761	5879.1	1.22E-01
762	6173.0	1.28E-01
763	6110.1	1.27E-01
772	6141.7	1.28E-01
773	6024.1	1.25E-01
774	5945.5	1.24E-01
783	5774.1	1.20E-01
784	5965.8	1.24E-01
785	5231.2	1.09E-01
794	5637.9	1.17E-01
795	5328.2	1.11E-01
796	5139.8	1.07E-01
805	5032.8	1.05E-01

806	4986.4	1.04E-01
807	4799.7	9.97E-02
816	6807.1	1.41E-01
817	5827.0	1.21E-01
818	5135.7	1.07E-01
827	7139.0	1.48E-01
828	5055.6	1.05E-01
829	4916.9	1.02E-01
838	4895.4	1.02E-01
839	4799.6	9.97E-02
840	4465.6	9.28E-02
849	5514.5	1.15E-01
850	4888.1	1.02E-01
851	4434.1	9.21E-02
860	4405.4	9.15E-02
861	4418.1	9.18E-02
862	4065.6	8.45E-02
871	3976.1	8.26E-02
872	3938.0	8.18E-02
873	4043.8	8.40E-02
882	4085.8	8.49E-02
883	3984.0	8.28E-02
884	4120.9	8.56E-02
893	4192.3	8.71E-02
894	4171.1	8.67E-02
895	4216.8	8.76E-02
904	4243.6	8.82E-02
905	4157.2	8.64E-02
906	4233.4	8.80E-02
915	4069.6	8.46E-02
916	4006.1	8.32E-02
917	3729.9	7.75E-02
926	3782.2	7.86E-02
927	3737.6	7.77E-02
928	3256.3	6.77E-02
937	3384.7	7.03E-02
938	3417.7	7.10E-02
939	3456.5	7.18E-02
948	3585.9	7.45E-02
949	3527.5	7.33E-02
950	3435.9	7.14E-02

959	3536.2	7.35E-02
960	3381.7	7.03E-02
961	3376.3	7.02E-02
970	3386.9	7.04E-02
971	3330.7	6.92E-02
972	3260.7	6.77E-02
981	3252.4	6.76E-02
982	3167.4	6.58E-02
983	2844.3	5.91E-02
992	2907.4	6.04E-02
993	2777.6	5.77E-02
994	2952.2	6.13E-02
1003	2739.6	5.69E-02
1004	2924.4	6.08E-02
1005	3003.1	6.24E-02
1014	2950.8	6.13E-02
1015	2818.7	5.86E-02
1016	2691.5	5.59E-02
1025	2795.0	5.81E-02
1026	2650.5	5.51E-02
1027	2609.6	5.42E-02
1036	2556.4	5.31E-02
1037	2541.9	5.28E-02
1038	2586.6	5.37E-02
1040	2633.9	5.47E-02
1041	2548.9	5.30E-02
1042	2302.6	4.78E-02
1043	2378.1	4.94E-02
1044	2352.2	4.89E-02
1045	2391.4	4.97E-02
1046	2287.8	4.75E-02
1047	2169.7	4.51E-02
1048	2193.9	4.56E-02
1049	2277.2	4.73E-02
1050	2298.5	4.78E-02

Site: 1362A	**Dataset: Vent Meter 2013-14**	**Analyte: SF6**
Days Post Injection (DPI)	pmol/L	C/C0
1094	2740.9	5.69E-02
1096	2895.4	6.02E-02

1098	2770.9	5.76E-02
1129	2545.7	5.29E-02
1131	2570.1	5.34E-02
1133	2750.9	5.72E-02
1164	2474.8	5.14E-02
1166	2406.1	5.00E-02
1168	2479.8	5.15E-02
1200	2235.9	4.65E-02
1201	2330.9	4.84E-02
1203	2366.8	4.92E-02
1235	2079.8	4.32E-02
1237	2149.5	4.47E-02
1238	2180.8	4.53E-02
1270	2155.4	4.48E-02
1272	2383.9	4.95E-02
1273	2120.0	4.40E-02
1305	2027.2	4.21E-02
1307	2061.7	4.28E-02
1309	2059.8	4.28E-02
1340	1987.6	4.13E-02
1342	2070.4	4.30E-02
1344	1955.5	4.06E-02
1375	1973.1	4.10E-02
1377	1992.3	4.14E-02
1379	1970.0	4.09E-02
1411	1902.9	3.95E-02
1412	1946.9	4.05E-02
1414	1844.0	3.83E-02

Site: 1362A	**Dataset: Deep Vent 2013-14**	**Analyte: SF6**
Days Post Injection (DPI)	pmol/L	C/C0
1069	3624.0	7.53E-02
1071	3445.1	7.16E-02
1072	3439.0	7.15E-02
1087	3083.7	6.41E-02
1089	3319.6	6.90E-02
1090	3097.4	6.44E-02
1117	3431.3	7.13E-02
1119	2933.1	6.09E-02
1120	3143.3	6.53E-02

1147	2896.0	6.02E-02
1149	2795.2	5.81E-02
1150	2791.1	5.80E-02
1177	2652.1	5.51E-02
1179	2599.5	5.40E-02
1180	2646.1	5.50E-02
1207	2468.7	5.13E-02
1209	2434.6	5.06E-02
1210	2474.4	5.14E-02
1237	2194.5	4.56E-02
1239	2395.8	4.98E-02
1240	2422.5	5.03E-02
1267	2153.7	4.47E-02
1268	2301.8	4.78E-02
1270	2240.2	4.65E-02
1297	2185.2	4.54E-02
1298	2248.1	4.67E-02
1300	2071.2	4.30E-02
1327	1952.8	4.06E-02
1330	2007.3	4.17E-02
1357	1951.0	4.05E-02
1358	2057.4	4.27E-02
1360	2015.8	4.19E-02
1387	1904.8	3.96E-02
1388	1986.6	4.13E-02
1390	1840.2	3.82E-02
1417	1983.9	4.12E-02
1420	1962.3	4.08E-02

Site: 1362A	**Dataset: Downhole 2010-14**	**Analyte: Cs**
Days Post Injection (DPI)	nmol/L	C/C0
2	6.1	N/A
4	8.4	N/A
6	8.4	N/A
8	8.3	N/A
10	8.6	N/A
12	8.2	N/A
14	8.4	N/A
16	8.3	N/A
18	9.1	N/A

20	8.7	N/A
22	8.8	N/A
24	9.1	N/A
28	8.9	N/A
30	8.8	N/A
32	8.8	N/A
34	8.8	N/A
36	8.5	N/A
38	8.9	N/A
40	8.3	N/A
44	7.8	N/A
48	8.2	N/A
52	8.1	N/A
54	8.0	N/A
58	8.0	N/A
59	7.8	N/A
61	7.9	N/A
63	7.9	N/A
65	8.0	N/A
67	7.8	N/A
69	7.9	N/A
71	7.7	N/A
73	7.7	N/A
75	7.9	N/A
77	7.7	N/A
79	7.9	N/A
81	7.8	N/A
83	8.5	N/A
85	8.1	N/A
87	8.1	N/A
89	8.5	N/A
91	8.4	N/A
93	8.4	N/A
95	8.6	N/A
97	8.8	N/A
99	8.8	N/A
101	8.6	N/A
103	8.9	N/A
105	8.4	N/A
107	8.5	N/A
109	8.6	N/A

111	8.7	N/A
135	8.3	N/A
139	8.3	N/A
159	8.8	N/A
163	8.8	N/A
183	8.6	N/A
187	8.7	N/A
206	8.9	N/A
210	8.6	N/A
230	8.8	N/A
234	8.6	N/A
254	8.7	N/A
258	8.5	N/A
278	9.0	N/A
282	8.8	N/A
302	9.0	N/A
306	8.6	N/A
325	8.7	N/A
329	8.7	N/A
349	8.8	N/A
353	8.5	N/A
373	8.6	N/A
377	8.6	N/A
397	8.5	N/A
401	8.6	N/A
421	8.5	N/A
425	8.7	N/A
445	8.5	N/A
449	8.7	N/A
468	8.5	N/A
472	8.8	N/A
492	8.7	N/A
496	8.5	N/A
510	8.4	N/A
514	8.6	N/A
534	8.5	N/A
538	8.6	N/A
558	8.5	N/A
562	8.4	N/A
582	8.5	N/A
586	8.6	N/A

605	8.5	N/A
609	8.4	N/A
629	8.2	N/A
633	8.3	N/A
653	8.3	N/A
657	8.2	N/A
677	8.3	N/A
681	8.3	N/A
701	8.2	N/A
705	8.4	N/A
724	8.2	N/A
728	8.4	N/A
748	8.2	N/A
752	8.3	N/A
772	8.3	N/A
776	8.2	N/A
796	8.3	N/A
800	8.1	N/A
820	8.4	N/A
824	8.3	N/A
844	8.3	N/A
848	8.4	N/A
867	8.4	N/A
871	8.3	N/A
891	8.4	N/A
895	8.2	N/A
915	8.3	N/A
919	8.5	N/A
939	8.2	N/A
943	8.5	N/A
963	8.4	N/A
967	8.2	N/A
981	8.5	N/A
985	8.4	N/A
1004	8.3	N/A
1008	8.4	N/A
1028	8.5	N/A
1032	8.4	N/A
1052	8.5	N/A
1056	8.4	N/A
1076	8.3	N/A

1080	8.5	N/A
1100	8.4	N/A
1104	8.4	N/A
1123	8.4	N/A
1127	8.4	N/A
1147	8.3	N/A
1151	8.4	N/A
1171	8.4	N/A
1175	8.5	N/A
1195	8.2	N/A
1199	8.3	N/A
1219	8.3	N/A
1223	8.3	N/A
1243	8.4	N/A
1247	8.4	N/A
1266	8.3	N/A
1270	8.4	N/A
1290	8.3	N/A
1294	8.4	N/A
1314	8.3	N/A
1318	8.4	N/A
1338	8.2	N/A
1342	8.3	N/A
1362	8.4	N/A
1366	8.3	N/A
1385	8.4	N/A
1389	8.1	N/A
1409	8.0	N/A
1413	8.0	N/A
1433	8.0	N/A
1437	8.2	N/A

Site: 1026B	**Dataset: Downhole 2010-14**	**Analyte: Cs**
Days Post Injection (DPI)	nmol/L	C/C0
460	0.0	0.00E+00
487	17.4	3.61E-04
488	0.0	0.00E+00
490	17.8	3.70E-04
490	17.8	3.70E-04
516	19.8	4.12E-04

518	12.4	2.58E-04
519	0.0	2.81E-07
546	0.0	2.84E-07
547	5.3	1.10E-04
549	0.0	3.26E-07
575	0.0	2.81E-07
575	0.0	2.81E-07
577	0.0	0.00E+00
578	0.0	2.49E-07
605	0.0	2.75E-07
606	0.0	0.00E+00
608	0.0	2.59E-07
634	0.0	2.78E-07
636	0.0	0.00E+00
637	0.0	2.84E-07
652	0.0	0.00E+00
664	0.0	2.81E-07
665	0.0	0.00E+00
667	0.0	2.78E-07
693	0.0	2.90E-07
695	0.0	0.00E+00
696	0.0	2.84E-07
723	0.0	2.90E-07
724	0.0	0.00E+00
726	0.0	2.90E-07
741	0.0	0.00E+00
752	0.0	2.94E-07
754	0.0	0.00E+00
755	0.0	2.97E-07
770	0.0	0.00E+00
782	0.0	2.84E-07
783	0.0	2.90E-07
785	0.0	2.97E-07
799	0.0	0.00E+00
811	0.0	2.94E-07
813	0.0	2.97E-07
814	0.0	2.72E-07
829	0.0	0.00E+00
841	2.6	5.50E-05
842	0.0	2.87E-07
844	4.5	9.36E-05

1003	0.4	7.47E-06
1004	0.8	1.74E-05
1006	0.1	2.17E-06
1032	0.4	7.72E-06
1034	0.8	1.72E-05
1035	0.9	1.78E-05
1062	0.4	7.98E-06
1063	0.9	1.86E-05
1065	0.1	2.22E-06
1085	0.4	7.39E-06
1088	0.4	7.31E-06
1091	17.6	3.66E-04
1093	14.0	2.92E-04
1094	23.3	4.83E-04
1096	0.4	7.81E-06
1097	0.4	7.39E-06
1106	0.9	1.91E-05
1108	0.9	1.88E-05
1109	0.4	7.64E-06
1115	0.3	7.24E-06
1118	0.4	7.55E-06
1121	17.4	3.62E-04
1122	14.0	2.91E-04
1124	0.4	7.72E-06
1127	4.8	9.88E-05
1130	0.4	7.47E-06
1150	0.4	7.72E-06
1152	0.8	1.69E-05
1153	0.1	2.20E-06
1180	0.4	7.81E-06
1181	0.8	1.76E-05
1183	0.1	2.22E-06
1209	0.4	8.08E-06
1211	0.9	1.86E-05
1212	0.1	2.32E-06
1239	0.4	7.39E-06
1240	0.8	1.76E-05
1242	0.1	2.22E-06
1268	0.3	7.24E-06
1293	16.7	3.47E-04
1295	19.2	4.00E-04

1296	16.4	3.40E-04
1298	0.0	0.00E+00
1299	0.0	0.00E+00
1301	0.0	0.00E+00
1327	0.0	0.00E+00
1329	0.0	0.00E+00
1330	0.0	0.00E+00
1357	0.0	0.00E+00
1358	0.0	0.00E+00
1360	0.0	0.00E+00
1386	0.0	0.00E+00
1388	0.0	0.00E+00
1389	0.0	0.00E+00
1416	0.0	0.00E+00
1417	0.0	0.00E+00
1419	0.0	0.00E+00
1445	0.0	0.00E+00
1447	0.0	0.00E+00
1448	0.0	0.00E+00

Site: 1026B	**Dataset: Wellhead 2010-14**	**Analyte: Cs**
Days Post Injection (DPI)	nmol/L	C/C0
0	0.0	8.62E-05
2	0.0	3.14E-05
3	0.0	6.41E-05
15	0.0	1.18E-04
17	0.0	6.15E-05
18	0.0	7.12E-05
30	0.0	4.54E-05
33	9.6	1.99E-04
45	9.3	1.92E-04
46	7.1	1.47E-04
47	6.3	1.31E-04
61	6.3	1.30E-04
62	0.0	8.91E-05
74	0.0	8.92E-05
76	0.0	4.74E-05
89	0.0	1.21E-04
90	0.0	1.25E-04
92	0.0	1.12E-04

104	0.0	1.03E-04
105	0.0	1.09E-04
106	0.0	1.15E-04
118	0.0	9.40E-05
120	0.0	1.03E-04
121	0.0	7.94E-05
133	0.0	7.06E-05
134	10.2	2.11E-04
136	0.0	1.14E-04
148	0.0	8.83E-05
149	0.0	8.65E-05
151	0.0	6.37E-05
162	0.0	6.50E-05
164	22.0	4.57E-04
165	17.2	3.58E-04
177	6.9	1.43E-04
179	0.0	1.19E-04
180	0.0	9.78E-05
192	63.0	1.31E-03
193	64.4	1.34E-03
195	62.8	1.30E-03
207	65.2	1.35E-03
208	0.0	5.38E-05
210	17.4	3.62E-04
221	15.0	3.13E-04
223	9.9	2.06E-04
224	6.3	1.30E-04
236	32.6	6.77E-04
238	25.0	5.19E-04
239	20.1	4.17E-04
251	18.8	3.91E-04
252	0.0	8.02E-05
254	38.2	7.94E-04
266	31.2	6.48E-04
267	48.4	1.01E-03
287	22.6	4.69E-04
293	78.2	1.62E-03
294	65.3	1.36E-03
297	44.2	9.18E-04
298	123.4	2.56E-03
301	56.6	1.18E-03

310	95.8	1.99E-03
311	34.4	7.15E-04
312	201.1	4.18E-03
802	0.0	1.12E-06
803	0.0	8.00E-07
803	0.0	1.20E-06
804	0.0	1.24E-06
826	0.0	1.27E-06
827	0.0	3.09E-05
827	0.0	1.27E-06
828	0.0	1.21E-06
850	0.0	1.12E-06
851	0.0	6.59E-07
851	0.0	1.20E-06
852	0.0	1.21E-06
873	0.0	1.12E-06
875	0.0	6.38E-07
875	0.0	1.15E-06
876	0.0	1.16E-06
897	0.0	1.07E-06
898	0.0	6.31E-07
898	13.3	2.77E-04
900	0.0	1.17E-06
910	0.0	1.28E-06
911	0.0	1.30E-06
921	0.0	1.12E-06
922	0.0	6.52E-07
922	13.3	2.77E-04
923	0.0	1.21E-06
945	0.0	6.81E-05
946	0.0	7.11E-05
946	0.0	1.27E-06
947	0.0	6.85E-05
969	0.0	1.21E-06
969	0.0	1.12E-06
970	0.0	6.38E-07
970	0.0	1.17E-06
971	0.0	1.36E-06
992	0.0	1.12E-06
994	0.0	6.59E-07
994	0.0	1.19E-06

995	0.0	1.23E-06
1016	0.0	1.13E-06
1017	0.0	6.31E-07
1019	0.0	1.12E-06
1040	0.0	1.12E-06
1041	0.0	6.18E-07
1042	0.0	1.12E-06
1064	0.0	1.12E-06
1065	0.0	6.18E-07
1066	0.0	1.12E-06
1088	0.0	1.12E-06
1089	0.0	1.98E-06
1090	0.0	1.12E-06
1108	0.0	0.00E+00
1111	0.0	0.00E+00
1131	0.0	0.00E+00
1133	0.0	0.00E+00
1153	0.0	0.00E+00
1155	0.0	0.00E+00
1175	0.0	0.00E+00
1177	0.0	0.00E+00
1197	0.0	0.00E+00
1199	0.0	0.00E+00
1221	0.0	0.00E+00
1222	0.0	0.00E+00
1242	0.0	0.00E+00
1243	0.0	0.00E+00
1244	0.0	0.00E+00
1264	0.0	0.00E+00
1265	0.0	0.00E+00
1266	0.0	0.00E+00
1286	0.0	0.00E+00
1287	0.0	0.00E+00
1288	0.0	0.00E+00
1297	210.3	4.37E-03
1298	218.5	4.54E-03
1299	219.4	4.56E-03
1308	275.7	5.73E-03
1309	281.6	5.85E-03
1311	289.3	6.01E-03
1319	352.5	7.32E-03

1321	358.2	7.44E-03
1322	391.5	8.14E-03
1331	397.7	8.26E-03
1332	385.7	8.01E-03
1333	373.2	7.75E-03
1342	427.0	8.87E-03
1343	465.0	9.66E-03
1344	469.6	9.76E-03
1353	305.0	6.34E-03
1354	233.9	4.86E-03
1355	236.2	4.91E-03
1364	85.8	1.78E-03
1365	95.8	1.99E-03
1366	103.2	2.14E-03
1375	0.0	1.22E-06
1376	0.0	1.36E-06
1377	0.0	1.63E-06
1386	0.0	1.12E-06
1387	0.0	1.51E-06
1388	0.0	1.25E-06
1397	59.0	1.23E-03
1398	0.0	1.17E-06
1399	0.0	1.20E-06
1408	0.0	1.19E-06
1409	0.0	1.30E-06
1411	0.0	1.42E-06
1419	0.0	1.34E-06
1422	0.0	1.31E-06
1431	0.0	1.28E-06
1432	0.0	1.23E-06
1433	38.8	8.06E-04

Site: 1301A	**Dataset: Wellhead 2010-14**	**Analyte: Cs**
Days Post Injection (DPI)	nmol/L	C/C0
4	0.0	0.00E+00
6	0.0	0.00E+00
7	0.0	0.00E+00
21	0.0	0.00E+00
23	0.0	0.00E+00
35	0.0	0.00E+00

37	0.0	0.00E+00
39	0.0	0.00E+00
51	0.0	0.00E+00
53	0.0	0.00E+00
54	0.0	0.00E+00
67	0.0	0.00E+00
68	0.0	0.00E+00
70	0.0	0.00E+00
82	0.0	0.00E+00
84	0.0	0.00E+00
85	0.0	0.00E+00
98	7.8	1.62E-04
99	0.0	0.00E+00
101	0.0	0.00E+00
113	0.0	0.00E+00
115	0.0	0.00E+00
116	0.0	0.00E+00
129	0.0	0.00E+00
130	0.0	0.00E+00
132	0.0	0.00E+00
144	0.0	0.00E+00
146	0.0	0.00E+00
147	0.0	0.00E+00
160	0.0	0.00E+00
161	0.0	0.00E+00
163	57.8	1.20E-03
175	0.0	0.00E+00
177	0.0	0.00E+00
178	0.0	0.00E+00
191	0.0	0.00E+00
192	0.0	0.00E+00
194	0.0	0.00E+00
206	0.0	0.00E+00
208	0.0	0.00E+00
210	0.0	0.00E+00
222	0.0	0.00E+00
224	0.0	0.00E+00
225	0.0	0.00E+00
238	0.0	0.00E+00
239	0.0	0.00E+00
241	0.0	0.00E+00

253	0.0	0.00E+00
255	0.0	0.00E+00
256	0.0	0.00E+00
259	604.2	1.26E-02
261	4082.6	8.48E-02
262	3700.8	7.69E-02
264	3841.2	7.98E-02
266	3811.8	7.92E-02
266	3846.3	7.99E-02
267	0.0	0.00E+00
269	0.0	0.00E+00
270	204.0	4.24E-03
272	428.0	8.89E-03
273	0.0	0.00E+00
275	0.0	0.00E+00
276	295.6	6.14E-03
278	671.3	1.39E-02
280	1032.2	2.14E-02
281	0.0	0.00E+00
283	15848.1	3.29E-01
283	16027.4	3.33E-01
284	9226.0	1.92E-01
286	16502.8	3.43E-01
287	2806.6	5.83E-02
289	4963.6	1.03E-01
289	4994.4	1.04E-01
290	8277.4	1.72E-01
292	5288.1	1.10E-01
294	9689.3	2.01E-01
298	15299.8	3.18E-01
300	40034.7	8.32E-01
301	19721.9	4.10E-01
303	15605.3	3.24E-01
304	7983.4	1.66E-01

Site: 1362A	**Dataset: Wellhead 2014-19**	**Analyte: Cs**
Days Post Injection (DPI)	nmol/L	C/C0
1466	1581.8	3.29E-02
1554	1852.9	3.85E-02
1642	1603.6	3.33E-02

1730	1547.6	3.22E-02
1818	1356.4	2.82E-02
1889	1014.7	2.11E-02
1977	968.5	2.01E-02
2065	1046.5	2.17E-02
2153	843.2	1.75E-02
2241	873.7	1.82E-02
2329	853.8	1.77E-02
2417	838.8	1.74E-02
2505	908.5	1.89E-02
2593	748.5	1.56E-02
2681	783.3	1.63E-02
2769	703.2	1.46E-02
2857	623.8	1.30E-02
2945	597.9	1.24E-02
3121	589.6	1.22E-02

Site: 1362B	**Dataset: Wellhead 2014-19**	**Analyte: Cs**
Days Post Injection (DPI)	nmol/L	C/C0
1459	953.1	1.98E-02
1488	908.1	1.89E-02
1548	874.1	1.82E-02
1607	891.3	1.85E-02
1666	838.3	1.74E-02
1725	696.3	1.45E-02
1784	846.7	1.76E-02
1843	702.0	1.46E-02
1903	615.5	1.28E-02
1962	696.1	1.45E-02
2021	634.1	1.32E-02
2080	633.5	1.32E-02
2139	665.5	1.38E-02
2199	573.7	1.19E-02
2258	616.3	1.28E-02
2317	559.2	1.16E-02
2367	524.1	1.09E-02
2391	532.8	1.11E-02
2450	408.4	8.49E-03
2509	451.9	9.39E-03
2568	446.1	9.27E-03

2628	382.9	7.96E-03
2687	381.3	7.92E-03
2746	321.7	6.68E-03
2805	382.1	7.94E-03
2864	403.9	8.39E-03
2924	383.2	7.96E-03
2983	295.3	6.13E-03
3042	305.2	6.34E-03
3101	327.3	6.80E-03
3160	329.7	6.85E-03
3219	310.2	6.44E-03